Atomic Force Microscopy of Biofilm Adhesion

Jamie Thomas Blakeman

A thesis presented for the degree of

Doctor of Philosophy

Department of Physics & Astronomy

The University of Sheffield

September 2019

Contents

List of Figures

List of Tables

Abstract

The adhesive behaviour of extracellular polymeric substances to poly(ethylene terephthalate), a model hydrophobic surface, were measured in response to their degradation by enzymes known for their biofilm dispersion potential. By examining the physical changes in the nature of the binding, structural or adhesive roles could be established for the targets of the enzymes. Degradation of extracellular DNA (eDNA) significantly decreased the adhesive force of *Micrococcus luteus* biofilms with the surface, and furthermore almost completely eliminated any components of the biofilm maintaining the adhesion. This established a key structural role for eDNA.

Due to the significant results observed by the targeting of eDNA, a highly potent novel DNase was investigated to understand its mechanism of action. This would allow further optimisation of the enzyme to maximise its efficiency against a major structural component of bacterial biofilms. Rapid data collection and computer software was used to construct and validate a model of the enzyme activity. This resulted in real world conditions that must be met to maximise the activity of the enzyme, as well as providing direction for additional engineering of the enzyme's behaviour.

The tools and procedures developed during the study of the model bacterium, *Micrococcus luteus*, were used to study the adhesive properties of two pathogens, *Leishmania mexicana* and *Staphylococcus aureus* (*S. aureus*). Improving understanding of the adhesive mechanisms used by these pathogens allows for the development of new treatments against them. Custom MATLAB scripts enabled new data analysis of the interaction between *Leishmania* parasites and galactose-coated AFM tips. This helped elucidate the binding changes used by the parasite as it matures and becomes infectious. Biofilm cantilevers were modified to examine a potential skin treatment that has the potential to decrease the adhesion of *S. aureus* to epithelial cells. A decrease in peak adhesion of 52 % was observed by force experiments between a biofilm-coated cantilever and treated human epithelial cells.

Abbreviations

2-CP	2-chlorophenol
AB	acid-base
AC	alternating current
AES	alcohol ethoxysulfates
AFM	atomic force microscopy
AO	amine oxide
APTES	(3-aminopropyl)triethoxysilane
ATCC	American Type Culture Collection
B. subtilis	*Bacillus subtilis*
BM	Brownian motion
BSA	bovine serum albumin
BSAA	biotinylated bovine serum albumin
CLSM	confocal laser scanning microscopy
CV	crystal violet
DAPI	4',6-diamidino-2-phenylindole
DI	deionised water
DLVO theory	Derjaguin, Landau, Verwey, Overbeek theory
DMSO	dimethylsulfoxide
DNA	deoxyribonucleic acid

DoX	design of experiment
E	Young's Modulus
E. coli	*Escherichia coli*
EC	extracellular loop
EDC	1-ethyl-3-(3-dimethylaminopropyl) carbodiimide
EDL	electrostatic double layer
eDNA	extracellular deoxyribonucleic acid
EDTA	ethylenediaminetetraacetic acid
ELISA	enzyme-linked immunosorbent assay
EMA	effective medium approximation
EPS	extracellular polymeric substances
GPI	glycophosphatidylinositol
HeLa	epithelial cell line named for Henrietta Lacks
HFIP	hexafluroisopropanol
HI	hydrophilicity index
κ^{-1}	Debye length
L. mexicana	*Leishmania mexicana*
LAS	linear alkylbenzene sulfonates
LPG	lipophosphoglycan
LvdW	Lifshitz van der Waals
M. luteus	*Micrococcus luteus*
MRSA	Methicillin-resistant *Staphylococcus aureus*
NA	nutrient agar
NB	nutrient broth

NHS	*N*-methylmorpholine *N*-oxide
OPD	*o*-phenylenediamine dihydrochloride
Ψ	surface potential
PBS	phosphate-buffered saline
PDE	phosphodiesterase
PEG	poly(ethylene glycol)
PEI	poly(ethylene imine)
PLL	poly-L-lysine
PMMA	poly(methyl methacrylate)
PVAm	poly(vinyl amine)
PZT	polycrystalline lead zirconate titanate
QCM-D	quartz crystal microbalance with dissipation monitoring
S. aureus	*Staphylococcus aureus*
SAB	*Staphylococcus aureus* bacteremia
SCFS	single cell force spectroscopy
SFM	scanning force microscopy
SRI	stain removal index
STORM	stochastic optical reconstriction microscopy
TEM	tetraspanin-enriched microdomain
TRIS	tris(hydroxymethyl)aminomethane
TSA	tryptic soy agar
TSB	tryptic soy broth
UV	ultra-violet
xDLVO theory	extended Derjaguin, Landau, Verwey, Overbeek theory

Presentations and publications

The contents of this thesis were presented at the following conferences:

- **J. T. Blakeman**, A. L. Morales-García, J. Mukherjee, K. Gori, A. S. Hayward, N. J. Lant, M. Geoghegan, "Extracellular DNA Provides Structural Integrity to a *Micrococcus luteus* Biofilm". Oral presentation, American Chemical Society National Fall 2019 Meeting, San Diego, United States of America.

- **J. T. Blakeman**, A. L. Morales-García, M. Geoghegan, "Atomic Force Microscopy for Biofilm Adhesion". Oral presentation, Centre for Doctoral Training Industrial Showcase 2018 (Best presentation award), Sheffield, United Kingdom.

The contents of this thesis will be included in the following publications:

- **J. T. Blakeman**, A. L. Morales-García, J. Mukherjee, K. Gori, A. S. Hayward, N. J. Lant, M. Geoghegan, "Extracellular DNA Provides Structural Integrity to a *Micrococcus luteus* Biofilm", *Langmuir*, 2019, **35**, 6468–6475.

- A. R. Hall, **J. T. Blakeman**, A. M. Eissa, P. Chapman, A. L. Morales-García, L. Stennett, O. Martin, E. Giraud, D. H. Dockrell, N. R. Cameron, M. Wiese, L. Yakob, M. E. Rogers, M. Geoghegan, "Molecular mapping of sand fly gut adhesins on the surface of the human protozoan pathogen *Leishmania mexicana* by scanning force spectroscopy reveals an opportunity for transmission blockade". (Manuscript in preparation, author's contribution: analysis of secondary peak data and new antibody AFM experiments)

- R. Issa, L. Partridge, C. Walther, M. Geoghegan, **J. T. Blakeman**, J. Wood, P. Monk, "Modification of tetraspanin-enriched microdomains as a strategy to prevent bacterial infection of human epithelial cells". (Manuscript in preparation, author's contribution: all AFM experiments).

Acknowledgements

Firstly, I would like to thank my supervisor, Prof. Mark Geoghegan, for the opportunity to research this fulfilling project. I didn't envisage the move from Chemistry to Physics, to study a microbiology project, being so rewarding. A special thanks goes to Dr Ana Morales-García, who despite only being tasked as a research colleague for my first year, became a mentor, friend and inspiring figure for the entirety of this project. I was fortunate enough to take part in many interesting collaborative projects during my research, may of which that were instigated by the constant championing from Ana.

I would also like to thank the many people at Procter & Gamble for their part in the project and making me feel so welcome during my time in Newcastle. My thanks to Dr Adam Hayward and Dr Neil Lant for their role in creating and advancing this project. I am grateful to Adam Malekpour for guiding me through my three months in industry and making it both fun and intensely rewarding learning experience. My thanks too go to Nazar Momin and Joana Pinheiro Da Silva Pinto for their knowledge and time during my interactions with the analytical side of industry.

There are so many people at the University of Sheffield to thank. Most importantly the supportive members of G floor for their friendship. Thank you, Dr Ellie Dougherty, Emily Hall, Emilia Hudzik, Dr Stephanie Burg, Jozra Garrido Velasco and Dr Tom Kennelly. Thank you also to the many friends across the CDT cohorts.

I am very grateful to all those involved in keeping the various labs running across the university, but especially the two Nics. Nic White in Animal and Plant Sciences for her guidance and stewardship of the microbiology labs and Dr Nic Mullin in Physics Astronomy for his expertise in maintaining the AFM facilities. Thanks also go to Dr Andy Parnell for his help in all things related to the Physics department.

In the Department of Chemical and Biological Engineering, I'd like to thank Dr Joy Mukherjee for his time, patience and knowledge in confocal microscopy. In the

Light Microscopy Facility in Biomedical Science, thanks to Dr Darren Robinson, for his rapid assistance in the confocal analysis software.

In the Department of Infection, Immunity & Cardiovascular Disease, my thanks go to Prof. Pete Monk and Dr Rahaf Issa for the opportunity to contribute to their research and to Katie Cooke for her assistance with the labs there.

For the opportunity to further expand my data analysis, thanks to go to Dr Amy Hall, for the trust and immense patience shown to contribute to her work on Leishmania. Thanks also go to Dr Matthew Rogers at the London School of Hygiene and Tropical Medicine for his assistance with further experiments.

Away from research, a sincere thank you to the team at Inspiration for Life for welcoming me into their family. Catherine Annabel, Dr Mike Weir and especially the radio duo of Andy Tattersall and Mark Clowes, your dedication to the cause is incredible.

A special thank you to Dr Andy Taylor, my chemistry teacher at King Edward's VI Camp Hill, for making science so interesting and compelling as a student. When you recommended the University of Sheffield, in part for the number of doctorates they produce from our school, I didn't anticipate I would venture this far down the same path. Due to your impact, I hope to teach at some point in my career.

Thank you to the many close friends who I have gained during my time at Forge, in the students' union. Student media provided opportunities to teach, grow and learn, which have profoundly shaped my university experience. Without it, I also would not have met my kind and loving partner, Kerry. Thank you so much for your support throughout the entire process, especially for making the daunting task of moving to another city, so full of fun, food and adventures at the coast. Extended thanks go to your family, Andrea, Bruce, Paddy and Maureen for making me part of the pack.

Last, but not least, I am eternally grateful to my parents Mary and John, for their love and support throughout my life. Thank you for creating such an encouraging and rewarding upbringing. I have no doubt that the copious amounts of Lego bricks helped build the problem solving skills and technical outlook that have served me so well through this research. Thanks of course go to the entirety of my family and especially my talented sister, Francesca.

Chapter 1

Introduction

This project began with the aim of increasing the understanding of how bacteria adhere to textile substrates and how industrially available enzymes might disrupt these communities. *Micrococcus luteus* was chosen as the model bacterium and poly(ethylene terephthalate) as the model substrate. By investigating the changes in adhesion of bacteria before and after exposure to different enzymes, the roles of the substances targeted by the enzymatic treatment could be determined.

This introductory chapter begins by explaining how and why bacteria establish biofilm communities and the methods available to study them, with a focus on atomic force microscopy (AFM). A brief review of how AFM cantilevers have been functionalised with biological material follows, as well as the interest of industry and medicine in studying and disrupting bacterial and pathogenic adhesion.

1.1 *Micrococcus luteus*

Micrococcus luteus (*M. luteus*) is a Gram positive, nonmotile bacteria, commonly used as a model organism[1] by virtue of its sensitivity to enzymes,[2] ability to utilize a number of carbon sources,[3] ability to resuscitate from dormancy,[4] potential role in bioremediation,[5] and its known preferential attachment to hydrophobic surfaces such as poly(ethylene terephthalate) (PET).[6]

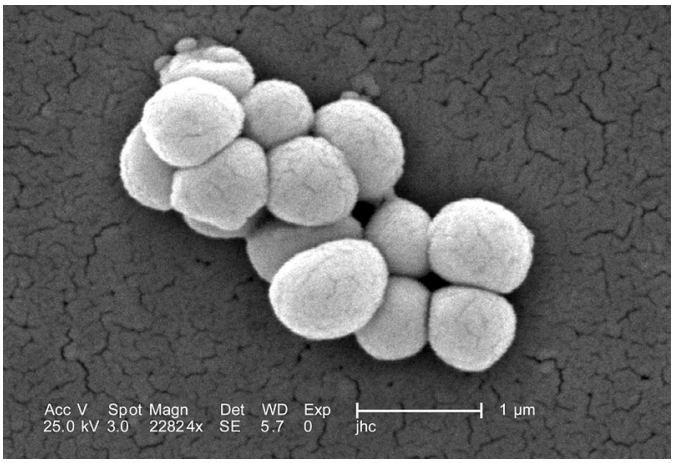

Figure 1.1: *Micrococcus luteus* imaged using a scanning electron micrograph (SEM). Image courtesy of Janice Carr, United States Centers for Disease Control and Prevention.

It was first identified as *Micrococcus lysodeikticus* by Alexander Fleming in 1922,[2] before his discovery of penicillin. The American Type Culture Collection (ATCC) reclassified the bacteria as *M. luteus* in 1968.[7] *M. luteus* is commonly found across mammalian skin, as well as in soil, dust and water.[6,8,9] Although mainly considered to be safe bacteria to work with, there are reports of *M. luteus* displaying pathogenic behaviour in immunocompromised humans and farmed fish stocks.[8,9]

The bacterium is held largely responsible for malodour on the body and clothing, due to its ability to fully catabolise saturated, monounsaturated and methyl-branched fatty acids.[6,10,11]

Table 1.1: Taxonomy of *Micrococcus*

Taxonomy of *Micrococcus*	
Kingdom	Bacteria
Phylum	Actinobacteria
Order	Actinomycetales
Family	Micrococcaceae
Genus	*Micrococcus*
Species	*M. luteus*

1.2 Biofilm formation

For a large part of the history of microbiology, microbes were believed to live freely from each other in a planktonic form. It is now accepted that the majority of bacteria live in complex communities called biofilms, adhering either to interfaces or themselves.[12] Attaching to a surface stimulates bacterial growth as organic material suspended in liquid settles and is deposited on the surface, increasing the local concentration of nutrients available.[13] Once the bacteria have begun to colonise a surface, they will begin to build a matrix around the population that serves a variety of functions including antibiotic resistance[14], structural rigidity and protection from the external environment such as mechanical damage and shear caused by fluid flow.[15] As well as a physical barrier, the matrix also holds dormant persister cells and highly resistant small colony variants which feature up regulation of several antibiotic resistance genes.[13] To develop new strategies to combat biofilms, an in-depth knowledge of what contributes to the matrix is required.[15] The extracellular polymeric substances (EPS) consist of a complex mixture of polysaccharides, proteins, DNA and other less significant compounds. This has seen a rise in research of dispersal methods that use enzymes that can disrupt these components of the biofilm. This can then be followed up with an alternative methods, such as an antibiotic treatment or mechanical action, to eradicate a biofilm.[16]

1.2.1 The biofilm cycle

The formation of a biofilm at an interface begins with the deposition of a conditioning film. This film is comprised of organic material (eg proteins, polysaccharides, nutrients) that diffuse towards the substrate, from the solution it has been placed in. This film alters the physiochemical properties of the surface and can aid the adhesion of the colonising bacteria.[17–19]

Bacteria then begin approaching the surface either via Brownian motion or active movement towards the higher nutrient concentration found at a surface. The initial

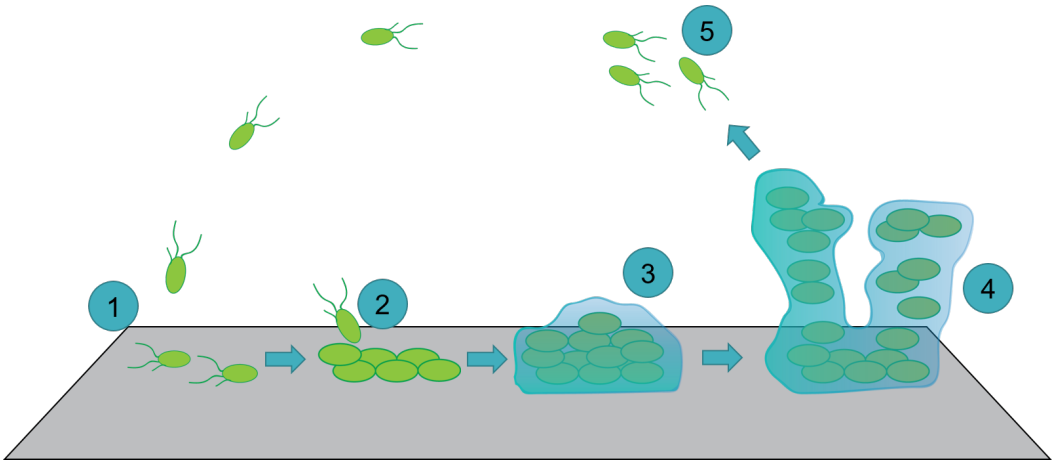

Figure 1.2: Diagrammatic representation of a typical biofilm cycle, which comprises distinct stages. 1) Initial reversible attachment of planktonic bacteria to a surface. 2) Permanent adhesion followed by growth and division. Production of flagella, deactivation of pili. 3) Production of extracellular polymeric substances (EPS). 4) Biofilm maturation and three-dimensional structure developing. 5) Dispersal of planktonic bacteria to colonise new environments. Figure based on those by Hall-Stoodley[14] and Sadekuzzaman[17].

reversible adhesion towards the surface takes place through weak interactions, such as van der Waals forces.[20,21] Cells may detach from the substrate at this point and return to a planktonic regime.[22] Irreversible attachment follows as the microbe gets closer to the surface. This stronger adhesion takes place via hydrophobic/hydrophilic interactions and attachment structures such as flagella, lipo-polysaccharides and pili help to overcome electrostatic repulsions.[20,21,23] The initial attachment is explored in more detail in Section 1.3. From this point enzymes, detergents or heat are required to remove the biofilm from the surface.[24]

Once the bacteria have become physically adsorbed onto the surface the production of the EPS, composed of proteins, polysaccharides and extracellular deoxyribonucleic acid (eDNA) can begin.[25,26] With the protective EPS in place the biofilm can mature to a structure that contains water channels to distribute nutrients and signalling molecules.[14,18] Cells can detach from the biofilm and disperse to new areas to propagate the population. This can be due to external factors such as an increase in fluid shear, or be due to internal enzymatic degradation.[24]

1.2.2 Extracellular Polymeric Substances

The abbreviation EPS is commonly used to refer to extracellular polymeric substances, but originally it stood for extracellular polysaccharides. The role that other polymers play in the EPS, such as proteins, lipids and DNA are now well respected.[27] The production of EPS has been observed in both prokaryotic (bacteria, archaea) and eukaryotic (algae, fungi) microorganisms. Polysaccharides, proteins, lipids and nucleic acids have all been catalogued as components of bacterial EPS. The matrix they form facilitates the retention of enzymes, cellular debris and genetic material, leading to the the extracellular matrix being described as, 'a microbial recycling yard'.[28]

The components that make up an extracellular matrix vary from microbe to microbe, with the circumstances that the biofilm forms in also affecting the composition. Biofilm matrices, even those produced by an identical organism, will vary greatly in their composition and physical properties due to the local conditions in which they grow.[29,30] Despite only contributing a small amount to the total mass of a biofilm (which can be up to 97% water[31]) the EPS compromise 50-90% of the organic mass of a biofilm.[28] Different enzymes are involved in the self-degradation of the EPS, with hydrolases, lyases, glycosidases, esterases and others all being abundant in biofilms as extracellular proteins.[29,32,33] These enzymes serve to release cells from the community and possibly provide low-molecular weight products as carbon and energy sources for metabolism by the resident bacteria. The breakdown also releases cells that allows for colonisation of new sites.[29,34]

It has been demonstrated that the biofilm matrix allows an organism to adhere to hydrophobic and hydrophilic surfaces by means of different EPS components.[28,35] In adhering to surfaces, three major kinds of forces can be distinguished: electrostatic, hydrogen bonding and London dispersion forces.[36,37]

1.3 Physical aspects of bacterial adhesion

As microorganisms are a few microns across in size and interactions between hydrophobic and hydrophilic molecules or surfaces occur in biological systems, the theories that are used in physics to describe colloids have been used to understand the movement and adhesion of bacteria to surfaces.[38]

Deposition of colloidal bacteria is governed by Brownian motion (BM) and hydrodynamic forces, while the adhesion to a surface depends on Liftshitz-van der Waals (LvdW), electrostatic double layer (EDL), acid-base (AB) and hydrophobic interactions.[39]

Liftshitz-van der Waals forces are made up of three different interactions: (1) Keesom forces, the electrostatic interaction between permanent dipoles, (2) Debye forces, the interaction between a permanent and an induced dipole and (3) London dispersion forces, where electronic fluctuations cause interactions between induced dipoles. Despite these forces decaying quickly with increased distance between the two molecules due to the r^{-6} component of their equations, they are considered long range interactions as they take place over tens of nanometres.[40]

In papers published in 1939, Levine and Dube developed a theory for the interaction between two hydrophobic colloidal particles, building upon the Debye-Hückel theory, which describes the charge distribution in ionic solutions.[41,42] They suggested a strong medium-range repulsive force and a weaker long range attractive force between charged colloidal particles. Levine and Dube's theory did not provide an explanation for the instability of colloidal dispersions through irreversible aggregation in high ionic strength solutions.

In 1941, Derjaguin and Landau developed a theory that accounted for the instability, due to a strong but short-ranged van der Waals attractive component.[43]

Verwey and Overbeek independently arrived at the same conclusions seven years later. In a letter to the editor of the Journal of Colloid Science, they attribute the parallel but delayed work being due to being cut off from Allied information during the war by German occupation.[44] Due to this joint but separate discovery, the theory became known as DLVO theory after the first letters of their surnames.[45] Marshall, Stout and Mitchell first applied DLVO theory to the adhesion of bacteria to surfaces in 1971, extending DLVO theory beyond just colloidal particles. Caution must be used when simplifying aggregating bacteria to colloidal particles as they have changing biological appendages and physiochemical properties.[46]

Classical DLVO theory explains the total interaction between the two surfaces (here a cell and a substrate) (ΔE_{total}) as a balance between the attractive van der Waals forces (ΔE_{vdW}) and the repulsive electrical double layer (ΔE_{EDL}):

$$\Delta E_{total} = \Delta E_{vdW} - \Delta E_{EDL}, \tag{1.1}$$

where ΔE_{vdW} can be given as[47]:

$$\Delta E_{vdW} = -\frac{Ar}{6d}, \tag{1.2}$$

where A is the Hamaker constant, r is the radius of the cell and d is the separation between the cell and the substrate.

A charged surface in an ionic solution will cause counter-ions to accumulate close to the surface. The region immediately surrounding the charged surface is called the Stern layer, where counter-ions are strongly bound. Beyond this Stern layer is a more diffuse layer of counter ions which are less firmly associated to the initial surface. As the distance from the charged surface increases the charge decreases asymptotically until the local ionic balance of the bulk liquid is achieved. When two objects with a double layer come into close contact, they repel each other. The interaction between the double layers can be expressed in terms of the surface

potential Ψ, the distance between the surfaces d and the Debye length κ^{-1}, which is the thickness of the double layer and is proportional to the reciprocal of the ionic strength of the solution[48,49]:

$$\Delta E_{EDL} \propto \Psi^2 e^{-\kappa d} \tag{1.3}$$

The more the ionic strength increases, the more the charged surface is shielded, which results in a thinner double layer and smaller Debye length. As a consequence of this, a higher ionic strength medium allows cells to approach the surface close enough so that the attractive van der Waals forces overcome the repulsive electrostatics.

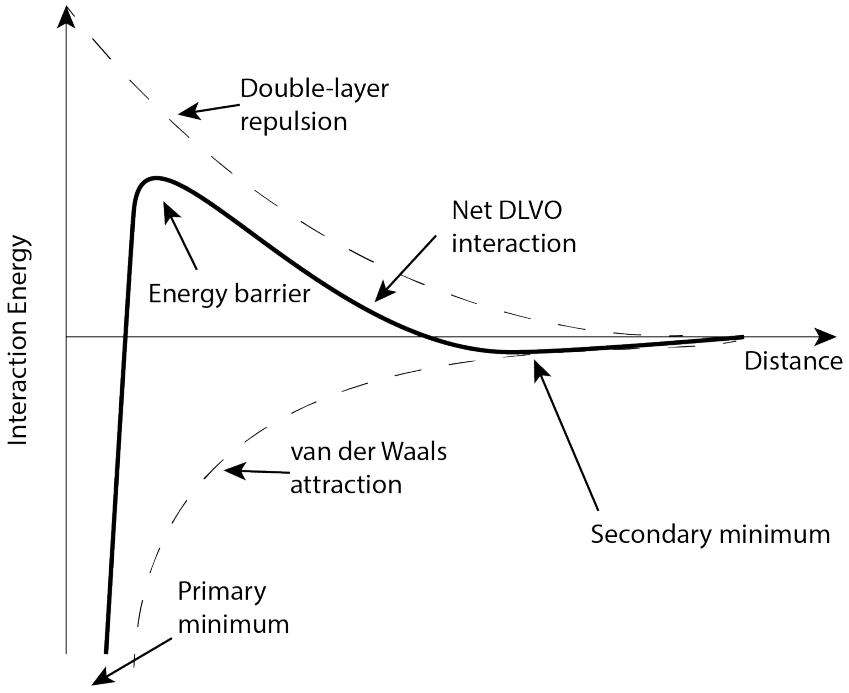

Figure 1.3: DLVO energy profile, showing the net interaction between the attractive van der Waals forces and the repulsive double-layer interaction.

Figure 1.3 shows the energy profile when the attractive van der Waals forces and repulsive electrostatic double layer interactions are combined. The potential energy minimum at contact is the primary minimum and represents irreversible adhesion. The energy barrier to reach this minimum may be too high, which would keep par-

ticles attached reversibly at the secondary energy minimum. If this minimum is too shallow, the particles will remain in suspension.

Although DLVO theory helped to explain some features of adhesion, it was recognised that other forces also influenced these interactions. Polar acid-base interactions include an attractive hydrophobic interaction and a repulsive hydration pressure. These forces can be two orders of magnitude larger than both Liftshitz-van der Waals and electrostatic interactions. Van Oss proposed extending the DLVO theory by adding in terms to account for the contributions of acid-base interactions (AB) and Brownian motion (BM),[50] which became known as the Extended DLVO theory (xDLVO). These new contributions altered Equation 1.1 to become:

$$\Delta E_{total} = \Delta E_{vdW} - \Delta E_{EDL} + \Delta E_{AB} + \Delta E_{BM} \tag{1.4}$$

1.3.1 xDLVO forces and bacterial adhesion

The extracellular polymers and surface appendages of bacteria can help them overcome the energy barriers described by xDLVO theory. These surface bound polymers can have a high affinity for a surface and anchor the cell across the energy barrier. The chemistry of the polymer chains can also change the hydrophobicity or specific interactions that the cell can experience when close to the surface.

Abu-Lail *et al.* explored the relationship between the extracellular polymers of bacteria and their adhesion using AFM.[40] By adding 100 mM of ethylenediaminetetraacetic acid (EDTA) to *E. coli*, approximately 80% of lipopolysaccharides (LPS) can be removed. The adhesion of *E. coli* with and without the LPS removed was then tested against glass slides. The bacteria with reduced LPS had significantly reduced adhesion forces compared to bacteria with intact LPS. It was suggested the LPS forms hydrogen bonds that enable the *E. coli* to overcome the energy barriers.

Ong *et al.* showed that mutant *E. coli* strains with truncated LPS chains can

cause increased or decreased adhesion depending on the properties of the surface. This is due to the polymers altering the surface charge and hydrophobicity of the cell surface.[51] As well as the positive contributions these polymers make to bacterial adhesion, both of these studies also highlight the steric repulsion that surface bound polymers can contribute to the energy profile of adhesion.

While the principles of xDLVO theory are able to describe the initial adhesion of bacteria, the deviation from being colloidal spheres need to be considered when studying real world adhesion of bacteria. The living nature of the cells can have an appreciable impact on the model.[46,51,52]

1.4 Optical methods to measure bacterial adhesion

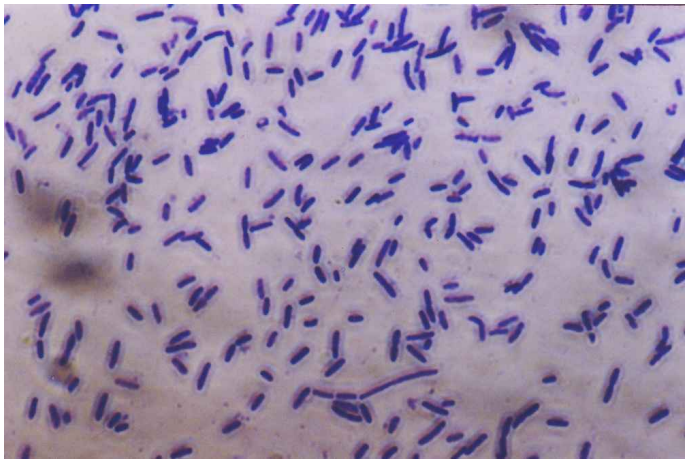

Figure 1.4: Crystal violet staining of various bacterial isolates. Image courtesy of Dr Muntasir Alam.

The study of bacterial adhesion and how it responds to variables such as enzymes and other dispersal agents has historically been conducted using optical methods. Methods usually involve developing a biofilm in the wells of a 96-well plate and staining with a dye that binds to different parts of a biofilm or cell. Different wells are then exposed to different treatments (enzymes, nutrients, toxins etc) and the amount

of dye lost compared to the controls is correlated to the amount of biofilm dispersed.

A popular dye for bacterial study is crystal violet, which has been used since its discovery in the 1880s.[53] It is well known to microbiologists as the dye used in the Gram staining method that can distinguish between bacteria of Gram-positive and Gram-negative type. Crystal violet has a maximum absorbance at 590 nm under usual usage conditions, but can become green or yellow at extreme pH values. In solution, crystal violet dissociates from its chloride ion and has a positive charge. These ions are able to penetrate the cell walls of bacteria and interact with the negatively charged parts of bacterial cells, staining them purple. Cells are usually fixed with an application of methanol or ethanol before being incubated in the stain solution. Unbound dye is removed by washing the samples with water and then leaving them to dry. Finally, 33% glacial acetic acid is used to draw the dye back into solution so it can be measured using a plate reader.[54–56]

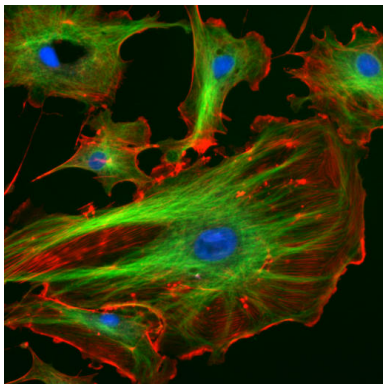

(a)

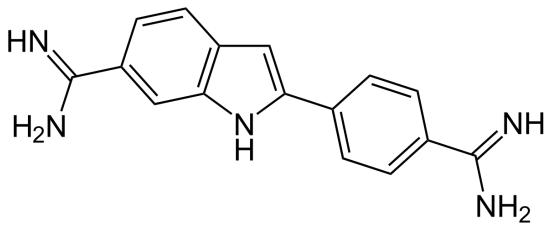

(b)

Figure 1.5: (a) Nucleus of endothelial cells stained blue by DAPI. Image in the public domain. (b) chemical structure of DAPI

Another commonly used dye for bacterial adhesion assays is 4',6-diamidino-2-phenylindole (DAPI), which intercalates to adenine-thymine rich areas of a DNA strand. This dye has a blue emission maximum at 461 nm and excitation maximum of 358 nm when bound to DNA. It therefore requires ultra-violet (UV) excitation to be imaged. The staining method for DAPI is very similar to crystal violet, involving

fixation of the samples before incubation with the dye. Bound DAPI is resolubilised with 95% ethanol before readings are measured.[57]

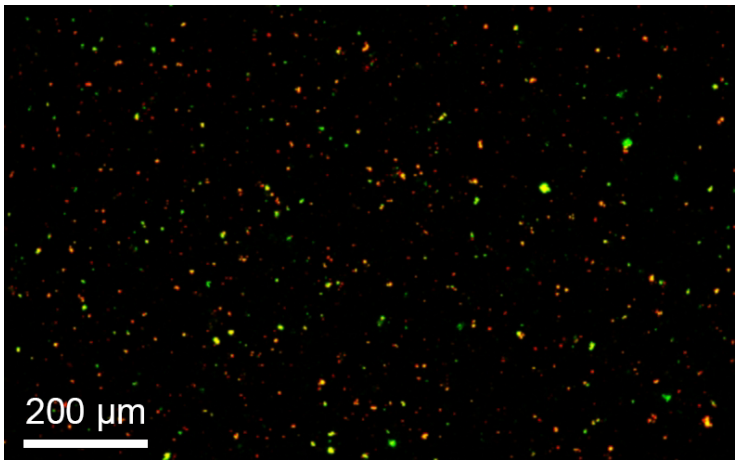

Figure 1.6: LIVE/DEAD image. Green cells are living and have been stained by SYTO 9, red cells are compromised and stained by PI. Yellow emission indicates an overlap of both live and dead cells.

Both crystal violet and DAPI require fixation of bacteria and therefore do not distinguish between live and dead bacteria. There are combinations of dyes that are able to achieve this difference, with a common pairing being propidium iodide (PI) and SYTO 9. The PI stain also binds to DNA, but has no sequence preference. It is unable to penetrate the membrane of cells so can only bind to extracellular DNA or compromised cells which have ruptured their membrane. The stain has an excitation maximum of 571 nm and has an emission maximum of 638 nm (red). SYTO 9 dye marks both live and dead cells as it is able to cross the membrane. It has an excitation maximum of 497 nm and an emission maximum of 543 nm (green). If both dyes are present, PI reduces the fluorescence of SYTO 9, further aiding in the categorisation of bacteria as live or compromised.[58,59]

Traditionally, spectrophotometry or two-dimensional fluorescence microscopy was used to quantify the changes made to biofilms using various treatments. The advent of the confocal laser scanning microscope (CLSM) allows these same assays to provide even more information about changes to the biofilms. The CLSM is able to

block out of focus light from being collected, allowing it to capture two-dimensional images at different heights through a sample. These collection of images are known as Z-stacks and can be reconstructed into a three-dimensional structure.[60,61]

Fluorescence imaging and binding assays are widely used and give important information about the location and amount of different components in a biofilm.[58,61,62] These types of experiment have suggested roles for the different components based on the morphology of the structures that they form. However, to assess a demonstrable role for these molecules, it is necessary to interact with the biofilm in a different manner. Force spectroscopy can give detailed information of the changes that biofilms undergo when exposed to the same chemicals and enzymes as in the fluorescence and binding assays and can complement the findings discovered using those techniques.

1.5 Scanning force microscopy

In 1986, Gerd Binnig, Calvin Quate and Christoph Gerber introduced the atomic force microscope (AFM) in a paper,[63] building upon the scanning tunnelling microscopy that Binning and Heinrich Rohrer had developed years before.

1.5.1 Introduction

They explained how the AFM uses a sharp tip at the end of a flexible cantilever to probe the surface topography and many other properties of a sample at nanometre scale. The movement of the cantilever as it rasters across the surface is detected by a laser source reflecting off the back of the cantilever and onto a photodiode. This translates the change in laser position to data on the topography of the surface, or how a cantilever responds during a force measurement.[63] It improved on the design of the scanning tunnelling microscope by removing the need for the sample to be electrically conductive. This allowed biological samples to be studied at resolutions beyond the diffraction limit of visible light.[64]

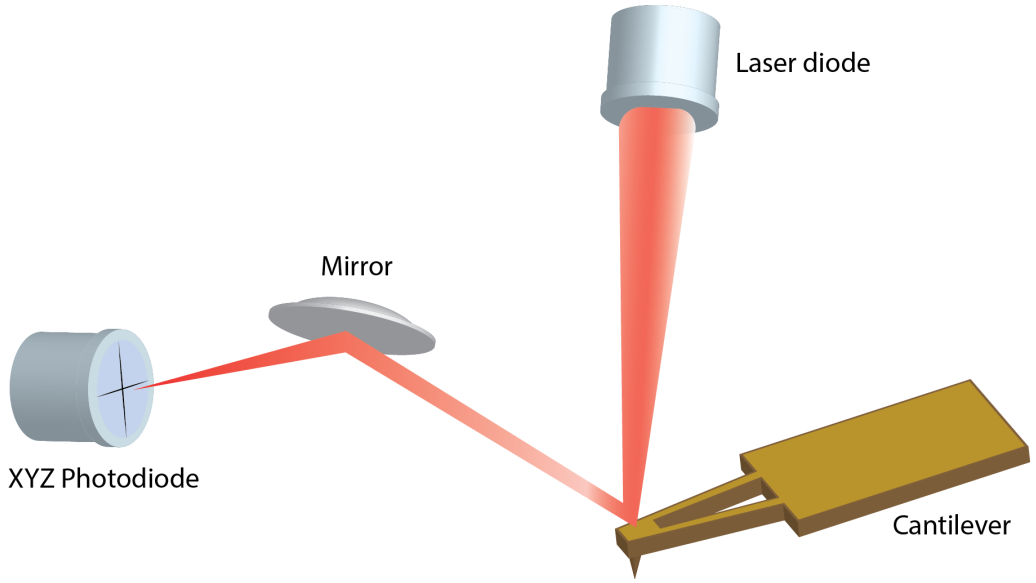

Figure 1.7: Diagram of the core components of an AFM. A laser diode reflects off the back off the cantilever on an XYZ photodiode with the aid of a mirror.

Cantilevers obey Newtonian mechanics and Hooke's law, so that

$$F = -kd, \tag{1.5}$$

where F is the force applied to the spring, k is the spring constant of the cantilever and d is the deflection experienced by the spring.

The selection of the cantilever to be used for an AFM experiment is important. Cantilever chips come with multiple arms of different spring constant on them. The spring constant to be used for a specific experiment must be carefully chosen in the experiment design, to meet the sample needs. Soft and delicate biological samples require a softer cantilever to prevent puncture damage or dislodging loosely bound cells. Indentation or roughness studies of surfaces require cantilevers with higher spring constants.

At the end of most cantilevers there is a sharp tip which sense the sample sur-

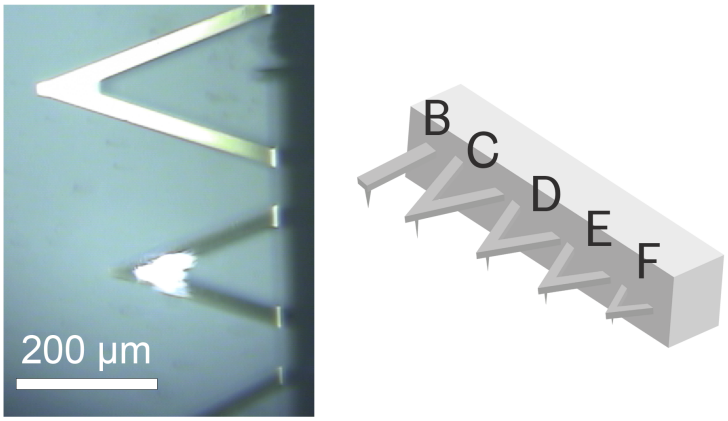

Figure 1.8: Optical camera view of MLCT cantilevers mounted in an MFP-3D AFM, alongside a schematic diagram of the cantilever arm layout. The top of the image shows arm C, with the laser shining on arm D.

face and cause the cantilever to bend up or down in response to the interactions it experiences. The laser reflecting onto the back of the cantilever converts these subtle cantilever movements into computer signals, via a four quadrant photodiode. The photodiode produces a voltage depending on where the laser is falling onto the quadrants. Vertical movements are produced by the topography or adhesion to the the sample, whereas lateral displacements are caused by the cantilever twisting due to frictional forces.[63]

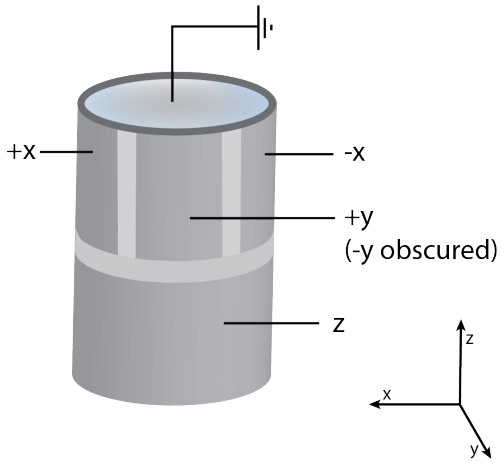

Figure 1.9: Schematic diagram of the piezoelectric tube that manipulates the cantilever in three dimensions.

The other major component of an AFM is the piezoelectric materials, which allow the tip to be adjusted with sub-nanometre precision. The piezoelectric effect is a linear phenomenon in which the mechanical displacement is proportional to the applied voltage. Piezoelectrics in an AFM are either a tube or a stack. Fig. 1.9 shows a hollow polycrystalline lead zirconate titanate (PZT) tube which is split into quadrants using silver plating. When voltage is applied to the electrodes, the thickness of the PZT quadrant increases and as a consequence, the length of the quadrant decreases. The high voltage electronics amplify the low level XYZ voltages generated by the digital signal processor so that it can manipulate the piezoelectrics, with voltages in the range of 100 V. The piezoelectrics rely on a potential difference across the two phases of the tube to change the dimensions of the material, enabling it to extend or retract and move in the X and Y axis. The tube can be extended if the same voltage is applied to all four quadrants, allowing movement in the Z direction. The sub-nanometre precision of piezoelectrics is crucial to the operation of the AFM.[65]

1.5.2 Feedback Loop

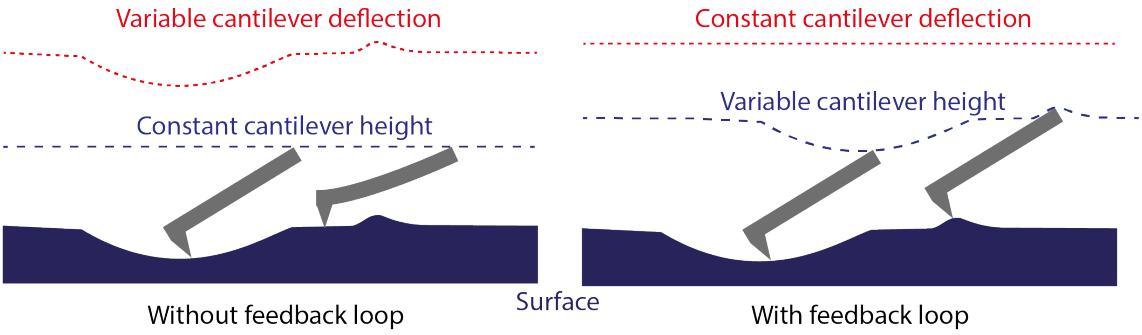

Figure 1.10: Contact mode feedback loop. With no feedback loop engaged, the height of the cantilever is kept constant, with height data collected through the cantilever deflection. With the feedback loop engaged, the piezo moves to keep the deflection constant.

The feedback loop keeps a parameter constant at a set value during scanning. Depending on which mode the AFM is being operated in, either the deflection or amplitude of the cantilever are kept constant by the feedback loop. Components

of the AFM measure the z-piezo position and compare it against the user selected set point. Any difference in these values is called the error signal. The feedback loop changes the voltage applied to the z-piezo to reduce the error signal so that the measured value returns to the set point. An ideal feedback loop would respond instantly, but this is not achievable in reality.

There are two components of the feedback loop in modern AFMs, the integral and proportional gains. These values affect how quickly the feedback loop responds to the changes in cantilever deflection. The proportional gain calculates the difference between the measured deflection and the desired value, the set point. This allows reactions to surface changes directly under the tip. This gain is suited for control on relatively flat surfaces or at slow scan speeds. The integral gain calculates the integral of the difference over time. This is much slower than the proportional gain and allows correction on rough surfaces and at high scan speeds.

1.5.3 Modes of operation

The imaging modes of an AFM can be categorised into two types; static or dynamic. The names refer to the oscillation of the cantilever tip during scanning, with the tip oscillating in dynamic modes and not in static modes. The most popular static mode of scanning is contact mode.

In this mode, the tip is in physical contact with the sample as it is moved across the surface. If the feedback loop is active, a constant force is applied across the surface as the z-piezo moves the tip vertically as it encounters features of different sizes. If the feedback loop is not active, higher parts of the sample experience higher forces as the the applied force is proportional to the deflection.

The most popular dynamic mode of scanning is tapping mode (also called AC mode). In this mode, the tip is oscillated away from the surface near its resonant frequency (f_0), with a given amplitude (A_0). As the probe comes near the surface,

the amplitude signal (A) is recorded. If the scan is being operated without a feedback loop active, tall features will dampen the oscillation and troughs will cause it to increase. This change in the amplitude can be converted to a height profile of the surface. If the feedback loop is engaged, the tip is moved by the z-piezo motor to maintain the amplitude at a constant value. The height profile of the surface is captured from the z-piezo movements.

Biological samples tend to use tapping mode to image due to the reduction in vertical forces and the removal of any lateral forces, which can detach or damage samples.

1.5.4 Cantilevers

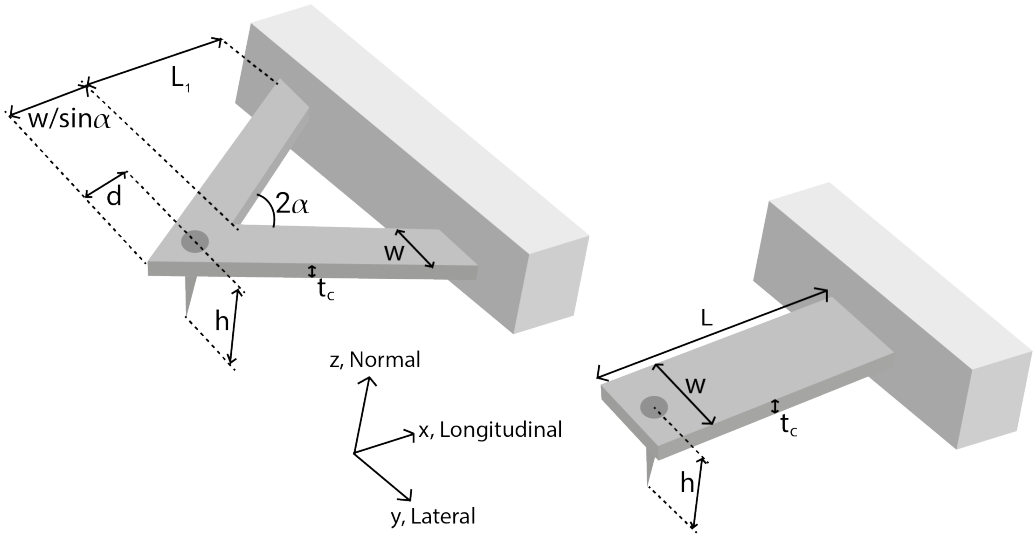

Figure 1.11: Dimensions of rectangular and triangular cantilever arms. Based on a figure by Sharpe *et al.*[65]

The spring constant of cantilevers can be calculated if the dimensions and materials are know. For a rectangular cantilever, the spring constant, k_{rect} is:

$$k_{rect} = \frac{Et_c^3 w}{4L^3}, \tag{1.6}$$

where E is the Young's modulus of the cantilever material (1.5×10^{11} N/m for Si_3N_4),

t_c is the cantilever thickness, w is the width and L is the length, as depicted in Fig. 1.11

For a V shaped (triangular) cantilever, the equation for spring constant, k_v is

$$\mathrm{k}_v = \frac{Et_c^3 w}{2L_1^3} \cos\alpha \; 1 + \frac{w^3}{2(L_1 \tan\alpha + \frac{w}{\cos\alpha})^3} \times (3\cos\alpha - 2)^{-1} \left(\frac{L_1}{L_1 - d}\right)^3, \quad (1.7)$$

where α is the half angle and L_1 is the length indicated in Fig. 1.11.[65]

The thermal fluctuation method of calibration introduced by Hutter and Bechhoefer in 1993 has become a popular method for calibrating optical lever probes.[66] A cantilever not subjected to a driving force experiences random thermal vibrations. The Hamiltonian of a system like this is given by:

$$H = \frac{p^2}{2m} + \frac{1}{2} m\omega_0^2 q^2, \quad (1.8)$$

where p is the momentum of the cantilever, m is its mass, ω_0 is the resonant angular frequency of the system and q is the displacement of the cantilever.

The mean average value of each quadratic term in the Hamiltonian is equal to the half the thermal energy, given as:

$$\left\langle \frac{1}{2} m\omega_0^2 q^2 \right\rangle = \frac{1}{2} k_B T, \quad (1.9)$$

where k_B is Boltzmann's constant and T is the temperature.

Since $\omega_0^2 = k/m$, the spring constant can be calculated from the measurement of the mean-square cantilever displacement, shown as:

$$k = \frac{k_B T}{\langle q^2 \rangle} \quad (1.10)$$

1.5.5 Force mode

The capability of the AFM to conduct force spectroscopy experiments is more important to this thesis than its ability to capture detailed images. The output of force measurements is a force-distance curve, which represents the force on the cantilever in relation to its distance from the sample.

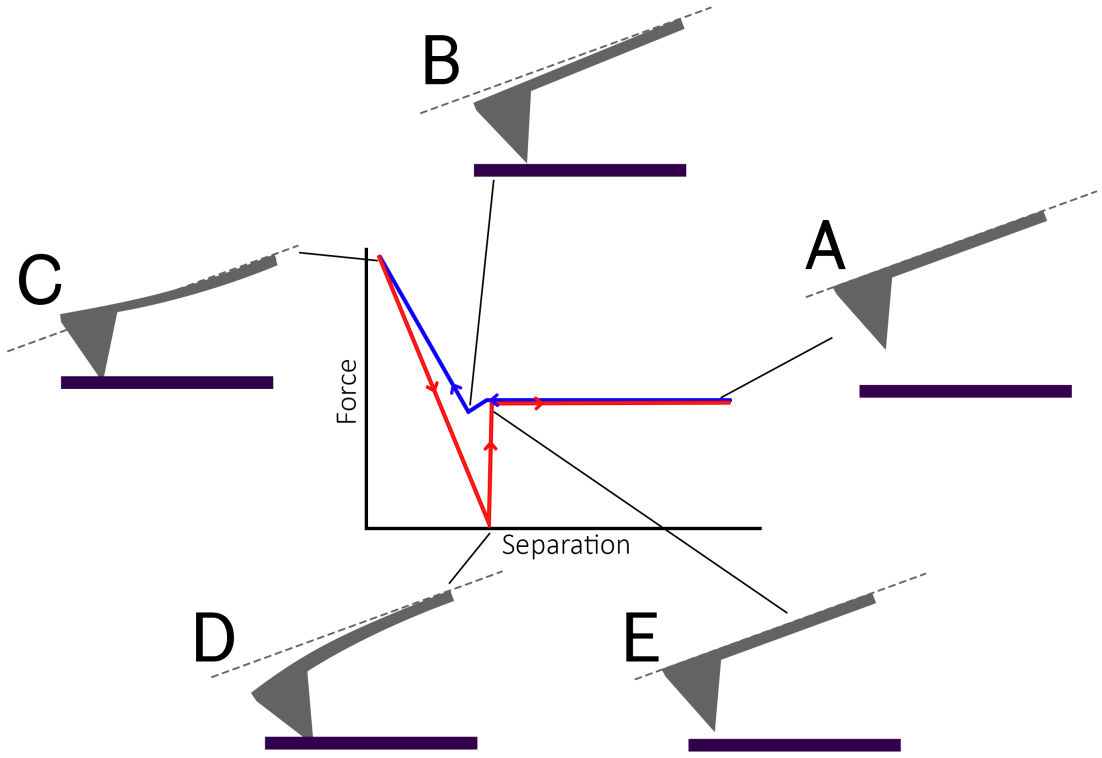

Figure 1.12: Diagram of cantilever positions through a typical force-distance curve. Blue line is approach, red line is retract. A) no interaction, away from surface B) jump to contact C) trigger point D) adhesion to substrate overcome E) retraction continues.

Force-distance curves are generally separated into two segments, the approach towards the sample and then the retraction. Starting at (A) in Fig. 1.12, the cantilever is far enough away from the sample that there are no forces experienced. The cantilever then begins its approach towards the sample. At (B), the interaction with the sample begins. Depending on the surfaces and conditions, a jump-to-contact can

be observed in some curves, depicted at point (C). The cantilever moves into the repulsive regime at (D) until the trigger point is reached at (E). The movement of the cantilever is then reversed and the data is shown on the retraction part of the curve. If there are attractive forces present, the z-motor must overcome these as shown at (E). Eventually all attractive forces will be overcome and the cantilever will totally separate from the sample. The cantilever eventually returns to point (A) and the approach and retract plots will overlap at a force of zero.

1.5.6 Functionalisation of cantilevers

Although the AFM is normally operated using cantilevers with sharp tips at the end, more recent techniques involving tipless cantilevers have been developed, with those of the bioprobe variety being of particular interest to this project.

1.5.7 Biological functionalisation

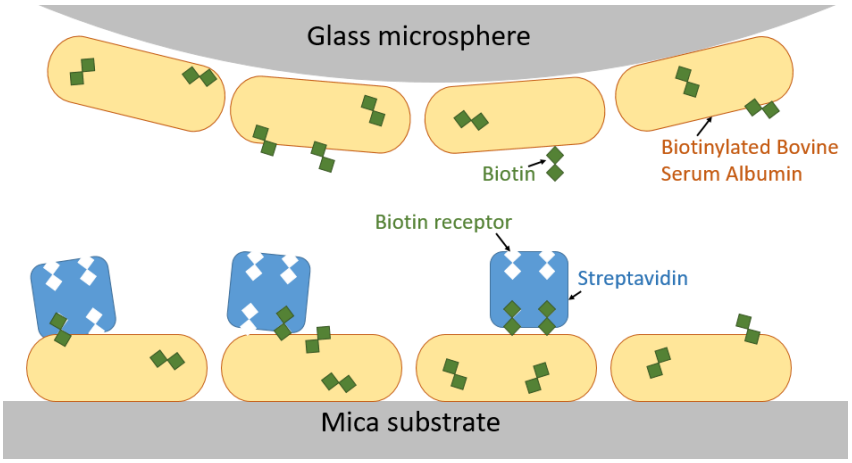

Figure 1.13: Schematic of a biotin coated glass bead on a cantilever approaching a streptavidin-BBSA-mica substrate. Adapted from Fig. 5 of[67].

A cantilever tip was first functionalised in 1994, where the interaction of biotin and streptavidin was investigated, as it has one of the strongest non-covalent interactions known.[67,68] Glass spheres attached to cantilevers and mica surfaces were functionalised with biotin and streptavidin using bovine serum albumin (BSA). BSA spontaneously adsorbs to glass and mica surfaces and can covalently attach biotin

groups to become biotinylated BSA (BBSA), using biotin-ε-aminocaproic acid *N*-hydroxysuccinimide ester. Streptavidin functionalised mica surfaces can also be synthesised by incubating with BBSA-mica films. These functionalised surfaces are schematically depicted in Fig. 1.13. Streptavidin-BBSA-mica surfaces can be blocked with a short incubation in biotin to prevent the specific interaction with a functionalised cantilever tip.

Lee *et al.* used these different surfaces to demonstrate the ability of an AFM to detect specific interactions. Biotin-streptavidin interactions were detected with a force of 0.34 ± 0.12 nN. When the streptavidin surface was blocked with excess biotin, no rupture forces were observed, with peak forces now only registering at 0.06 ± 0.04 nN. There were many other biotin-protein reports following this initial publication, with biotin-avidin interactions being explored in addition to streptavidin.[69–71]

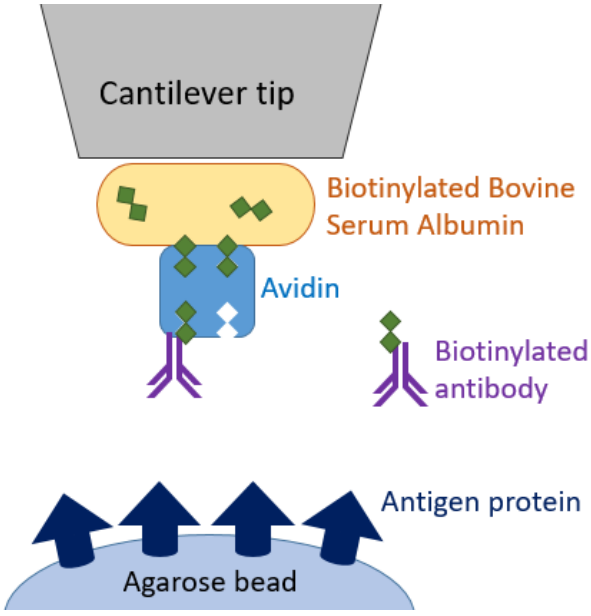

Figure 1.14: Schematic of a biotin-avidin coated cantilever tip being further functionalised by biotinylated antibodies. Adapted from Fig. 2 of[72].

The ability to construct BBSA-protein complexes on a cantilever tip were used to create a scaffold to attach other molecules to the cantilever tip. Biotinylated antibodies can attach to a BBSA-avidin coated tip as shown in Fig. 1.14. This

antibody functionalised tip can then investigate the specific interaction between the antibody and its antigen. The specific interaction between antibody and antigen is observed using this method, but the authors could not establish a single molecule interaction so were unable to define a value for the interaction.[72]

In 1996, Hinterdorfer *et al.* further developed the functionalisation of cantilever tips with antibodies by introducing an 8 nm long polyethylene glycol (PEG) flexible linker.[73] The freedom of the antibody to correctly orientate and the close control of ligand concentrations led to the expectation that only one antibody had access to the antigen coated surface. With these adjustments, single antibody-antigen events were successfully observed.

By 1997, the biological functionalisation of cantilever tips had progressed to include attaching cells. The first report of a cell being attached to a cantilever tip was a single *Saccharomyces cerevisiae* yeast cell.[74] The practice of attaching a single cell to a cantilever for force measurements has become known as single cell force spectroscopy (SCFS). Cantilevers were also coated in lawns of cells, such as *E. coli*[75] and mammalian trophoblast-type cells.[76]

There are both positives and negatives of SCFS and coating cantilevers with multiple cells. The main detractor of SCFS is the time consuming production of the probe. Cells are allowed to settle on a substrate at an appropriate concentration so that individual cells will not have neighbours closely settled nearby. A cantilever coated in some form of adhesive is carefully positioned over a selected cell and moved into contact with the cell. If the cell successfully binds to the cantilever, the tip has been successfully converted to a cell probe. An alternative method favours the addition of a colloidal bead between the tip and the bacterium. This involves the additional steps of applying a small amount of glue to the cantilever tip and attaching a colloidal bead. The method then continues as described previously. The described advantage of the colloidal bead is an increase in the reproducibility of the

measurements as it ensures proper contact between the single cell and the surface of interest.[77,78] The presence of the large bead (in comparison to the small bacterium) may influence the types of forces detected by the AFM, particularly in solutions of low ionic strength due to the large electrostatic double layer.[79]

The advantage of SCFS is the measured forces can be directly compared between different bacteria and surfaces. This method for studying the initial adhesion between a bacterium and a surface, but is less relevant for the study of biofilms as the EPS produced changes the chemistry surrounding the bacteria.[80]

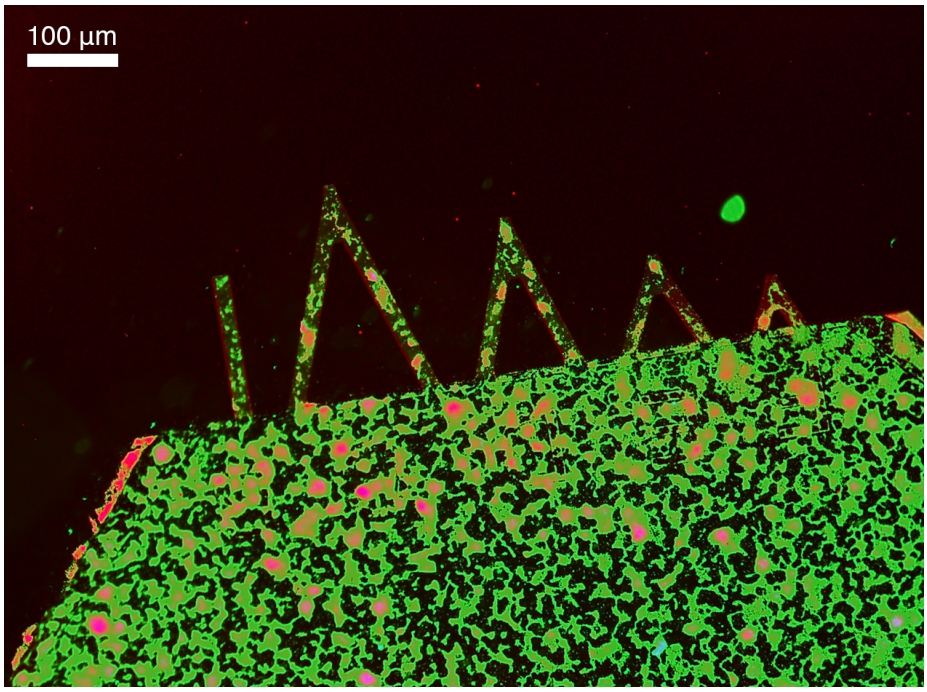

Figure 1.15: NPO-10 cantilever stained with LIVE/DEAD (green/red), demonstrating the coverage of *M. luteus*. This image is taken after treatment with cellulase enzyme.

Multi-cell coated cantilevers are more appropriate for the study of biofilms with AFM measurements. While some methods involve depositing a bacterial pellet of known size directly onto the cantilever,[75] an alternative is to allow a biofilm to self assemble itself on the cantilever.[23] In this method a cantilever coated in poly-L-lysine, to aid in the initial attraction of bacteria to the silicon nitride surface, is immersed in bacterial culture. After an initial deposition of bacteria, the cantilever

is moved to a dilute growth media and incubated over night to allow a young biofilm to establish on the surface of the cantilever.

1.6 Motivations for studying adhesion in medical research

Adhesion of biofilms not only has significant effects in industrial settings, but also in public health. There are many examples of bacteria that are pathogenic towards humans, such as *Streptococcus pneumoniae* that causes respiratory infections,[81] *Staphylococcus aureus* that causes a range of infections of soft tissues and implants,[82] as well as *Burkholderia cenocepacia* and *Pseudomonas aeruginosa* that cause infections in those with cystic fibrosis. It is estimated that as much as 80% of all human bacterial infections are biofilm-related.[83]

Parasites such as *Leishmania* species, that causes leishmaniasis and *Plasmodium* species that cause malaria, rely on being able to regulate adhesion to be transported in their vector, such as sand flies and mosquitos, and then move into a human host when the opportunity arises.[84,85] Without being able to adhere to the vector, the parasite would not be able to mature and be transmissible.

By increasing the knowledge of how bacterial and parasitic adhesion occurs, new targets for treatment and therapeutics that exploit this can be developed.[45] For biofilm based infections, disruption of the extracellular polymeric substances is an obvious target, although disrupting the adhesive targets in the human host could also be a promising route.[86,87] For parasites, the binding in the parasite-vector relationship is of high importance.[85] Atomic force microscopy is uniquely suited to acquiring adhesion data in biologically and physiologically relevant environments.[59]

1.7 The use of enzymes in industrial cleaning

Enzymes have been used by industry for cleaning purposes since 1913, when Röhm and Haas added the protease trypsin from pig pancreas into their detergent, Burnus. Trypsin was not particularly stable or active in the detergent mixtures of the time. In 1963, a more alkali and builder tolerant bacterial protease called Alcalase was developed. After only five years of the initial introduction to detergents, over half of all heavy-duty laundry detergent for domestic use in Europe contained some form of protease enzymes.[88]

By the 1950s, it had been established that secretions of sweat from the human body were odourless and the resulting odour was as a result of break down by bacteria.[89] Enzymes were not yet required to combat bacteria on clothing due to the high wash temperatures used at the time. Heavily soiled items such as kitchen towels, underwear and bed sheets would regularly be washed at 95 °C, with coloured items being washed at 60 °C.[90]

The growth of enzyme containing detergents continued until the early 1970s, when safety problems in industrial handling of enzymes became apparent. Sensitisation of workers to enzyme dust caused a temporary discontinuation of enzymes until better industrial hygiene practices and procedures could be developed. The first α- amylase for detergents was introduced by Novozymes and by the mid-1970s, liquid detergents in Europe and the USA contained specially designed liquid enzyme preparations.[88]

In the late 1970s, with dramatically rising energy costs, that domestic wash temperatures dropped to 60 °C for heavily soiled items and 40 °C for coloured and less soiled items. With this decrease in temperature, wash duration and the amount of mechanical action was increased to compensate, alongside the addition of bleaching agents.

By the 1980s, a range of new enzymes were introduced adapted to these new more ecologically friendly conditions, including a cellulase, a bleach compatible protease and a lipase. In the 1990s, new detergent markets were opened in India, South America, China and former Soviet Union countries. There regions came with very different and unique washing conditions including lower washing temperatures and low detergent concentrations to keep costs at a minimum. This led to a second generation of the 1980s detergents being developed to maintain cleaning levels at these new conditions.[88]

1.7.1 Motivations for enzyme use

Although the use of chemicals such as bleach in industrial detergents still persists, they are not prevalent in domestic settings due to bleaching systems not being applicable to liquid detergents which are becoming more favoured by the public.[91,92] With the removal of activated bleaches from detergent formulations and the comparatively lower wash temperatures the ability of bacteria to produce undesirable odours becomes an issue that needs resolving once again. The amount of bacteria remaining on fabrics and contaminating the washing machines without bleach and heat is significantly higher.[93–95]

As well as the textile cleaning industry requiring non-bleaching, low temperature cleaning from enzymes, the shipping industry began to investigate how enzymes could help prevent biofouling of ship hulls. Traditionally, chemical biocides had been used, such as tin and copper containing complexes or oxidants using chlorides, bromides or ozone.[57] It is important environmentally and financially to prevent biofouling on ships' hulls as the additional drag increases fuel consumption. Figures from 2013 estimate that antibiofouling coatings save $60 billion USD of fuel, equating to 384 million tonnes of carbon dioxide and 3.6 million tonnes of sulphur dioxide emissions.[96] A specific ban of organostannic agents, which were found to be toxic

to marine flora and fauna, came into force in the European Directive 1998/8/EC. Antifouling paints needed a more environmentally friendly approach to preventing biofilm formation, with enzymes being the answer.

Although enzymes were originally incorporated into laundry detergents to tackle hard to remove stains, many of these enzymes also act on different parts of a biofilm. A range of enzymes have been shown to have hydrolytic effects on different biofilms, including α-amylases,[56,97,98] proteases,[99,100] lipases,[101] cellulases[102,103] and mannanases.[59,104] An enzyme not already part of detergent formulations is DNase, which was first shown to have dramatic biofilm dispersal abilities in 2001 in what has become a landmark report.[105]

1.8 Research aims and thesis structure

The primary aim of this thesis is to further the understanding of how bacteria adhere to textile substrates and how industrially available enzymes might disrupt these communities. By investigating the changes in adhesion of bacteria before and after exposure to different enzymes, the roles of the substances targeted by the enzymatic treatment could be determined. The methodologies and results of the primary aim of the project are provided in Chapters 2 and 3.

Of the enzymes tested in this project, a novel DNase that targets the phosphate backbone of deoxyribonucleic acid (DNA) was found to be highly potent in reducing bacterial adhesion. This enzyme was studied in real world conditions to explore the factors that affect the enzymatic activity. Studies were also conducted to establish the mechanism of action used by the molecule on substrates. The industrial methods, computer modelling and mechanistic results are provided in Chapter 4.

Custom software was created throughout the project to aid in rapid and automated analysis of the large amounts of data captured by the AFM experiments.

The software and experimental methods refined through the project were adapted and used to process and provide data in collaborations that studied the adhesion of different types of pathogens. The investigation of *Leishmania mexicana* to the gut of its sand fly vector benefited from the software, allowing analysis that would have previously been time prohibitive. These findings helped demonstrate the life stage dependency of the adhesion targets and is provided in Chapter 5. Also in this chapter, bioprobe experimental techniques that were advanced through the thesis were used to provide additional data on a prospective treatment that reduces the adhesion of pathogenic *Staphylococcus aureus* to human epithelial cells.

Chapter 2

Experimental methods

2.1 Microbiology

Micrococcus luteus were the primary bacteria of interest for the experiments documented in this thesis and were grown on tipless cantilevers to construct bioprobes. Secondary data were obtained by growing *M. luteus* on silicon wafer and glass slides for contact angle and confocal microscopy experiments respectively. The method of preparation is the same until the substrate is introduced and is outlined here.

2.1.1 General protocol for bacterial growth

M. luteus (ATCC 4698) was a gift of Dr Bob Turner of Molecular Biology and Biotechnology, The University of Sheffield. Bacterial strains were stored at −80 °C (80 % bacterial suspension, 20 % glycerol, by volume) and plated onto tryptic soy agar (Table 2.1, all components sourced from Sigma Aldrich, Gillingham, UK) for 3 days at 30 °C. Plates were stored at 4 °C and disposed of after 1 month. As the solid medium is non-selective, the plates were visually inspected for contamination and discarded if culturing shows signs of growth not belonging to *M. luteus*. *M. luteus* produces round yellow colonies where the plate has been streaked, has shown in Fig. 2.1.

Figure 2.1: Streaked yellow colonies of *M. luteus*

Table 2.1: Composition of tryptic soy agar.

Component	**Concentration (g/L)**
Typtone	17.0
Soytone	3.0
Dextrose	2.5
NaCl	5.0
K_2HPO_4	2.5
Agar	15.0

An initial growth of the bacteria takes place in a culture tube, with 3 mL of trpyic soy broth (TSB, 30 g/L, Sigma Aldrich) for 12 h at 30 °C in an orbital shaker (Luckham R1000 Orbital Shaker, Luckham Ltd., Burgess Hill, England) at 50 rpm. 100 µL of the initial culture was used to inoculate 100 mL of TSB, which was incubated for a further 18 h with gentle shaking.

2.1.2 General protocol for growth of biofilms on substrates

Regardless of the purpose of the biofilm on the substrate, the general protocol is similar across small AFM cantilevers or entire glass slides. For cantilevers and silicon wafer tokens, the following steps occured in fresh wells of a flat bottomed 48 well plate. For the preparation of glass slides, ethanol and poly-L-lysine hydrobrombide

Table 2.2: Differing volumes of solutions required in biofilm construction

Solution	**Volume required for substrate**		
	Cantilever or wafer (µL)	Glass slide (pipetted) (µL)	Glass slide (in petri dish) (mL)
Ethanol	500	1000	-
Poly-L-lysine	200	400	-
Bacterial culture	500	-	15
Dilute growth media	500	-	15

(30-70 kg/mol, Sigma Aldrich) was pippetted onto the surface and the glass slide was then placed in a petri dish to allow the bacterial culture and dilute growth media to be poured around and onto the slide. The volumes that were used are shown in Table 2.2.

The substrate was immersed in 70% ethanol for 10 min as a simple sterilisation step and allowed to dry. A 1% (w/w) poly-L-lysine hydrobromide solution was placed on the top surface of the substrate for 2 h. The substrate was then immersed in bacterial culture (see §2.1.1) and incubated for 4 h at 30 °C before being moved to 10 % concentration growth media overnight at 30 °C. The samples were then stored at room temperature through the day as they are used in the required experiment.

2.1.3 Cell viability staining

To image bacteria using a fluorescence or confocal microscope, LIVE/DEAD *Bac*Light (ThermoFisher Scientific, Waltham, MA, USA) dye kits are used. The dyes are temperature and light sensitive, so must be stored at −20 °C away from light. The kit is made of two dyes, green fluorescent SYTO 9 and red fluorescent propidium iodide, which both stain nucleic acid. SYTO 9 is able to penetrate virtually all cell membranes and therefore tags all cells, alive or dead. Propidium iodide is unable to penetrate cell membranes, so can only gain entry to a cell with a compromised membrane, so therefore only tags dead cells. When used in conjunction and with post processing, cells which have been compromised can be identified from those that are healthy.

Table 2.3: Excitation and emission maxima for components of LIVE/DEAD *Bac*Light and their amounts in 300 μL DMSO solution in kit components

Dye	Maxima (nm)		Amount (mM)	
	Excitation	Emission	Component A	Component B
SYTO 9	480	500	1.67	1.67
Propidium iodide	490	635	1.67	18.30

The kits consist of two vials named Component A and Component B and are recommended to be used in a 1:1 ratio. However, if one of the dyes is being detected too much or too little, adjusting the amount of Component B, which has an elevated concentration of propidium iodide, can aid in finding an approximate optical balance.

2.2 Surface Preparation

The ability of spin coating to produce flat surfaces that mimic materials that may be curved or fibrous in nature is a great asset for analysing surfaces in the likes of an ellipsometer or AFM.[106] Spin coating is efficient and gives reproducible results and is used throughout experiments in this thesis to form analogues of textiles such as polyester and cotton. Force mapping textile patches of these substances is much less suitable for use in AFM force experiments, due to the overhanging fibres causing hazards for the fragile bioprobes.

In this thesis, cellulose thin films were used as an analogue for cotton fabric and PET was used as an analogue for polyester fabric. Some commercially available PET contains glass particles included as a reinforcing agent and are not suitable for forming thin films.

2.2.1 Spin coating polymer thin films

The thickness of a thin film made by spin coating can be controlled by a variety of factors. The concentration of polymer in solution is the major factor in controlling the thickness,[107] with other factors having a less prominent effect, such as spin ve-

locity[108] or evaporation rate of the solvent.[109]

Thin film thickness is not the only characteristic that is desirable to be controlled with spin coating. The morphology and roughness of a thin film can be tailored using different solvent choices and varying the solution concentration and spin time.[107,109].

2.2.2 Protocols for spin coating polymer thin films

Poly(ethyleneterephthalate) (PET)

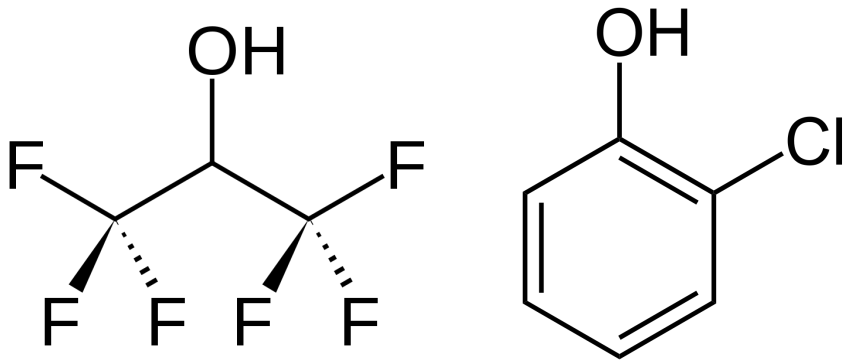

(a) hexafluoroisopropanol (HFIP) (b) 2-chlorophenol

Figure 2.2: Chemical structures of the two solvents used in creating PET thin films.

For the preparation of thin films, 2-chlorophenol was obtained from Fluorochem (Hadfield, UK), poly(vinylamine) was obtained from BASF (Ludwigshafen, Germany) and all other solvents were purchased from Sigma Aldrich. Silicon wafers were obtained from Prolog Semicor (Ukraine).

There are many different protocols for preparing PET thin films in the literature and the most reliable thin films were formed by combining two methods.[106,110] Both methods use hexafluoroisopropanol (HFIP) as the main solvent, but differ in solution concentration and annealing temperatures. Song *et al.*[106] use 0.16 % (w/w) PET in HFIP, spinning at 3000 rpm for 20 s. These films are then annealed in an

oven at 80 °C for 2 h. It is important not to Piranha clean silicon to be coated in PET as the cleaning causes the PET solution to reject the surface.

Ibaragi[110] explored many different concentrations and supplementary solvents for creating PET thin films in their thesis.[110] Using these calculations, a 3 % (w/w) of PET in HFIP was dissolved at 100 °C for 1 h in a sealed container, before being diluted to 1 % (w/w) using 2-chlorophenol. The addition of 2-chlorophenol, with a higher boiling point than HFIP (HFIP bp = 58.2 °C, 2-chlorophenol bp = 174.9 °C), allows more time for the thin film to form and results in a thinner film. These samples were spun at 2500 rpm, with acceleration at 1000 rpm/s for 60 s. Annealing at 200 °C removes the higher boiling point solvent and also hemispherical features that are observed if annealing takes place at lower temperatures that can be seen in Figure 2.3.

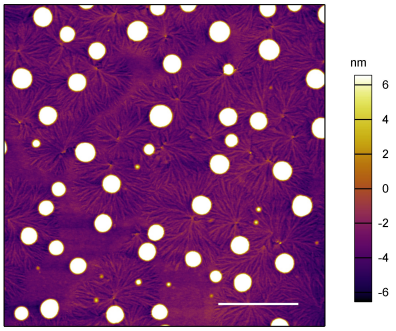

(a) 80 °C annealing, height

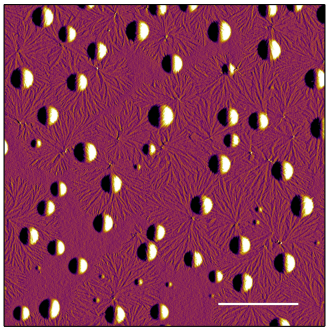

(b) 80 °C annealing, deflection

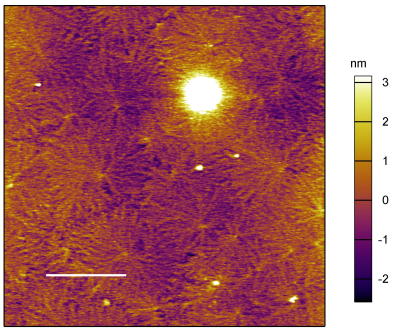

(c) 200 °C annealing, height

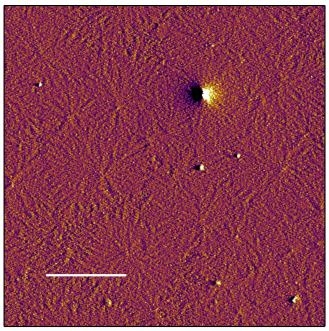

(d) 200 °C annealing, deflection

Figure 2.3: AFM images of PET thin films. 2.3(a) and 2.3(b) were annealed at 80 °C for 2 h. 2.3(c) and 2.3(d) were annealed at 200 °C for 1 h. Scale bar indicates 5 µm.

Cellulose

The preparation of a cellulose thin film combines three similar sources from literature.[106,111,112] Silicon wafers are cleaned using Piranha solution (70% H_2SO_4 (95% - 98%) and 30% H_2O_2 (30%)) for 1 h. The clean wafers are immersed in a 0.01 g/L solution of poly(vinylamine) (PVAm) in water for 20 min. PVAm acts as an anchoring layer, giving homogeneous films and fastening the cellulose to the wafer after drying.[111]

After immersion in PVAm, the wafers are removed and rinsed in DI water, before being dried at 50 °C for 45 min. A solution of 50% *N*-methylmorpholine *N*-oxide (NMMO)/water (v/v) is prepared and 0.01 g of cellulose dissolved in it at 115 °C.

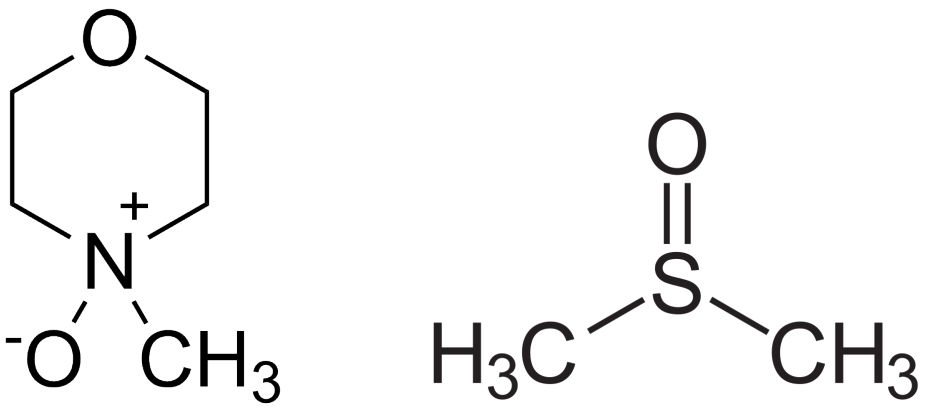

(a) *N*-methylmorpholine *N*-oxide (NMMO)

(b) dimethyl sulfoxide (DMSO)

Figure 2.4: Chemical structures of the two solvents used in creating cellulose thin films.

A pale yellow solution is obtained which should be removed from heat immediately once the cellulose has dissolved, or a brown precipitate begins to form. To this solution, 9.99 g of dimethylsufoxide (DMSO) is added dropwise and stirred for a further 10 min. This solution is spin coated at 2500 rpm for 30 s. The wafers are then immersed in deionised water which precipitates the cellulose film. The wafers are left immersed for 4 h with frequent water changes before being dried under nitrogen and stored in a desiccator.

2.2.3 Ellipsometry

Ellipsometry is a non-destructive optical technique that relies on the reflection and refraction of polarized light. By analysing the differences in the polarisation of light which is incident and reflected from a sample, characteristics of the film such as thickness and refractive index can be calculated.

Ellipsometry was used to verify the targeted film thickness had been achieved on the silicon wafer. A M2000 V rotating compensator ellipsometer (J.A. Woolam Co., Inc., Lincoln, UK) was used. Measurement were taken at an angle of incidence of 70° to the surface normal, shown schematically in Figure 2.5. CompleteEase software (J.A. Woolam Co., Inc., Lincoln, UK) was used to apply a multilayer

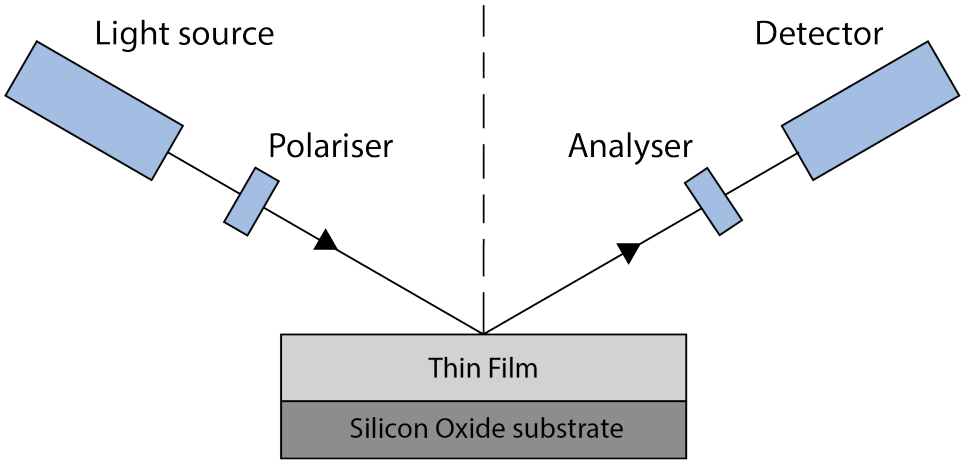

Figure 2.5: Schematic diagram of ellipsometry of a thin film on a silicon wafer. The changes to polarised light give characteristics of the thin film being investigated.

model to account for the native SiO_2 layer and a Cauchy approximation was used to approximate the thin film. Cauchy's equation is a relationship between refractive index of a transparent material and wavelength of light pass, defined as

$$n = A + \frac{B}{\lambda^2} + \frac{C}{\lambda^4}, \tag{2.1}$$

where n is the refractive index, λ is wavelength and A, B and C are coefficients related to the substance.[113] By fitting ellipsometry readings to this model, the thickness of the layer can be extracted.

2.2.4 Contact angle

Contact angle (θ in Fig. 2.6) measurements obtained using the static sessile drop method involves observing water (18 MΩ·cm) using a digital camera to find the contact angle of water dropped from a syringe against the surface in question. The images are analysed with a curve fitting model using the tangent approximation. For contact angle measurements in this thesis, a Theta optical tensiometer (Attension, Biolin Scientific, Espoo, Finland) was used.

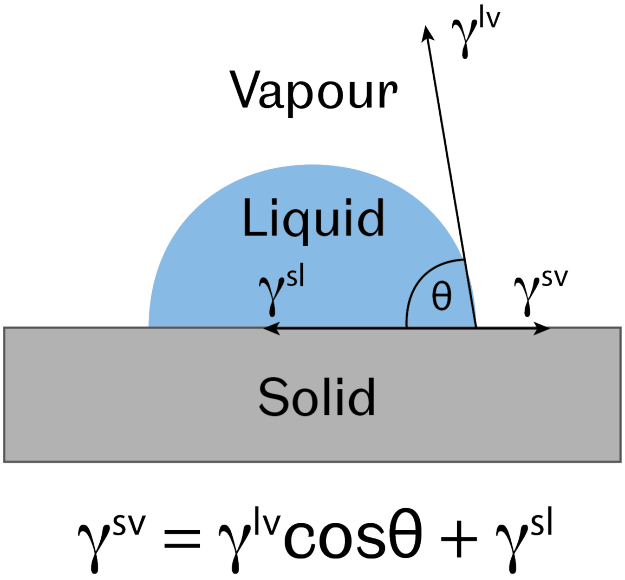

Figure 2.6: The Young's equation for calculating the solid-surface free energy (γ^{sv}) from contact angle (θ). γ^{lv} is the liquid-surface free energy. γ^{sl} is the solid-liquid interfacial free energy.

2.3 Enzyme preparations

All enzymes were used at their recommended commercial usage concentration of 0.2 mg/L of active protein in wash liquid and were supplied by Novozymes A/S (Bagsværd, Denmark). For the non-commercial DNaseI, a concentration was calculated where the effect of the enzyme on the measured biofilms was no longer dependant on the concentration.

This was found to be 2 mg/L. The commercial enzymes were tested at 2 mg/L and no increase was seen in their performance, confirming that the commercial usage concentration was already saturating the samples.

The enzymes were provided in liquid form with a given active protein concentration. As each enzyme had different active protein concentrations, a general dilution protocol was created that could be easily adjusted to each enzyme.

From the active protein concentrations, the volume of total enzyme that had

to be measured to obtain 2 mg of enzyme was calculated and is given in Table 2.4. Where the active protein concentration was provided as mg/g, it has been converted to mg/mL assuming a density of 1.09 g/mL of the enzyme solution.

Table 2.4: Active protein concentrations of various enzymes and the volume required to measure out 2 mg of active enzyme.

Enzyme	**Active protein concentration (mg/mL)**	**Volume containing 2 mg (μL)**
Cellulase 1	21.3	94
Cellulase 2	13.5	148
Protease	51.7	39
Mannanase	27.3	73
Amylase	14.5	138
DNaseI	24.0	83
S3 PDE	3.17	631

A 1000× stock solution is created by diluting 2 mg of active enzyme (Table 2.4) in 10 mL of imaging buffer (see Section 3.4). This stock solution is then further diluted to the correct working concentration by dissolving x μL of stock in x mL of fresh imaging buffer. For instance, to obtain 50 mL of enzyme in imaging buffer, 50 μL of stock solution would be used. As the performance of DNaseI was found to be constant at concentrations 10 times greater than the commercially available enzymes the final dilution step is reduced by a factor of 10. Therefore, to obtain 50 mL of DNaseI containing imagining buffer, 500 μL of stock solution is used.

A fresh 1000× stock solution was created for each day of experimentation and new dilutions made from the stock for each bioprobe. The stock solution is stored at 4 °C alongside the original solutions.

2.4 Measurement gathering and equipment

The measurements at the centre of attention for this thesis, the adhesion of biofilms in the presence of enzymes, were primarily taken using a atomic force microscope

(AFM) and a confocal laser scanning microscope (CLSM). This section sets out the general protocols for the use of these techniques and how they were specifically used to collect data the data presented in this project.

2.4.1 Confocoal laser scanning microscopy (CLSM)

Glass slides are used as substrates for confocal microscopy, following the protocols set out in Section 2.1.1. Once the biofilms have been established, the confocal specific preparation begins. The dilute growth media in each petri dish is removed and replaced by 15 mL of enzyme solution and left for 40 min. The slides are then washed with water to remove any remaining enzyme solution and then stained with LIVE/DEAD Bac*Light* according to Section 2.1.3. The slides are then washed in water twice to remove dye that has not been taken up by cells before being reimmersed in approximately 15 mL of water ahead of measurements.

Measurements were taken on a Leica (Wetzlar, Germany) SP-2 and SP-8 confocal laser scanning microscope. A 10× objective is used to locate suitably thick areas of biofilm on the slide, which is then introduced to an argon laser emitting at 488 nm and 561 nm for imaging. Images are 1162.5 µm^2 with a pixel size of 2.3 µm. Z-stacks are taken with the same x and y settings, with z images being taken every 7 µm. Photomultiplier tubes were limited to 497-540 nm for detecting SYTO 9 (green) and 571-638 nm for detecting propidium iodide (red).

Imaris (Bitplane, Oxford Instruments, Belfast, UK) software was used to quantify the biovolumes changes of the confocal images.

2.4.2 Atomic Force Microscopy (AFM)

All AFM measurements were made using an Asylum Research (Oxford Instruments, Abingdon, UK) MFP-3D microscope. Force measurements of bacterial bioprobes of NPO-10 tipless cantilevers using the D arm, which has a nominal spring constant of

60 pN/nm. Spring constants were confirmed to be within manufacturer's tolerances using the thermal tune method.[66]

Force maps for *M. luteus* against PET substrates consisted of 100 points in a 10×10 1 µm map to keep the cantilever in the same area of the substrate. Trigger points and force distances may be altered for specific bioprobes if the initial data capture indicated that a probe may have events at longer extensions than usual, but the default settings were a trigger point of 20 nN, a force distance of 4 µm with a velocity of 2 µm s^{-1} in closed loop mode. If a bioprobe did use different settings, these were kept consistent for all measurements using that probe so that the percentage difference would not be adversely altered.

A 10×10 force map is first taken without dwell at the surface and then repeated with a 10 second hold in contact with the surface, which is the maximum the software allows. The control domestic water supply is replaced with the enzyme solution to be tested and allowed to incubate for 40 min. The two force maps are then repeated and the bioprobe and PET subsrate are discarded for new samples. Due to the incubation times and extended measurement time involved in 100 dwelled measurements, typically three bioprobes would be tested in a normal working day.

The microscope control software, an Asylum Research add on for Igor PRO (WaveMetrics Inc., Portland, USA) was also used for initial data analysis and is able to export the readings in .csv format, to be imported into MATLAB (MathWorks Inc., Massachusetts, USA) where custom software has been written to analyse changes in force and extension much more rapidly than is possible in the native software.

2.4.3 Summary

The details listed in this chapter are the final methodologies used throughout the following chapters for preparation and experiments. Chapter 3 covers the the mod-

ifications and refinements carried out in terms of thin film production and bioprobe construction, alongside the results obtained using these methods.

As the experiments of Chapter 4 were carried out in an industrial setting, there is little cross over with the methods used throughout the rest of the thesis. Methodologies specific to that work are contained within that chapter. Chapter 5 returns to using the methods laid out in this chapter, with biologically modified AFM cantilevers and the resulting analysis required to extract that form of data.

Chapter 3

Bioprobes and enzymes

The central aim of this project was to investigate the adhesion of biofilms on textile substrates, using AFM. This rather concise statement had many hurdles and issues that needed to be overcome before data collection was able to progress at a satisfactory pace. The methodology for constructing bacterial bioprobes on tipless cantilevers was inspired by Xu *et al.*,[23] from their work with *Escherichia coli* (*E. coli*) against different chemically defined surfaces. This project differed by keeping the substrate, a poly(ethylene terephthalate) (PET) thin film that was designed to mimic polyester fibre's chemistry and adhesion, constant and varying the medium in which the substrate and bioprobe were incubated.

Although the methodology settled on biofilms on tipless cantilevers, alternatives of single cell force spectroscopy (SCFS) and construction of colloidal probes were also attempted and investigated. Bioprobe experiments were only conducted on PET substrates as a textile analogue in this project, but thin films of cellulose (to represent cotton) and nylon were also developed.

3.1 Textile substrates

The substrate of interest for this project are textiles, but fabric pieces are difficult to use inside an AFM. Overhanging threads pose a hazard to the fragile cantilever tip as it is guided to the surface. With careful manoeuvring of the cantilever, the surface of the textile can be reached. The fibres are many microns in diameter and rise above the plane of the fabric by a number of microns. Although this area can be imaged clearly, taking force measurements in this region would be difficult due to the topography. Polyester fabric is poly(ethylene terephthalate) (PET) and cotton is comprised of cellulose. Both chemicals are well studied and there are known protocols for creating thin films of them. Thin films lack the dangers to the cantilever found on fabric pieces, with no overhanging threads or rough surfaces to contend with. They are an ideal substitute for the fabric pieces, providing their shared chemistry results in similar adhesive interactions.

Glasswear and substrates must be clean to obtain good quality thin films. Glassware was cleaned using the RCA organic cleaning method. The items were boiled in a solution of five parts deionised water, one part aqueous ammonium hydroxide and one part aqueous hydrogen peroxide for 15 min. The solution was allowed to cool and the glassware was then rinsed thoroughly with deionised water and acetone before being dried with nitrogen.

Silicon substrates were cleaned using piranha solution. This is a highly corrosive and oxidising solution and must be prepared with care and in minimal amounts. It is made by slowly adding 30% hydrogen peroxide to 70% sulfuric acid. Silicon wafers are submerged in the piranha solution for 1 h. The wafers are then rinsed with deionised water, acetone and dried in nitrogen before being stored in a sealed Petri dish. Before spin coating, the wafers were again cleaned using a 15 min UV/ozone treatment.

3.1.1 Poly(ethyleneterephthalate) (PET) thin films

Initially, a method for preparing PET thin films from a 4% solution in *o*-chlorophenol was followed, involving stirring the solution with heating for 48 h.[114] This concentration was found to be too high as the solution became saturated. The concentration was lowered to 0.2% PET and left to dissolve. At this much lower concentration, the PET still appeared to not be fully dissolving in the solution as particles were visible in the solution. This solution was spin cast onto silicon wafer at a speed of 2000 rpm with an acceleration of 2500 rpm/s. The samples were annealed in a vacuum oven overnight at 20 °C to remove any remaining solvent. The PET films prepared using this method produced uneven surfaces, with nanometre sized features, as shown in Fig. 3.1.

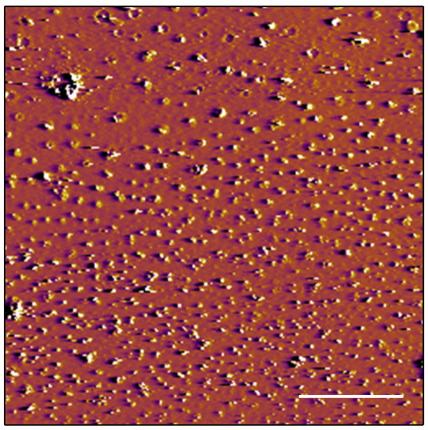

Figure 3.1: PET thin film prepared from a 0.2% *o*-chlorophenol solution. The scale bar is 500 nm.

Due to these poor PET thin films, an alternative method was found that uses hexafluoroisopropanol (HFIP) as the primary solvent.[106] This method used 0.16% (w/w) solutions of PET in HFIP which was allowed to dissolve with stirring under low heat overnight. An infrared lamp is used to pre-heat the silicon wafer (at least 10 s of irradiation) before spin casting the solution at 3000 rpm for 20 s. The wafer should then be annealed at 80 °C for 2 h to remove the residual solvent. The thin

films produced by this method were also unsatisfactory, with the PET appearing unable to properly dissolve into solution.

It was at this point it was realised the PET supplied by Sigma-Aldrich (now part of Merck) contains 30% glass particles as a reinforcing agent. Older PET pellets from ICI (now defunct) were obtained from collaborators in the department that did not contain glass reinforcement. At the point this new source of PET was obtained, further alterations to the method had been planned after consulting a thesis on PET thin film preparation.[110]

This new method used a combination of the two solvents mentioned previously and claimed to produce reliable thin films. A 3% (w/w) stock solution of PET in HFIP was created by heating in a sealed vial. This stock solution could be diluted with *o*-chlorophenol to obtain different film thicknesses. Ibaragi[110] used *o*-chlorophenol to dilute the stock solution, rather than additional HFIP, as the *o*-chlorophenol increases the boiling point of the solution, allowing more time for the thin film to form and giving rise to smoother samples (HFIP bp = 58.2 °C, *o*-chlorophenol bp = 174.9 °C). The films must be annealed at 200 °C or hemispherical features cover the surface, as seen in Fig. 2.3. Thin films using this technique would sometimes appear to have areas on the wafer where the solution had dewetted from the surface. Removing the cleaning steps of the wafer vastly improved the success rate of PET thin films. This is due to the oxidation of the silicon surface by the cleaning steps making an unsuitable substrate for the hydrophobic solution.

PET thin films were measured in air and under water using an ellipsometer. The thickness values calculated in air are shown in Table 3.1 and shows the targeted thickness of 40 nm has been achieved, with measured values indicating the thickness of the samples to be 40.5 ± 0.1 nm.

Ellipsometry measurements were also conducted under water and the thickness fitted using the effective medium approximation method. This method is used for

Sample	Thickness (nm)
1	38.8 ± 0.1
2	40.2 ± 0.1
3	42.6 ± 0.4
4	40.3 ± 0.1

Table 3.1: Thicknesses of PET thin films as measured by ellipsometry in air.

composite materials, where the model treats the different parts as a single layer. In this case, the model incorporates a changing amount of water into the PET layer which it uses to detect the swelling of the layer. The change in thickness was measured over five hours, in which an increase of over 14 nm was observed. The change in thickness with respect to time can be seen in Fig. 3.2, with a rapid change in thickness over the initial 30 min before the rate of expansion slows.

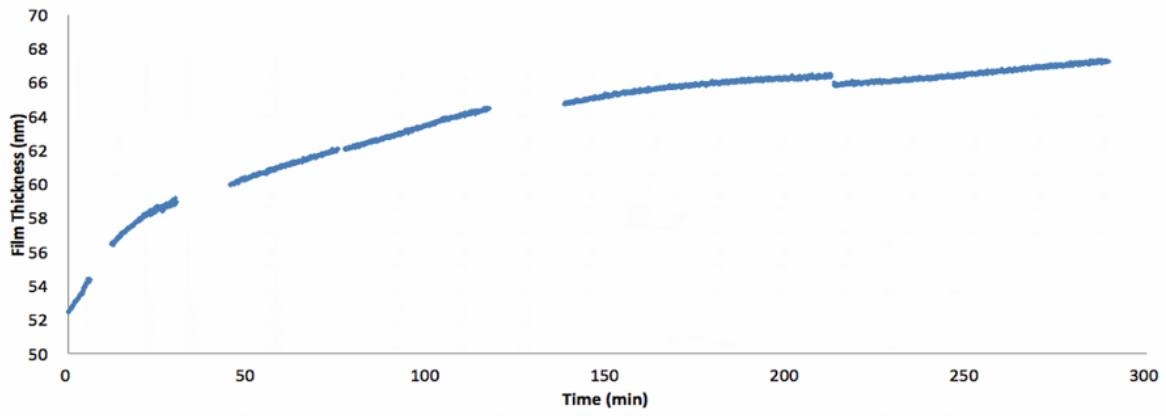

Figure 3.2: PET thickness increasing under water over a 5 h time period.

3.1.2 Cellulose thin films

Unlike the varying methods for creating a PET thin film, the literature for the creation of cellulose thin films is unified with a method using *N*-methylmorpholine *N*-oxide (NMMO) as the primary solvent being followed.[106] An initial layer of poly(vinyl amine) (PVAm) is required as to anchor the cellulose thin films to the silicon wafer. A 0.01 g/L solution of PVAm in deionised (DI) water was created and cleaned silicon wafers immersed in the solution for 20 min. These wafers were then

rinsed gently in fresh deionised water and dried at 50 °C for 45 minutes and then kept under vacuum.

Cellulose (0.01 g) is dissolved in 10 g of 50% NMMO in water, by heating to 115 °C. The solution must be removed from heat as soon as the dissolution is complete, or a brown water soluble precipitate forms. Allowing the temperature of the solution to exceed 130 °C will also cause the cellulose to degrade. Some methods suggest dissolution requires 1 h,[111] but the solutions tested here would always show precipitate if left heating for that amount of time. Once the cellulose is fully dissolved, 9.99 g of dimethylsulfoxide (DMSO) is added dropwise to the solution and stirred for a further 10 min. The DMSO helps adjust the target thickness and helps achieve a viscosity more appropriate for spin coating. The solution is spin cast at 2500 rpm for 30 s. The wafers are then immersed in DI water for four hours with frequent water changes, to allow the cellulose layer to precipitate onto the PVAm layer. After the water changes are complete, the wafers are dried with nitrogen and stored in a desiccator.

Ellipsometry

Ellipsometry measurements were conducted on these thin films to understand the size of the PVAm and cellulose layers. Fresh wafers with only the PVAm steps complete were also tested so that the anchor layer could be properly accounted for in the model. The PVAm layer is thin, with ellipsometry in air of three different parts of the film giving a value of 0.92 ± 0.01 nm. By adding this value for the PVAm layer into the model, with a refractive index of 1.58 and a refractive index of 1.54 for the cellulose layer, the values for the thickness of the cellulose layer are given in Table 3.2.

The similar optical properties of the PVAm and cellulose layers were deemed to be disrupting the model's ability to detect the boundary layer between the two polymers. The software has the ability to combine these layers into an effective medium approximation (EMA). Once this option was enabled, the combined PVAm

Sample	**Location**	Cellulose Thickness (nm)
A	1	1.0 ± 0.2
	2	0.74 ± 0.1
	3	1.9 ± 0.9
B	1	5.2 ± 0.9
	2	7.7 ± 0.8
	3	1.9 ± 0.3

Table 3.2: Ellipsometry measurements acquired in air on two cellulose films, three points per sample. The effective medium approximation is processing the PVAm and cellulose layers as distinguishable layers.

and cellulose layer was found to be 76 ± 1 nm.

Contact angle

Contact angle measurements were collected according to the method described in Section 2.2.4. Water contact angles were obtained for silicon, PVAm and three samples of cellulose thin films over short periods of time (100 images every 16 ms over a total of 1.6 s). The values are displayed in Table 3.3.

Sample	**Contact Angle (average)**
Silicon	20.4°
PVAm	69.2°
Cellulose 1	45.5°
Cellulose 2	46.6°
Cellulose 3	36.8°

Table 3.3: Static sessile drop method water contact angle measurements for all steps of the cellulose thin film preparation method.

The contact angle measurements show that the different coating steps have been successful at modifying the surface properties. Clean silicon wafer has been modified by the submerging period in PVAm and made the surface more hydrophobic (all readings are hydrophilic in nature as the contact angle is less than 90°). This large change is expected as the literature describes PVAm as an anchoring layer.[106] This more hydrophobic surface aids in the initial deposition of the cellulose thin film. The readings for the cellulose film contact angle show it is more hydrophilic than

the PVAm layer, but still has a greater angle than the native silicon layer.

3.1.3 Validity of thin film analogues

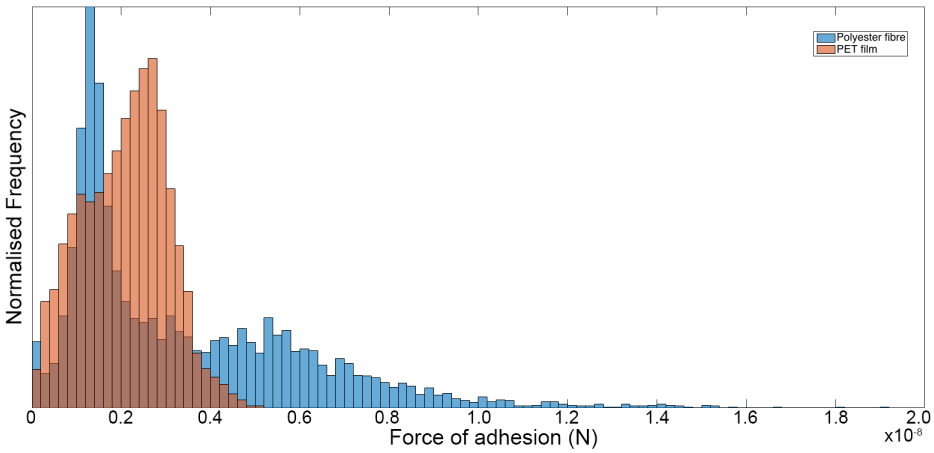

Figure 3.3: Force of adhesion interactions between an MLCT cantilever tip and poly(ethylene terephthalate) (PET) based substrates. The histograms are normalised to each other and overlayed to allow for straightforward comparison.

Thin films of PET and cellulose were prepared according to the previous sections and probed using an MLCT silicon nitride cantilever to establish their average adhesion values. The same tests were carried out on fabric samples of polyester and cotton to compare against the thin films. As can be seen in both Fig. 3.3 and 3.4 the thin films have similar peak force as the fabric, but also lack the regions of higher adhesion values seen in the natural fabrics. For both PET and cellulose substrates, the fibre and film differ in mean adhesion by only 0.1 nN. This close grouping of adhesion responses is of benefit when comparing the effect of enzymes and other treatments, as any change in measured adhesion force is less likely to be due to the variation in the substrate. These properties make the thin films valid substitutes for the problematic fabric samples.

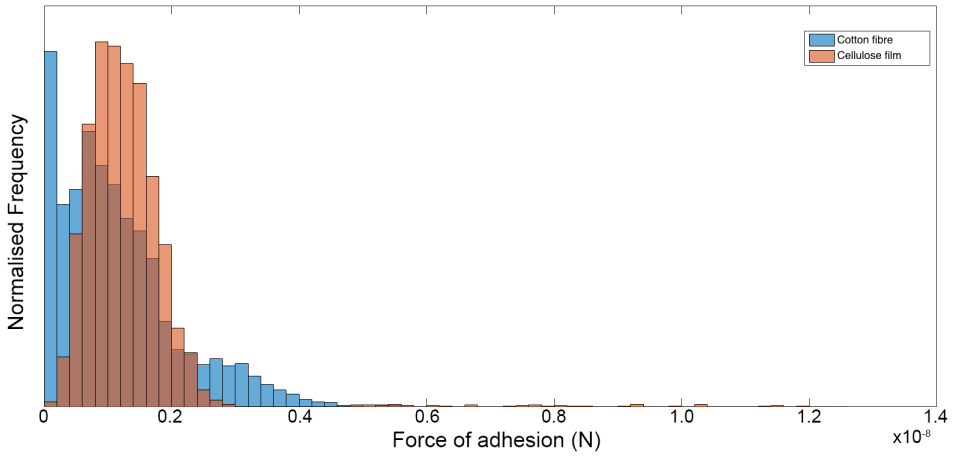

Figure 3.4: Force of adhesion interactions between an MLCT cantilever tip and cellulose based substrates. The histograms are normalised each other and overlayed to allow for straightforward comparison.

3.1.4 Testing storage of thin film solutions

The solutions prepared for these thin films use dilute solution of polymer. Due to the sensitivity of the target film thickness to concentrations of polymer in these solutions, it is difficult to scale down the masses and volumes without the error in the measurements becoming more prominent. This results in large volumes of solution being prepared, when only a small volume is required to spin cast numerous samples.

If the remaining solution is disposed of, it is not only a waste of resources, but necessitates repeating high temperature preparation with a number of highly hazardous solvents. If the remaining solution can be stored to be used at a later date, this has positive outcomes for the environment and health and safety concerns. The films produced by solutions that have been stored for a period of time need to match those produced initially by the prepared solution. To investigate the storage capabilities of the PET and cellulose solutions, films were made immediately after solution preparation and again after a month of solution storage.

PET

PET thin films spin cast from a solution prepared three months prior showed no effects of degradation. Freshly spun thin films (Section 3.1.1) recorded an average thickness of 40.5 $\pm$ 0.1 nm.

The same solution three months later produced an average thickness of 43.6 $\pm$ 0.1 nm. This small increase in thickness is likely due to a small amount of evaporation of solvent increasing the concentration of PET.

Cellulose

Ellipsometry measurements using the effective medium approximation method found fresh cellulose films prepared from the solution outlined in Section 3.1.2, to have a thickness of 76 $\pm$ 1 nm. The same measurements on films cast from a month old

solution indicated a thickness of only 29.2 ± 0.3 nm. This decrease in thickness suggests that the cellulose in solution is degrading over time and effectively decreasing the concentration of the solution.

Ellipsometry measurements taken over a period of 30 minutes under water on both old and new cellulose films indicate that they both gain only 1% thickness due to water swelling, indicating that although the thickness of the produced film is lower, the properties of the film are still similar. To further examine these properties, AFM adhesion measurements were taken of the two films.

Force maps of 100 points each were taken over 1 μm^2 areas of the old and new thin films and compared and are shown in Fig. 3.5. The adhesion readings of the month old solution have a wider variation than those produced by the fresh solution. Imaging the surfaces using AFM also showed particulate matter on the surfaces of the films cast from the old solution. As the decrease in thickness suggests that cellulose has decomposed and precipitated out of solution, the particles covering the surface are very likely to be these byproducts of prolonged storage in solution.

These results indicate that cellulose dissolved in its NMMO-DMSO solution is not capable of remaining entirely stable over the period of a month and should not be used to spin cast at a later date. Cellulose films should be spin cast in bulk when the solution is first prepared and the films stored in a desiccator until needed.

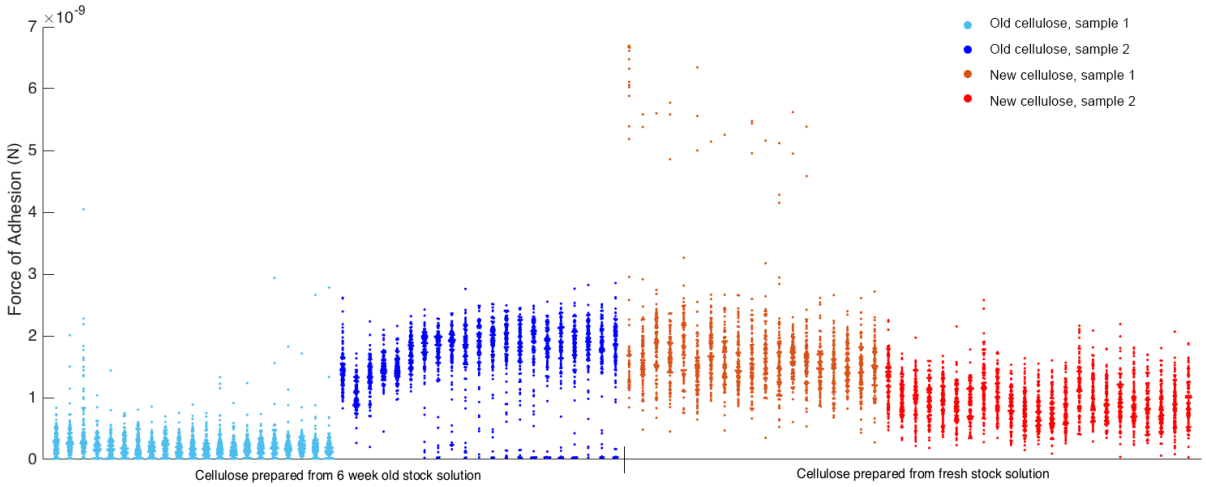

Figure 3.5: Force of adhesion interactions between an MLCT cantilever tip and cellulose based substrates. Old cellulose samples are spin cast from a one month old solution. New cellulose samples were spin cast immediately. Each force map is comprised of 100 interactions.

3.2 Bacteria

Bioprobes were trialed and investigated using both gram-positive and gram-negative bacteria. *Pseudomonas* sp. Pse1 was chosen as the gram-positive bacterium. This strain was isolated from a phenol contaminated aquifer in the West Midlands, UK and has been used for previous work within the research group and its collaborators.[60,115,116] *Micrococcus luteus* (ATCC 4698), sourced originally from the American Type Culture Collection, was selected as the gram-negative bacterium due to the reasons outlined in Section 1.1, as well as interest from industrial partners.

3.3 Bioprobe alternatives

There are many alternatives for constructing bioprobes to be used with AFM, including multiple single cell alternatives or constructing entire biofilms on the cantilever tip. Each method has its advantages and disadvantages which become more or less important depending on what is to be investigated. Traditionally the single cell approach has dominated research.

The most basic form of single cell force spectroscopy (SCFS) involves attaching an individual cell to the end of a cantilever tip, usually with the aid of a bioadhesive such as poly-L-lysine. Cells are allowed to settle on a substrate before a functionalised cantilever is brought over the top of a chosen cell. The tip is carefully lowered into place on top of the cell for such time that the cantilever can be retracted, taking the cell with it. This is then used in force measurements against the new substrate of interest. The trade-off with being the most simple technique is that replicating the exact positioning of the bacteria on the cantilever is not guaranteed, which can cause issues with data replication.[78]

3.3.1 Single Cell Force Spectroscopy (SCFS)

There are a range of different bioadhesives that are used for the preparation of single cell probes, including Cell-Tak, poly(dopamine) and poly(lysine). Cell-Tak and poly(dopamine) were trialed in these experiments.

Cell-Tak

Sodium bicarbonate (57 μL, 0.1 M) was mixed in a clean Eppendorf tube with 1 μL of NaOH and 2 μL of Cell-Tak solution. The cantilever to be coated is incubated in this mixture for 20 minutes, before being gently washed with deionised (DI) water.

Poly(dopamine)

A 4 mg/mL dopamine hydrochloride solution is prepared in 10 mM TRIS buffer. The cantilever to be coated is incubated in this solution for 1 h. During this time, the colourless solution will turn slightly yellow due to the oxidative polymerisation process that forms the poly(dopamine) on the surface.[117] The cantilever is gently rinsed with DI water and allowed to dry at 20 °C in a vacuum oven.

Bacterial probe assembly

A glass-bottomed Petri dish was cleaned inside a UV-ozone chamber, which increases the hydrophilicity of the glass. A dilute bacterial cell suspension was stained with BacLight (see Section 2.1.3) and incubated for 10 minutes away from light. The stained cells were added to the Petri dish and moved onto the stage of the AFM, along with the adhesive covered cantilever. Isolated cells were located using the inverted microscope attached to the AFM. A suitable cell will be immobile on the surface of the Petri dish (not floating in solution) and not immediately surrounded by other cells. Fig. 3.6 shows the size of the cantilevers compared to a bacterial suspension on the Petri dish bottom. The area on the left of this view of the suspension is too dense to attach just a single cell on the end of the cantilever, but there are potential candidates on the right side of the image.

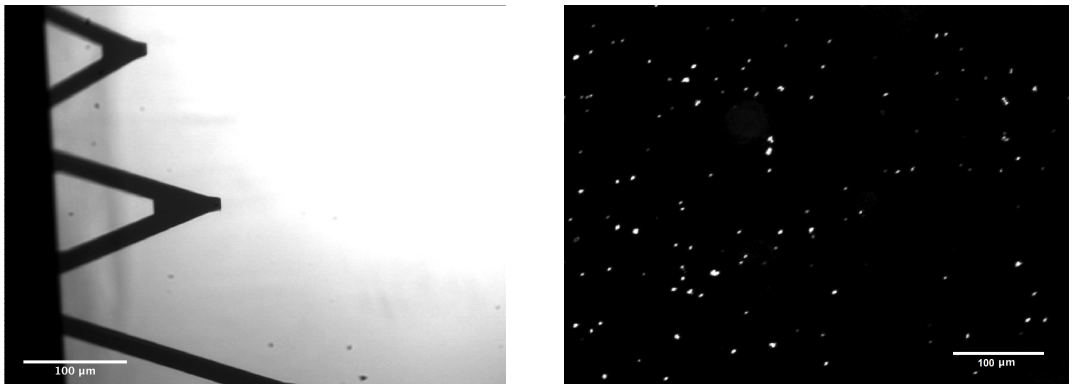

(a) MLCT-O10 tipless cantilever (b) *M. luteus* dilute suspension

Figure 3.6: 10× objective images taken using inverted microscope in the AFM. The black marks in (a) are not bacteria, but imperfections on the lens. The cantilever is hovering above the dish bottom, which is the point at which the scale bar becomes accurate. The fluorescence filter is engaged for (b).

Once an appropriate cell has been identified, the cantilever arm is lowered over the chosen bacterium and contact is made. The contact is maintained for 5 min and then the cantilever is retracted. By maintaining the focus on the Petri dish bottom, the stained cell should be seen to leave the field of view as the cantilever is retracted. The cantilever tip can also been observed with the 40× objective in

bright field mode to identify if the bacterium has been bound. If attachment has been successful, the probe can be carefully removed from the suspension and the Petri dish replaced with the surface of interest to be probed. For these initial trials, a clear part of glass was found and the single cell probe measured against this area.

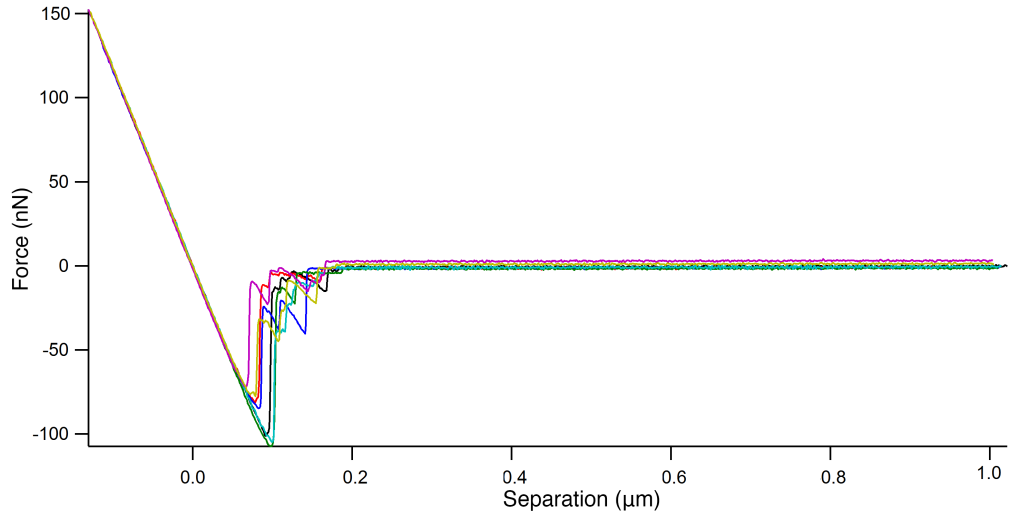

Figure 3.7: A random selection of seven interactions of a single *M. luteus* cell attached to a cantilever tip using Cell-Tak, probed against a glass surface.

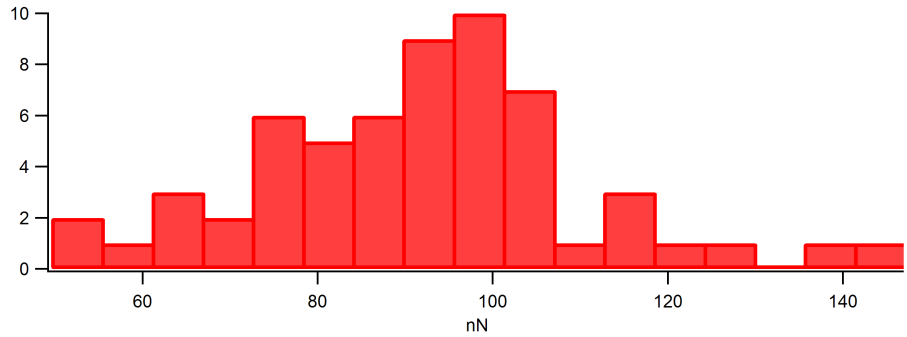

Figure 3.8: A histogram of the maximum adhesion of each interaction of a single *M. luteus* cell attached to a cantilever tip using Cell-Tak, probed against a glass surface.

A single *M. luteus* cell was attached to a tipless MLCT-O10 cantilever arm with a nominal spring constant of 30 pN/nm. Fig. 3.7 and 3.8 show that the cell was successfully attached to the tip with detailed retraction curves evident. The average force measured between the cell and the glass substrate was 91.3 $\pm$ 2.4 nN.

Alternative cantilevers and bacteria were also tested with this method to explore if it is applicable to a range of experimental conditions. NPO-10 cantilevers were used with *Pseudomonas* sp. Pse1 cells, using poly(dopamine) as the adhesive. With this cantilever, an arm with a nominal spring constant of 60 pN/nm was chosen and functionalised in the same manner as before. The average interaction between *Pseudomonas* and glass on this stiff cantilever was 30 ± 3 nN and can be seen in Fig 3.9 and 3.10. As the bacteria are different the measured forces cannot be compared with each other. However, the initial attachment of the cell to the cantilever tip was successful after fewer attempts with this cantilever, which is likely to be due to a greater contact being achieved with the stiffer nature of the cantilever.

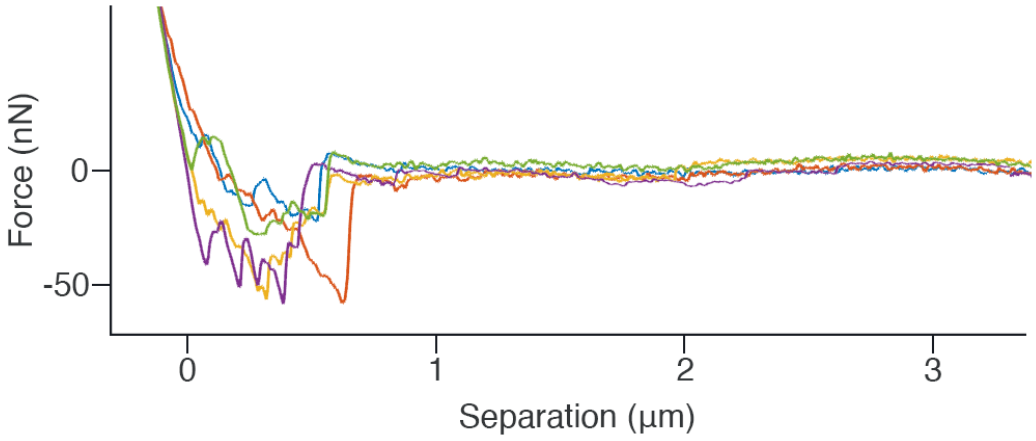

Figure 3.9: A random selection of five interactions of a single *Pseudomonas* Pse1 cell attached to a cantilever tip using poly(dopamine), probed against a glass surface. Only retraction curves are shown

While the method of attaching a bacterium directly to the cantilever tip has been shown to have successes, it is difficult to reliably attach the cell in the same place on the tip. One of the main advantages of this SCFS method is the ability to compare data between different experiments when all other variables are kept constant. If the amount of contact the cell makes with the substrate cannot be guaranteed to be constant across these experiments, this method is no longer appropriate.

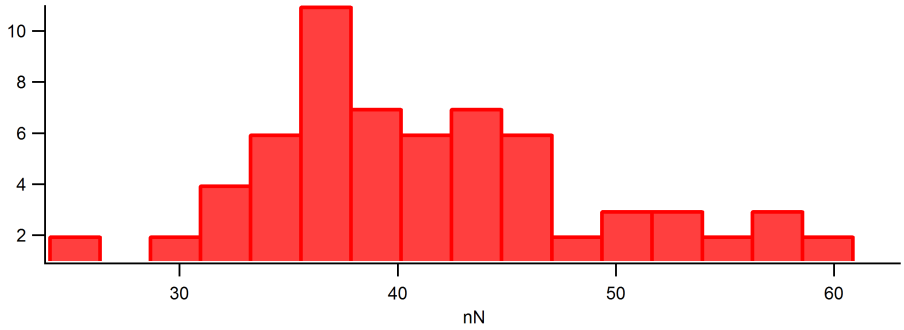

Figure 3.10: A histogram of the maximum adhesion of each interaction of a single *Pseudomonas* Pse1 cell attached to a cantilever tip using poly(dopamine), probed against a glass surface.

3.3.2 Colloidal SCFS

In an attempt to further improve this SCFS technique, Beaussart *et al.*[118] modified the protocol to add a colloidal bead to the cantilever tip before picking up the individual cell. The reasoning for adding the preparation step is that the large, well-defined geometry of the colloidal sphere (approximately 6 µm in diameter) allows the placement of the cell in the centre of the colloid, giving more reliable and reproducible single-cell force measurements.

The cantilever to be functionalised is mounted in the AFM and a drop of UV-curable glue placed on a glass slide on the AFM stage. Just the end of the tip of the cantilever is moved into the glue and then retracted. The glass slide is removed for one that has micron sized dry polystyrene colloidal spheres on the surface. The glue covered cantilever tip is positioned over a sphere and contact is made for a few seconds. The cantilever is then removed from the AFM and the glue is cured under UV light for 10 minutes. The cantilever with the colloidal sphere is then covered in bioadhesive as detailed in previous sections. Fig. 3.11 shows a constructed colloidal probe before a cell has been attached.

This method was tested with *Bacillus subtilis* (*B. subtilis*) cells as the SCFS method to attach the bacterium directly to the cantilever tip had been unsuccessful. Using the colloidal probe method, a *B. subtilis* cell was succesfully attached to the probe and measured against a clean section of glass. The force-distance curves are shown in Fig. 3.12 and the distribution of forces in Fig. 3.13. The curves are all of a similar shape which is an encouraging sign that the cell is making a repeatable contact with the surface. There are two regions of repulsion observable in the approach curve, which which maybe explained by the cell being compressed as the contact between tip and substrate begins.

Although the data collected with colloidal probes appear to be clear and repeatable, the additional steps of coating the cantilever with glue, attaching the colloidal

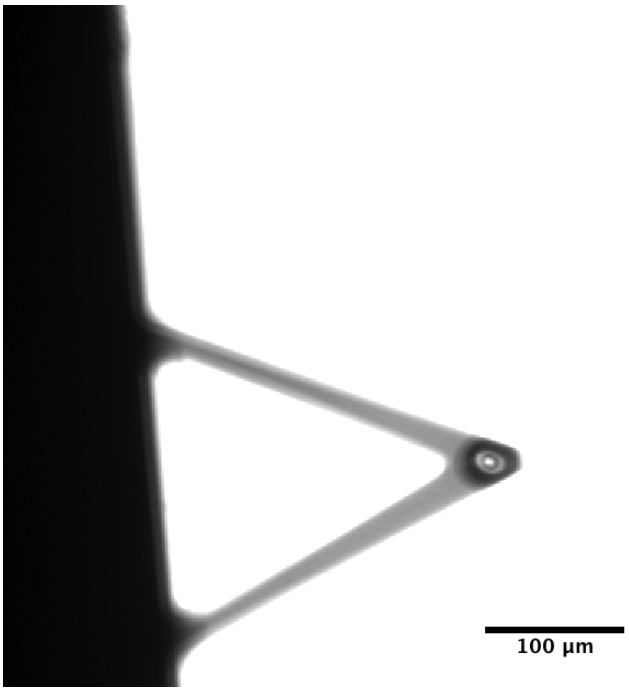

Figure 3.11: Tipless NPO-10 cantilever with a polystyrene colloidal sphere (10 µm) attached.

sphere, coating the sphere with bioadhesive and finally collecting the cell certainly slows the maximum rate of data collection. This method also has an increased risk of damaging the cantilever with every handling step. Colloidal probes may well be the ideal technique for reproducible data in SCFS, but for some investigations, a single cell is not appropriate.

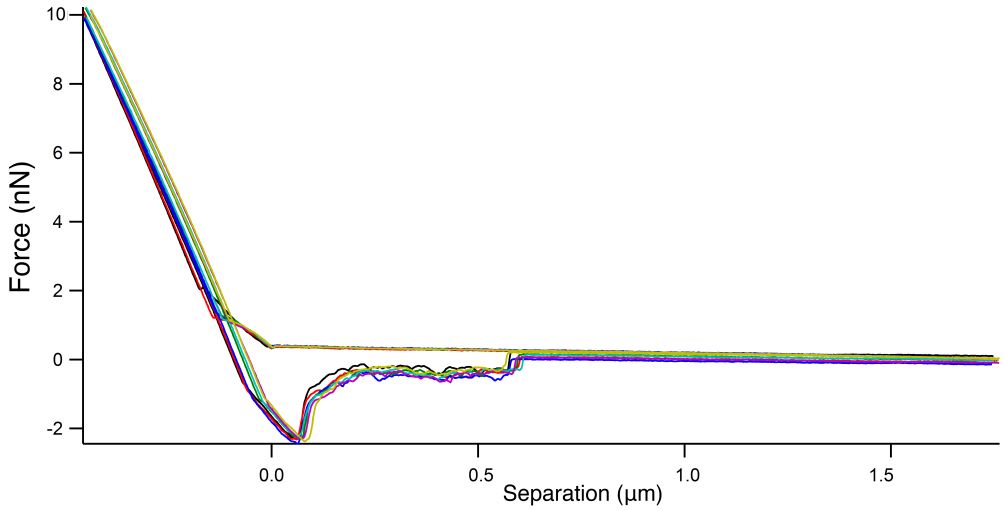

Figure 3.12: A random selection of seven interactions of a single *B. subtilis* cell attached to a cantilever tip using poly(dopamine) and a colloidal sphere, probed against a glass surface.

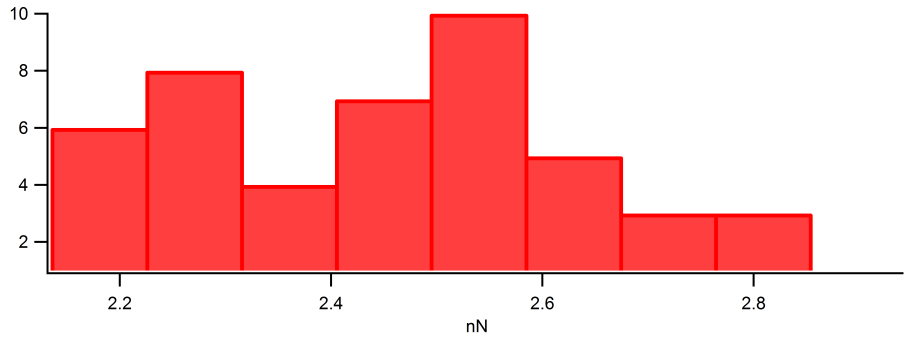

Figure 3.13: A histogram of the maximum adhesion of each interaction of a single *B. subtilis* cell attached to a cantilever tip using poly(dopamine) and a colloidal sphere, probed against a glass surface.

3.3.3 Biofilm cantilever

It is known that bacteria in the planktonic state or in a biofilm behave differently and express different chemistry.[25,36] Therefore, it follows that a single cell can only give information about adhesion of planktonic cells, not those already in an established biofilm. The protective extracellular polymeric substances (EPS) of a biofilm dramatically alters how bacteria would interact with surfaces or respond to a threat such as enzymes or antibacterial agents.[83,119] To study biofilms and their response to these scenarios, SCFS is not valid and a biofilm alternative should be used instead.

Xu *et al.*[23] demonstrated a straightforward method for preparing biofilms on multiple tipless cantilevers at one time, as detailed in Section 2.1.2. The method of establishing biofilms on the tip may be straight forward compared to SCFS techniques but carries the disadvantage of not knowing how many bacteria are making contact with the substrate during force measurements. This means that values of adhesion cannot be compared across different bioprobes, merely the trend in the change of adhesion when a treatment is applied. Despite this, the rate at which biofilm probes can be tested allows reasonable data sets to be collected quickly to aid in identifying these trends.

The method was tested on a silicon wafer stained with BacLight dye to investigate the quantity and quality of biofilm that can establish on a poly-L-lysine coated surface in approximately 24 h. A *Pseudomonas* Pse1 culture was used to inoculate a 1×1 cm silicon wafer and was imaged using an Olympus BX-51 fluorescence microscope, which is shown in Fig 3.14. The biofilm has clearly established successfully on the silicon wafer substrate, although there are patches without bacterial coverage. If this part coincides with the region of the cantilever tip that makes contact during AFM measurements, it would not be a valid representation of how the biofilm will interact. Following this successful test, the method was conducted on a silicon nitride tipless cantilever and imaged after treatment with protease enzyme, as shown in Fig. 3.15.

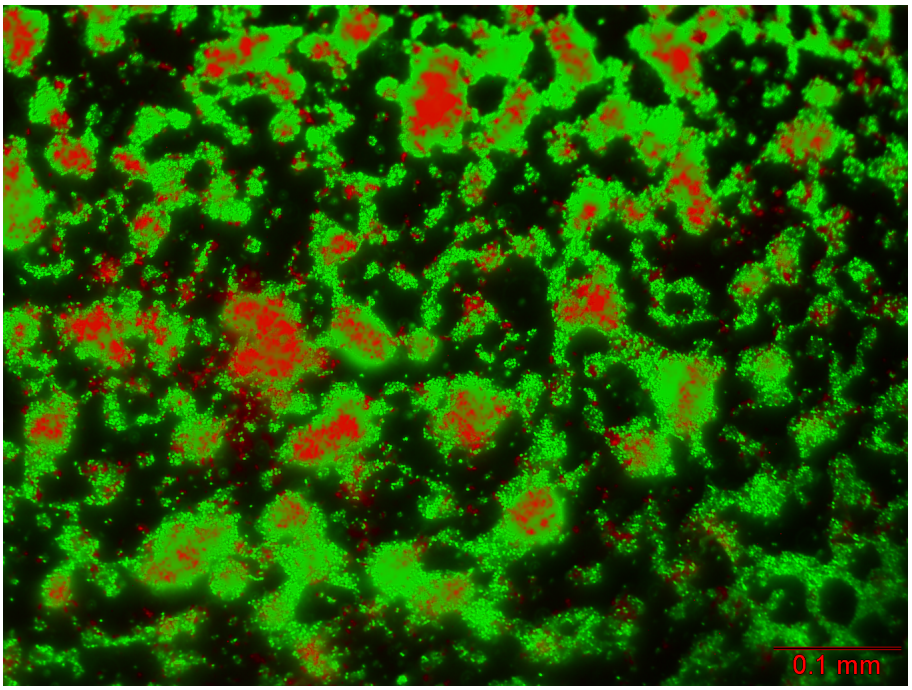

Figure 3.14: *Pseudomonas* biofilm grown on a poly-L-lysine coated silicon wafer, stained with BacLight viability kit. Green (live) and red (dead) channels have been superimposed.

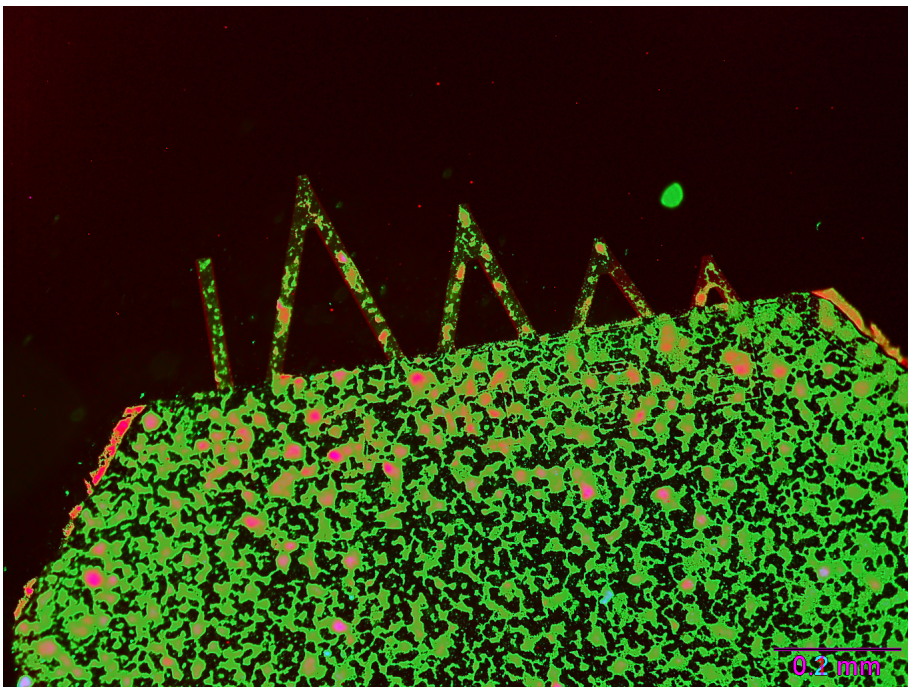

Figure 3.15: *Pseudomonas* biofilm grown on a poly-L-lysine coated MLCT-O10 cantilever, stained with BacLight viability kit. Green (live) and red (dead) channels have been superimposed. Imaged after treatment with protease enzyme.

Dwell time at surface

Xu *et al.*[23] introduce a dwell at contact between their biofilm cantilever and substrate in their findings. This is not a technique that had appeared in other literature regarding SCFS techniques, so was explored using a *Pseudomonas* biofilm cantilever against a cellulose thin film. Fig 3.16 shows the interactions of two separate biofilm cantilevers prepared on the same day under the same conditions.

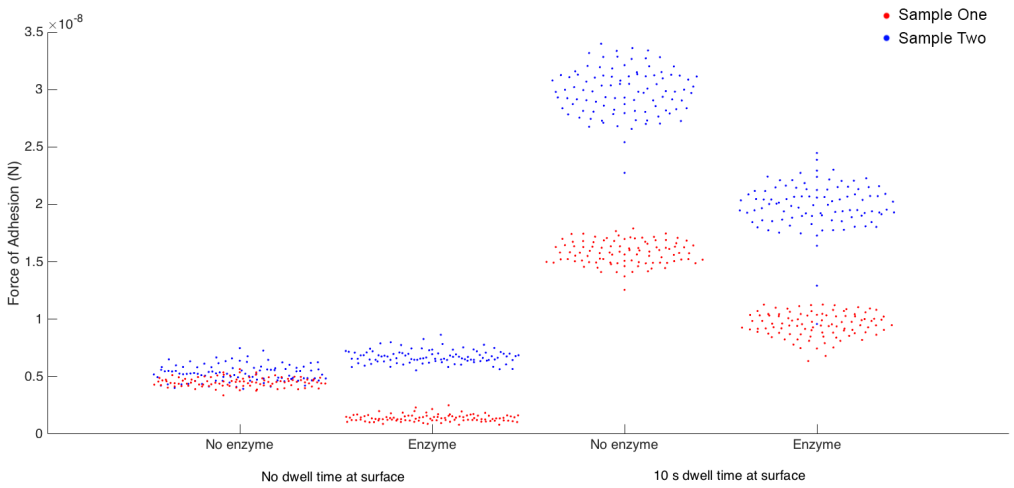

Figure 3.16: Bee swarm plot showing adhesion values between a *Pseudomonas* biofilm cantilever and a cellulose thin film. There are two experimental conditions: with and without protease enzyme and with and without a dwell at the surface of 10 s.

An immediate observation is that the data from the dwelled measurements feature similar trends across the two samples and at greater forces than the non-dwelled measurements. This observation is likely to be due to additional time allowing the bonds between the biofilm and the substrate to fully form, compared to the instantaneous contact in the non-dwelled measurements. Maximising the forces observed before any treatment will also be of benefit when exploring the effect of different treatments as it gives a higher resolution for minor changes in adhesion to be detected. For these reasons, only data from dwelled interactions will be analysed when investigating the effect of different treatments on biofilm adhesion to different substrates. The non-dwelled interactions were maintained in the protocol of experiments as the short run time (approximately 2 min for a 10×10 force map) acts as a

quality control check, confirming the presence of a viable biofilm on the cantilever before the more time consuming (approximately 24 min) dwelled force map is collected.

Despite the very different initial adhesion values of the two samples in Fig. 3.16, they both indicate the biofilm was affected in similar amounts by the enzyme treatment, with each sample showing a decrease in adhesion of approximately 50% after treatment. This confirms the expected disadvantage of biofilm cantilevers, that cantilevers prepared in identical conditions at the same time will have different shaped biofilms established at the tip. This disadvantage is overcome by the agreement in the response from the cantilevers, the use of bacteria in the biofilm state and the speed at which many can be constructed and tested compared to SCFS techniques.

Poly-L-lysine weights

Poly-L-lysine (PLL) is predominantly available in two molecular weights in the UK, a 1000–5000 $gmol^{-1}$ variant (Sigma Aldrich, P0879) and 30000–70000 $gmol^{-1}$ (Sigma Aldrich, P2636). Bioprobes were constructed using both molecular weight variants and probed against a PET thin film. The lower molecular weight PLL resulted in a much higher failure rate than the higher molecular weight, which is observed as the characteristic force-distance curve of PLL interacting with PET, similar to that observed in Fig. 3.22. This indicates that the lower molecular weight PLL does not encourage the formation of biofilms as well as the higher molecular weight. Due to this observation, only 30000–70000 $gmol^{-1}$ molecular weight PLL will be used for bioprobe construction.

3.4 Control buffer

Enzymes were provided by Novozymes A/S (Bagsværd, Denmark) in high concentration solutions. In real world applications they are used at very small quantities in the bulk liquid, typically only 0.2 mg of active protein per litre of water. To clearly

understand what effect the enzymes were having on the biofilms in experiments, the solution used to dilute the enzymes would have to have minimal effect on the bacteria and be consistent in terms of properties such as pH and ionic concentration. Lau *et al.*[120] conducted a range of experiments with biofilm measurements in an AFM using deionised water, so this was used as an initial condition. A *Micrococcus luteus* (*M. luteus*) biofilm cantilever was probed against a PET thin film before and after a 40 min incubation period in deionised water. A beeswarm plot of the normalised adhesion readings is shown in Fig. 3.17. With no enzyme present, the adhesion of the *M. luteus* biofilm is compromised by the deionised water, with a loss of adhesion of over 90% of the original readings. These findings show that deionised water is not a suitable medium to study the adhesion of *M. luteus*, which is likely to be due to osmotic stress it induces, so a control buffer was prepared.

When selecting the properties of the control solution to mimic, a domestic tap water supply was appealing as the commercial enzymes are optimised for such situations. The ion concentrations of domestic water supplies are similar to the final stages of the cantilever preparation, which will minimise the change experienced by the biofilm. The biofilm is known to grow successfully in two different levels of ionic concentration during the biofilm preparation protocol (Section 2.1.2). Domestic water supplies have slightly higher concentrations of Na^+ and Cl^- than those in the dilute growth medium, as seen in Table 3.4, which should pose no issue of osmotic shock to the established biofilm. The dilute growth media contains no Ca^{2+} or Mg^{2+} ions, but they are found in low levels in domestic water supplies, so have been included at the appropriate concentrations.

To properly gauge the effectiveness of enzyme activity against biofilms, they should be operating at their maximum ability. These enzymes are engineered for alkaline conditions found in domestic washing formulations, so two buffers were examined for this pH region, tricine and phosphate buffer. Tricine is able to buffer solutions between pH 7.4 and 8.8 and was used at a concentration of 25 mM and

Ion	Water Board conc. (mg/L)	Dilute Growth Media conc. (mg/L)	Control solution conc. (mg/L)
Na^{+}	200	195	200
Ca^{2+}	6.4	-	6.4
Mg^{2+}	2.4	-	2.4
Cl^{-}	250	305	342

Table 3.4: Ion concentrations in domestic water supplies, dilute growth media of *M. luteus* and the developed control buffer solution

adjusted to a pH of 8.4 with 1% KOH. A phosphate buffer solution can be tailored to a specific pH by adjusting the ratio of monobasic and dibasic sodium phosphates. A pH of 7.8 was targeted using 8.5 mL of monobasic sodium phosphate 0.2 M and 91.5 mL of dibasic sodium phosphate 0.2 M.

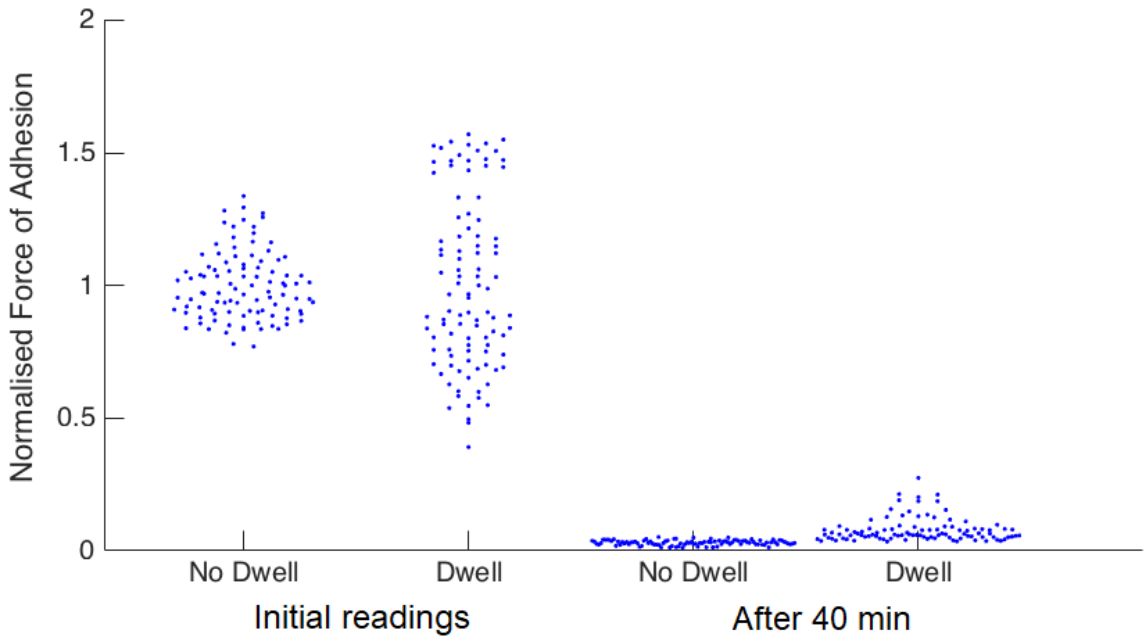

Figure 3.17: Bee swarm plot showing normalised adhesion values between a *Micrococcus luteus* biofilm cantilever and a PET thin film, before and after a 40 min incubation in deionised water.

Multiple biofilm cantilever experiments were conducted in this control domestic water supply buffered in tricine which resulted in a decrease of only 32 ± 1% adhesion. This continued decrease is likely due to the mechanical stresses experienced

during the contract process which will trigger a dispersion response.[121] When enzymes are present in the solution, any further decrease to adhesion beyond 32% can be attributed to the effects of the enzyme on the biofilm.

3.5 Enzymes

A variety of enzymes, all supplied by Novozymes A/S (Bagsværd, Denmark), were used to investigate the structural and adhesive roles of different components to the *M. luteus* biofilm. The four enzymes studied in most detail are listed in Table 3.5. Three additional enzymes were also explored to varying levels were Whitezyme (cellulase, glycosyl hydrolase 44), Stainzyme (α-amylase) and a new DNase named S3.

Table 3.5: Main enzymes used against *M. luteus*. Enzyme common names, commerical names and family/type.

Enzyme	**Commercial name**	**Family/type**
DNaseI	DNaseI	endonuclease
Protease	Savinase 16L	serine protease
Cellulase	Carezyme Premium 4500L	glycosyl hydrolase 45
Mannanase	Mannaway 25L	glycosyl hydrolase 5

The glycosyl hydrolases target the β-1,4 glycoside bonds between sugars, with the different types specifying alternative steric arrangements, as seen on the left side of Fig. 3.18. Also shown in this figure is that protease targets the peptide bond of proteins and DNaseI cleaves the phosphodiester backbone of eDNA.

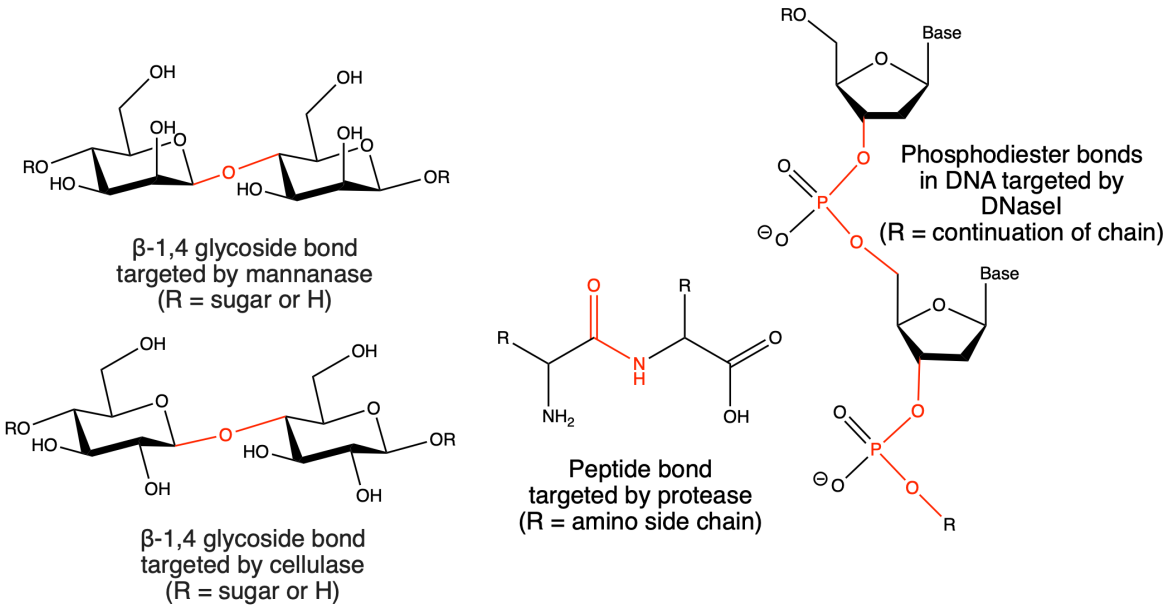

Figure 3.18: Examples of moieties in the EPS of bacteria targeted by the enzymes used in this work. The cleaved bonds are highlighted in red.

3.6 Confocal microscopy

Biofilms of *M. luteus* were cultured for 18 h on glass slides and their dispersal upon enzyme treatment was imaged using confocal microscopy.

3.6.1 Glass slide preparation

Glass slides were prepared as the bioprobes were in Section 2.1.2. Slides were submerged in a 1% poly-L-lysine hydrobromide solution (w/w %) for 2 h before incubating in *M. luteus* culture for 4 h and then in dilute growth media for 18 h. The slides were then submerged in imaging buffer containing the relevant enzyme (control slides used only imaging buffer) for 40 min before staining with BacLight (Section 2.1.3). Slides were gently rinsed in buffer before imaging in a Leica SP8 confocal microscope, employing images with a 10×/0.3 water dipped objective. Images were analysed and biovolumes calculated using Imaris (Bitplane, Belfast, UK) software using the surface creation wizard with upper and lower intensity thresholds set to automatic.

3.6.2 Biovolume

The term biovolume appears to have been popularised by a computer script developed by Arne Heydorn and Bjarne Ersbøll in 2000, called COMSTAT.[122] The script described biovolume as:

> the number of biomass pixels in all images of a stack multiplied by the voxel size [$(\text{pixel size})_x \times (\text{pixel size})_y \times (\text{pixel size})_z$] and divided by the substratum area of the image stack. The resulting value is biomass volume divided by substatrum area ($\mu m^3/\mu m^2$). Biovolume represents the overall volume of the biofilm, and also provides an estimate of the biomass in the biofilm.

With the value being a measure of volume over area, it could be argued that biovolume is a misnomer. However, it is a useful way of quantifying the coverage of biofilm over a surface. Imaris, a microscope image analysis software, is able to measure the volume of dyed material captured by confocal microscope Z-stacks. This value is then divided by the area of the surface to get an average biovolume coverage. By comparing these values before and after enzyme treatment, a viewpoint on the millimetre length scale can be obtained to complement the micrometre length scale provided by bioprobe AFM experiments.

After a 40 min incubation in enzyme, Z-stacks of the biofilms were captured from multiple glass slides, as shown in Fig. 3.19. All enzyme treatments caused decreases in biovolume with respect to control values, but only DNaseI was a significant change ($p<0.05$).

Table 3.6: Mean biovolume, standard error and p values for combined green and red channel data of 40 min incubation.

Enzyme	**Biovolume ($\mu m^3/\mu m^2$)**	**Standard error**	**p value**
(Control)	2.8	0.6	N/A
DNaseI	0.7	0.2	0.00 (0.0005)
Protease	2.0	0.5	0.37
Cellulase	1.7	0.4	0.17
Mannanase	1.3	0.2	0.18

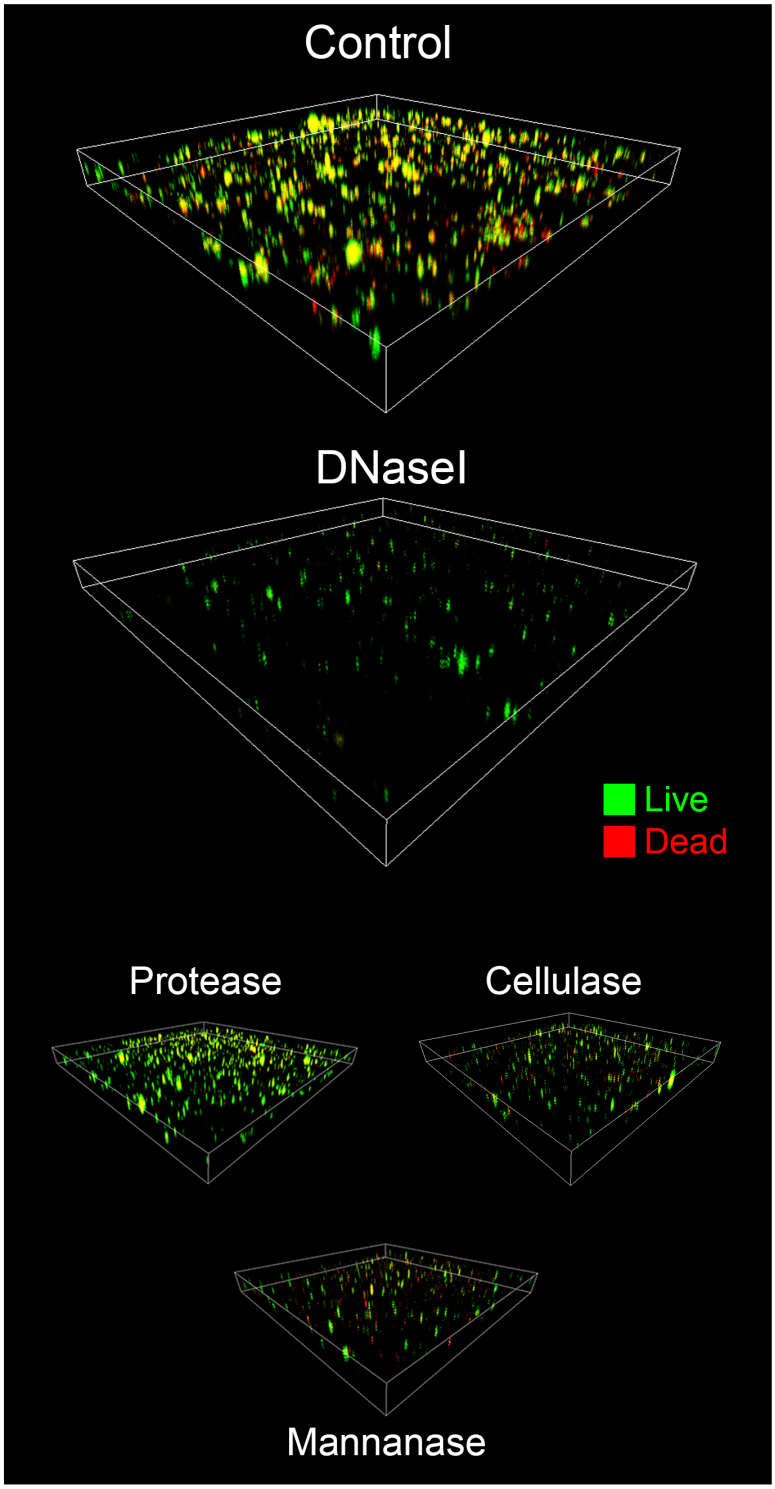

Figure 3.19: Three dimensional confocal microscopy Z-stacks of *M. luteus* biofilms after treatment with various enzymes. Stained with BacLight LIVE/DEAD dye. Compromised cells are stained red, live cells are stained green. Lateral dimensions of images are 1.16 mm.

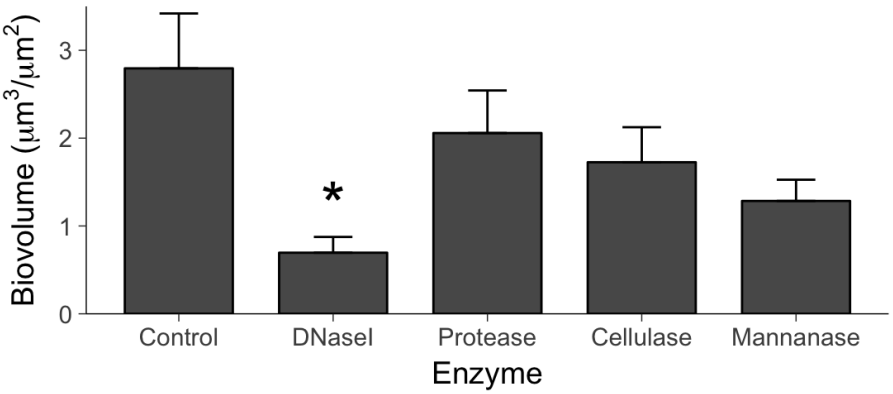

Figure 3.20: Bars represent the mean average biovolume, with the standard error shown by error bars. Asterisks indicate significant ($p<0.05$) reduction in biovolume. Green and red channel data combined.

3.6.3 Biofilm height

The Z-stacks obtained from confocal microscopy have the obvious advantage over traditional fluorescence microscopy of height data. Unlike the biovolume values, the height of the biofilms varied very little between control and enzyme treated samples, except for DNaseI which again had a significant (p<0.05) change.

Table 3.7: Mean biofilm heights, standard error and p values for combined green and red channel data of 40 min incubation.

Enzyme	**Biovolume height (µm)**	**Standard error**	**p value**
(Control)	93.8	3.6	N/A
DNaseI	68.3	2.6	0.00 (0.000006)
Protease	88.7	5.6	0.48
Cellulase	95.7	5.9	0.80
Mannanase	99.2	3.8	0.34

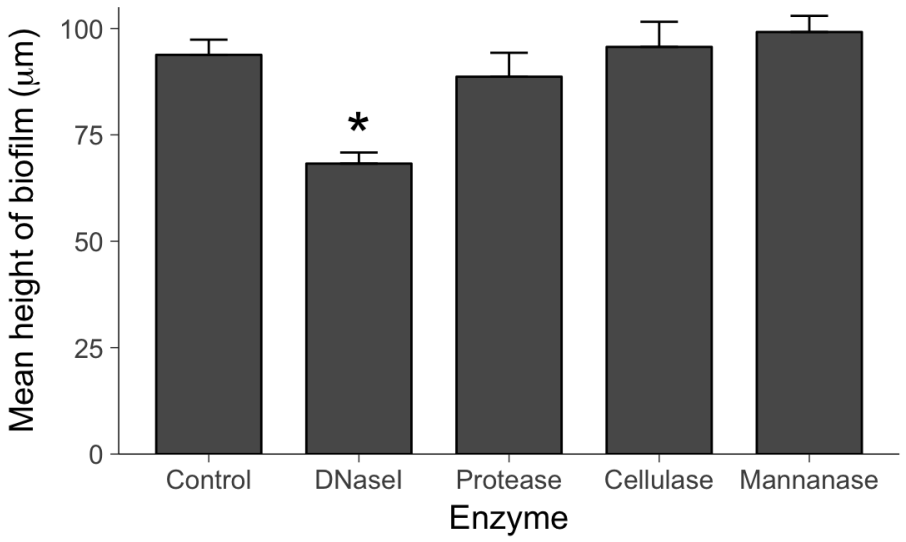

Figure 3.21: Bars represent the mean height of the biofilm, with the standard error shown by error bars. Asterisks indicate significant (p<0.05) reduction in height. Green and red channel data combined.

3.6.4 Confocal microscopy summary

After 40 min incubation, DNaseI was able to remove the majority of the biofilm (Table 3.6, 3.19 and Fig. 3.20) with the remaining height (Table 3.7 and Fig. 3.21) coming from tall spire-like structures, suggesting that these were the oldest parts of the biofilm.[123] This supports studies concluding that DNases are less effective against older biofilms,[105,124] which have been attributed to either eDNA being increasingly more shielded from the action of the enzyme by other biofilm components, or that eDNA is supplanted by other macromolecules. The three other enzymes examined using these methods resulted in non-significant changes to biovolume and height.

Fluorescence imaging, combined with binding assays, is a widely used technique that can give important information about the location of different components of a biofilm.[58,61,62] Such experiments have suggested roles for the different components based on the morphology of the structures that they form. However, to assess a demonstrable role for these molecules, it is necessary to interact with the biofilm in a different manner. Therefore, the bulk of this thesis is dedicated to force spectroscopy to investigate the effect that enzymes have on the interaction between *M. luteus* biofilms and PET surfaces.

3.7 Contact angle

Biofilms of *M. luteus* were grown on silicon wafer as described in Section 2.1.2 to be examined by contact angle measurements (see Section 2.2.4). The contact angle of a water droplet deposited on a biofilm gives information about the hydrophobicity of the assembly and is a way to assess surface cleaning. Bare silicon wafer was found to have a contact angle of 43° and untreated biofilms had a contact angle of 65°.

If treatment with an enzyme causes the contact angle to drop close to that of the clean substrate, it can be concluded that the cells have been dispersed and that the

hydrophobic EPS no longer coats the substrate. Therefore, contact angle measurements were captured before and after treatment with a control or enzyme solution for 40 min.

DNaseI, followed by protease, had the largest reduction in the contact angle of the residual biofilm compared to the untreated biofilm, differing by only 6° and 7° from bare silicon respectively (Table 3.8). The glycosyl hydrolases (mannanase and cellulase) did not change the surface properties of the biofilm by much, albeit more than the enzyme-free treatment.

Table 3.8: Contact angle measurements of a *Micrococcus luteus* biofilm on silicon wafers after treatment with enzymes. Contact angles are presented to the nearest degree, and the uncertainty associated with their measurement is small compared to this.

Contact angle of clean surface	Contact angle of biofilm before treatment	Treatment	Contact angle of biofilm after treatment	Difference between enzyme-treated biofilm and clean surface
43°	65°	DNaseI	49°	6°
		Protease	50°	7°
		Mannanase	61°	18°
		Cellulase	54°	11°
		(No enzyme)	64°	21°

3.8 AFM Results

Bioprobes were constructed by growing *M. luteus* biofilms on NPO-10 tipless AFM cantilevers (Bruker AFM Probes, Camarillo, CA, USA), as detailed in Section 2.1.2. The bioprobes were mounted on the piezoelectric mechanism of the AFM instrument and repeatedly brought into contact with the PET surface, while immersed in enzyme-free imaging buffer. The contact time to ensure the consolidation of adhesive bonds between the bacteria and the surface in each cycle was 10 s. One hundred force-separation curves were acquired in a 10×10 force map.

3.8.1 Control measurements

The biofilm is encouraged to grow on the cantilever by a poly-L-lysine (PLL) layer. It is important to know that the force-distance curves collected are detailing the interaction between the biofilm and PET substrate and not between PLL and the PET. Tipless cantilevers with a PLL coating, purposely lacking a biofilm, were tested against a PET substrate. Recording this type of interaction would enable identification of bioprobes without sufficient bacterial coverage in later experiments.

The force-distance curves from this control experiment feature a very distinctive appearance, as shown in Fig. 3.22. The PLL and PET interact so strongly that the piezoelectric motor is unable to overcome until forces greater than 60 nN are applied and the motor has pulled the cantilever back 4 µm. Using a cantilever with a stiffer arm (spring constant = 0.24 N/m) provides force-distance curves are obtained without the flat-bottomed feature of Fig. 3.22, but are notable for the high peak adhesion values and straight, featureless force-distance curve returning to equilibrium, as shown in Fig. 3.23.

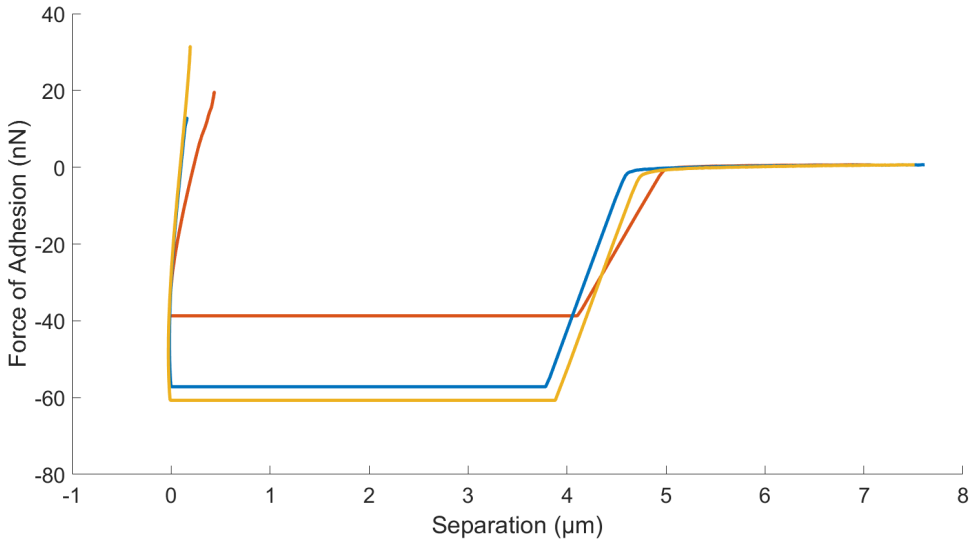

Figure 3.22: Force-distance curve of PLL interacting directly with a PET thin film. This general shape is observed with PLL of all weights when using a cantilever arm with a spring constant of 0.06 N/m or less.

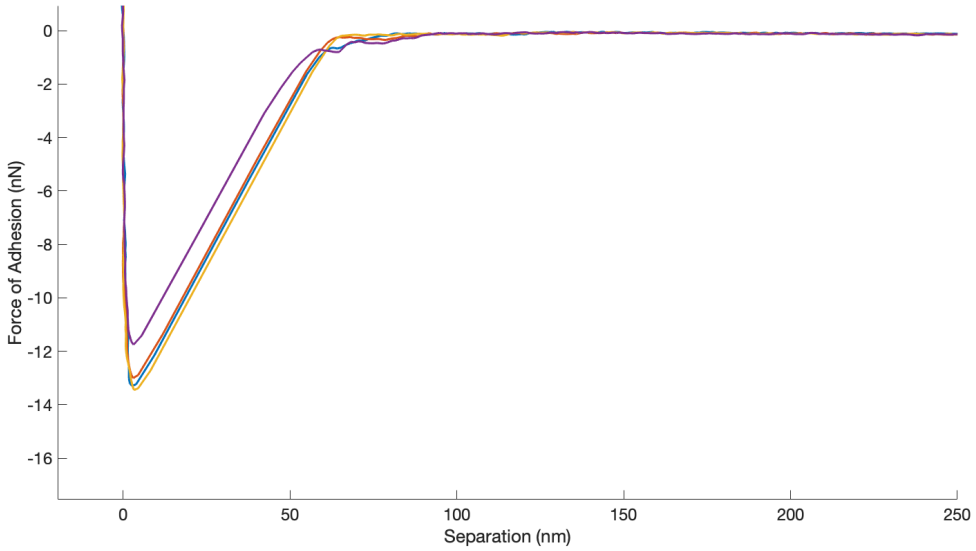

Figure 3.23: Four randomly selected retraction force-distance curves of poly-L-lysine coated tipless cantilever, with a nominal spring constant of 0.24 N/m, interacting with a PET substrate.

3.8.2 Peak adhesion

As the most basic form of analysis of the data contained in a force-distance curve, the peak adhesion of each interaction between bioprobe and substrate is obtained at the most negative force value of the retraction curve and usually occurs at minimum separation. Regardless of position, the value of each interaction can be obtained in any data processing software by finding the minimum value of the curve.

By obtaining these minimum values for all force-distance curves, a basic inspection of how adhesion changes can be undertaken as a starting point. To know what changes in adhesion are caused by the enzymes, any variation in the control measurements needs to be well understood.

Control experiments conducted in this imaging buffer have a much more acceptable decrease in adhesion of $32 \pm 2\%$ ($n = 3 \times 100$, $p \ll 0.05$). This drop in adhesion is likely to be due to the mechanical stress placed on the biofilm during force measurements, but this remains constant through all experiments.[121]

The enzyme experiments show a larger decrease in adhesion force of 92 ± 3% ($n = 3 \times 100$, $p < 0.05$) for DNaseI, 52 ± 12% ($n = 3 \times 100$, $p < 0.05$) for protease, 40 ± 5% ($n = 4 \times 100$, $p = 0.05$) for mannanase and 53 ± 7% ($n = 3 \times 100$, $p < 0.05$) for cellulase. These decreases in adhesion are displayed in Fig 3.24. These results indicate that *M. luteus* biofilms treated by hydrolases significantly decrease their adhesive force to a PET surface.

The reduction in adhesion after enzyme treatment suggests that either the key binding components have been removed from the biofilm, reducing its interaction with the PET surface, or that the biofilm itself has been partially dispersed. Either possible mechanisms indicates that the enzymes have cleaved the bonds that they target and that these components were used by the biofilm to attach to surfaces.

To better understand the effect these enzymes are having on the biofilm and the role of the targeted components, a greater degree of analysis is required, such as examining the primary and secondary events.

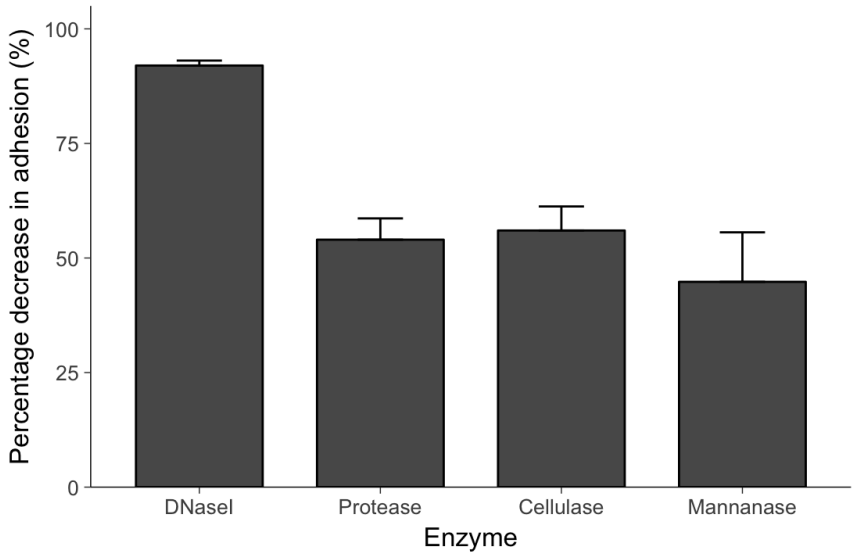

Figure 3.24: Bars represent the change in adhesion of bioprobes to PET substrate, with the standard error shown by error bars.

3.8.3 Primary and secondary events

A typical force-distance curve contains a wealth of data about how the bioprobe has interacted with the PET substrate. As the probe retracts from the surface, polymeric substances in the EPS that have become adhered to the substrate will be unwound and eventually rupture. These events are captured in the precise movement of the probe and recorded in the retraction curve. Although this information can be extracted manually from the curves, it is time consuming and open to error. For this reason, a custom MATLAB script was developed to quickly extract information from various types of curves. This script is detailed in Appendix A.1.

This MATLAB script quickly provides the separation and force values for each event recorded as the probe retracts from the surface. These values can the be explored for any variation in the biofilm caused by the different enzyme treatments. The separation values recorded for the interaction between the bioprobe and the PET may give detailed information about how various polymeric substances are altered by the enzyme treatment. A random force map pair of 100 points before and after enzyme treatment were analysed by the MATLAB script and the separation values of each force event obtained, shown in Fig. 3.25. The distributions are skewed towards a minimal value of separation, which is expected as most force events have a primary peak at minimal separation. Although there is variation across the force maps, there is overlap between the interquartile boxes not only between the before and after pairs of each enzyme, but also across all the force maps shown. This indicates that any change in the separation value of the force events caused by enzymatic treatment cannot be distinguished reliably using these AFM techniques. The polymeric substances being monitored here will have many degrees of freedom, allowing rapid reorientation and adhesion at different values of separation.

The script is also designed to log the number of events observed on each of the 100 curves in a force map. The force-separation curves obtained can also be analyzed in terms of the number of events per curve. As the probe retracts from the

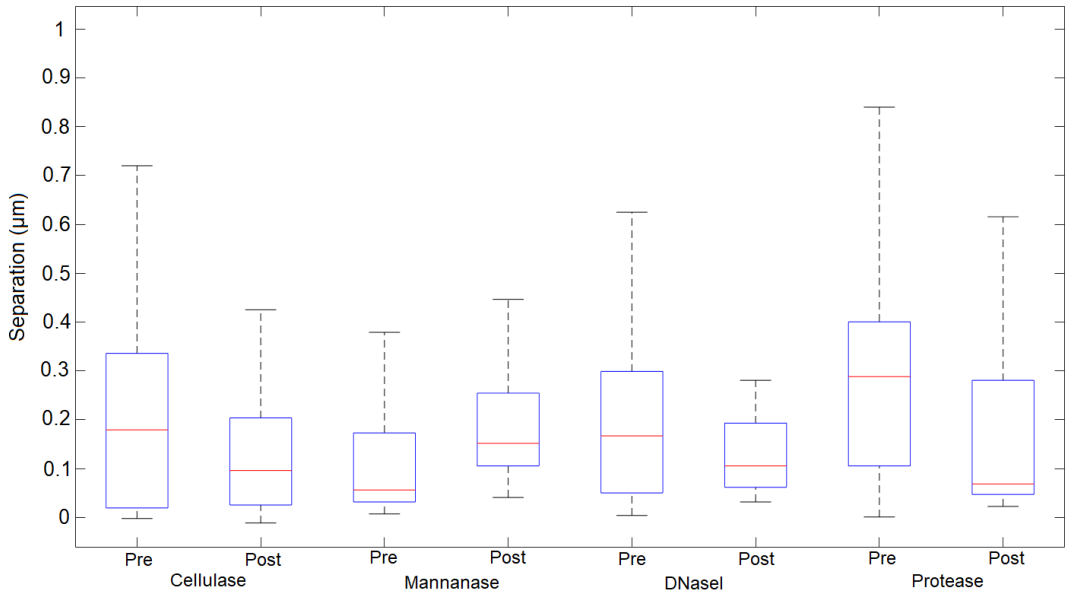

Figure 3.25: Box plots of separation values of force–distance events recorded before and after treatment with various enzymes.

surface, polymeric substances in the EPS that have become adhered to the substrate will be unwound and eventually rupture. These events are captured in the precise movement of the probe and recorded in the retraction curve. A bacterial biofilm can rapidly establish adhesive links when put in contact with a surface. If, upon enzyme treatment, the number of secondary events per curve decreased, it would follow that a proportion of the links that maintained the biofilm–substrate interaction has been lost.

As shown in Figure 3.27, DNaseI has the greatest impact in the reduction of secondary events, followed by protease. The glycosyl hydrolases (mannanase and cellulase) cause little change in the number and distribution of events. Thus, the cleavage of eDNA in a *M. luteus* biofilm causes a dramatic reduction in the number of links that maintained its adhesion to a PET surface, more so than the hydrolysis of proteins and polysaccharides. By analyzing the number of events after exposure to an enzyme, the role of the targeted EPS component can be categorised as structural or adhesive. A structural component is considered here as a core element of the

mesh that holds the biofilm together, so that its removal causes structural collapse and bacterial dispersion. This dispersion would be detected in force spectroscopy by a reduction in the number of anchor points (adhesion events) and a reduction in the force of adhesion. An adhesive component is taken here as a biomacromolecule that enhances the interaction capabilities of the periphery of the biofilm, which upon cleavage, diminishes its adhesive capacity, but does not critically affect the overall structure of the biofilm. The deterioration of adhesive components would then be characterized by a reduction in the strength of adhesion. Using these proposed definitions, it can be concluded that eDNA and proteins are both structural components, with the former having a larger effect in the overall structure, and that the polysaccharides function as nonstructural, peripheral, adhesive compounds.

Multiple bioprobes were tested for each enzyme, with a random choice for each enzyme displayed alongside each other in Fig. 3.26. The force spectroscopy experiments suggest that eDNA and proteins are the structural elements of the biofilm, as DNaseI and protease significantly reduced the number of adhesive contacts between an *M. luteus* biofilm and a PET surface (Fig. 3.27).

eDNA has been established as a functional component of the biofilms of many species, and the ability of DNases to disperse biofilms has been recorded.[105,124] This group of enzymes randomly cleave phosphodiester bonds to form phosphooligonucleotide end products. The force spectroscopy results show that disrupting the backbone of eDNA causes a near total loss of adhesion ($92 \pm 3\%$ reduction in the force of adhesion). Given that upon DNaseI treatment there was a complete loss of secondary interactions in the majority of force–separation curves (80%, Fig. 3.27), it can also be concluded that the degradation of eDNA caused the disassembly of proteins and polysaccharides. As it has been hypothesized that eDNA would bind with polysaccharides forming fibrils or anchored to proteins to form a mesh,[125,126] it is logical that the loss of eDNA, the key cohesive element of the mesh, disperses the assembly.

Proteins are also key elements of biofilms, performing structural and protective roles.[127] Proteases hydrolyze the peptide bonds in proteins, and in these experiments, the cleavage of this component provoked a decrease of 54 ± 12% in the adhesion of the biofilm to PET. Although substantial, the fact that some adhesion remains indicates that either eDNA and polysaccharides on their own can support the adhesion to the PET substrate or that an assembly of these and other biofilm matrix components render a number of proteins inaccessible.

These force spectroscopy experiments (Fig. 3.26) suggest that β-1,4-linked glycans and mannans are adhesive elements of the *M. luteus* biofilm, as cellulase and mannanase reduce the adhesion between the biofilm and surface, while leaving the number of bonds virtually unchanged (Fig. 3.27). Polysaccharides are an integral part of biofilms and can be composed of a wide variety of sugar monomers, linked with different connectivities and stereochemistries. Common polysaccharides in biofilms include β-1,4-D-glucans and β-1,4-D-mannans, and although research on the polysaccharide composition of *M. luteus* has not been extensive, the presence of lipomannans has been reported,[128] suggesting a possible sensitivity to mannanases. In other assays, cellulases and mannanases have been used to disperse lab strains,[83] medical,[103,129] and industrial[130] biofilms, with these enzymes commonly used in biofilm-dispersing compositions.

The mannanase used in this work is a glycosyl hydrolase belonging to the GH5 group, specifically to the enzyme class E.C.3.2.1.78 that catalyzes the endohydrolysis of the $(1 \rightarrow 4)$-β-D-mannosidic bonds. The use of mannanase against *M. luteus* biofilms decreases the strength of adhesion to PET by 40 ± 5%, having the smallest effect of all the enzymes tested. Upon treatment, the distribution of the number of secondary events per curve remained constant (Fig. 3.27), so no structural changes have been ascribed to the mannan component of the biofilm.

The cellulase used is a glycosyl hydrolase that belongs to the GH45 or E.C.3.2.1.4 class, and catalyzes the endohydrolysis of the (1→ 4)-β-D-glycosidic bonds. Cellulase reduced the biofilm–substrate adhesion substantially (53 ± 7%). This large decrease in the strength of adhesion indicates that polysaccharides containing these linkages are important for the interaction of the *M. luteus* biofilms to a hydrophobic substrate. The analysis of the secondary events reveals that the number of attachment points remains unchanged, and hence the role of cellulose like polymers in this biofilm has been categorised as adhesive.

To the author's knowledge the characterisation of components in a biofilm by using enzymes to manipulate biological targets has not been conducted before. This method of physically interacting with a biofilm before and after incubation with an enzyme allows for new insights that traditional methods are not able to produce.

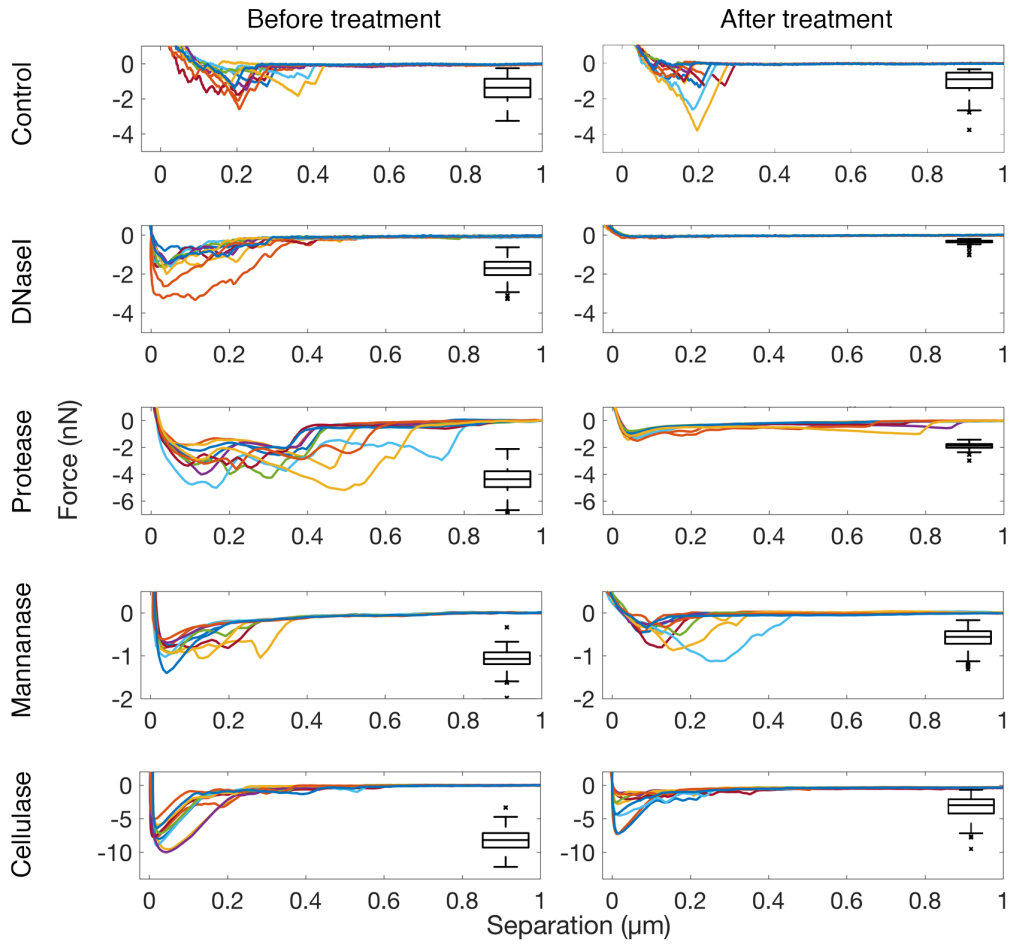

Figure 3.26: Force-separation retraction curves before (left) and after (right) treatment with specific enzymes. Each plot overlays 10 *randomly* selected curves and is representative of all measurements. The boxplots denote the distribution of adhesion, that is, the magnitude of the primary peak of adhesion. Each boxplot corresponds to a single pair of force maps, comprising 100 biofilm-substrate interactions each. The top and bottom edges of the box are the 25th and 75th percentiles (quartiles) of the data, with the middle bar being the median value. The whiskers extend from their respective quartile to a spread of 1.5 times the interquartile range. Any data outside of this range are marked on the plot by a cross. The data marked "before treatment" were obtained using the same biofilm as the corresponding data marked "after treatment".

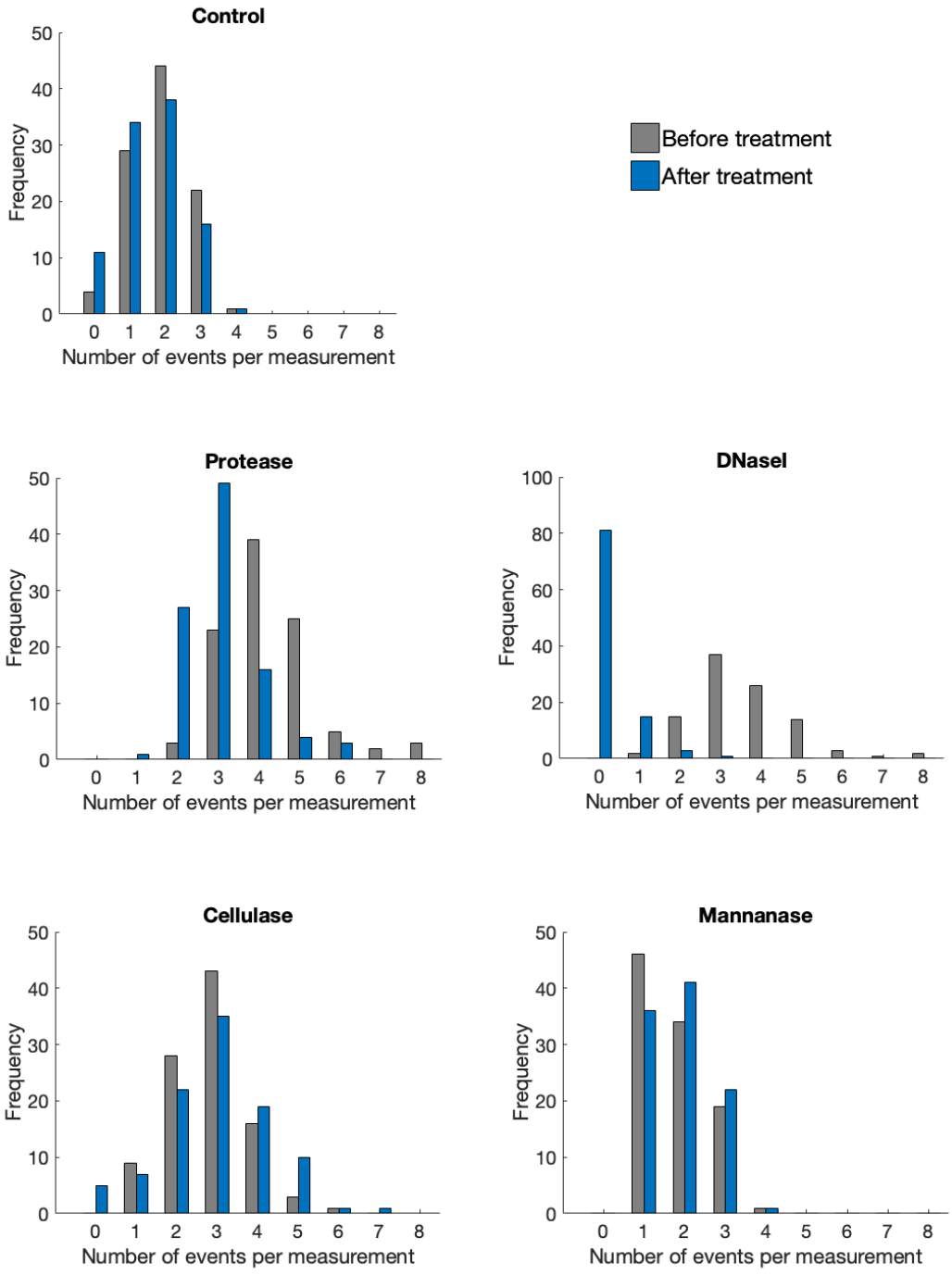

Figure 3.27: Bar charts showing the number of secondary events per force–separation measurement before and after treatment with each enzyme. Each plot corresponds to a single pair of force maps, comprising 100 biofilm-substrate interactions each.

3.8.4 S3 and S3 mutant

An additional DNase molecule, named S3, was supplied by Novozymes to be explored using the AFM method. *M. luteus* bioprobes were prepared in the usual manner and S3 was diluted to 0.2 mg/L in control buffer. This enzyme was stored at $-20\,^{\circ}\mathrm{C}$ unlike the other enzymes examined in this project, which were stored at $4\,^{\circ}\mathrm{C}$. The solution was supplied at a concentration of 3.17 mg/mL of active protein.

Initial bioprobe measurements against a PET thin film resulted in an increase in adhesion due to a large peak at zero separation (Fig. 3.29-B). When these peaks are temporarily excluded, a range of smaller interactions are noticeable which share similar events at certain separation values (Fig. 3.29-C). This grouping of post-treatment adhesion events has not been observed with other enzymes which suggested it was related to the enzyme molecule itself. The repeating events occur at 1 μm and similar shaped events at larger extensions between 2 and 2.5 μm. The shape of these interactions is also observed in a small amount of the large post-treatment events between 2 and 3.5 μm (Fig. 3.29-B). A second cantilever treated with S3 showed similar sharp peaks at low separation and step wise interactions at many microns separation, shown in Fig. 3.30. The type of force-distance curve shown in Fig. 3.30 is characteristic of a polymer unfolding, stretching and breaking. This evidence suggests the biofilm is being transformed in a way not seen with the previously tested enzymes.

To investigate whether the enzyme was removing the biofilm or the adhesion was due to bacteria remaining coated to the cantilever, confocal microscopy images were captured from *M. luteus* biofilms on glass slides (see Section 2.1.2). Both two-dimensional and three-dimensional Z-stacks were captured using BacLight as a fluorescent stain. As Fig. 3.28 shows, the biofilm is clearly removed by S3 treatment, leaving little bacterial matter on the glass slide. Regions of the biofilm that appear more built up, suggesting a greater age, have been able to resist treatment, which was also seen in DNase results. The large length scale that is incompatible with

proteins being stretched,[131] suggests that the large adhesion events observed in AFM measurements (Fig. 3.29) may be due to the remaining isolated parts of the biofilm interacting with the substrate.

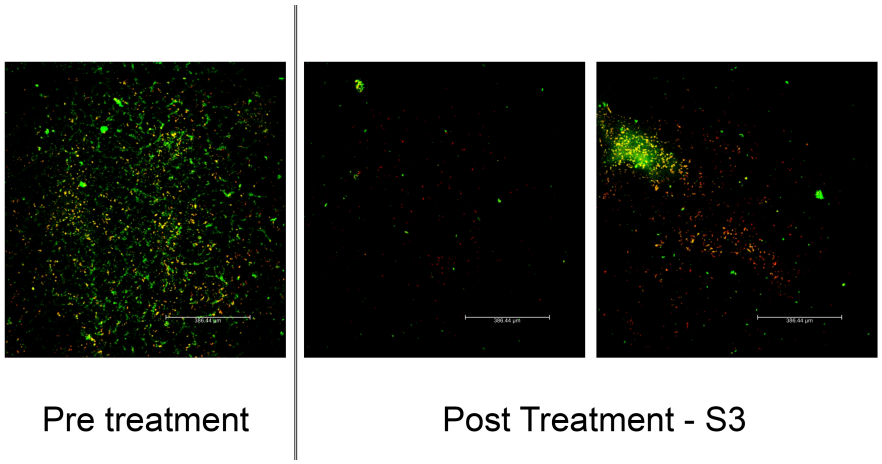

Figure 3.28: Top down view of combined confocal Z-stacks of *M. luteus* biofilm before and after treatment with S3 enzyme. Stained with BacLight LIVE/DEAD dye. Compromised cells are stained red, live cells are green. Scale bars are 386.44 µm.

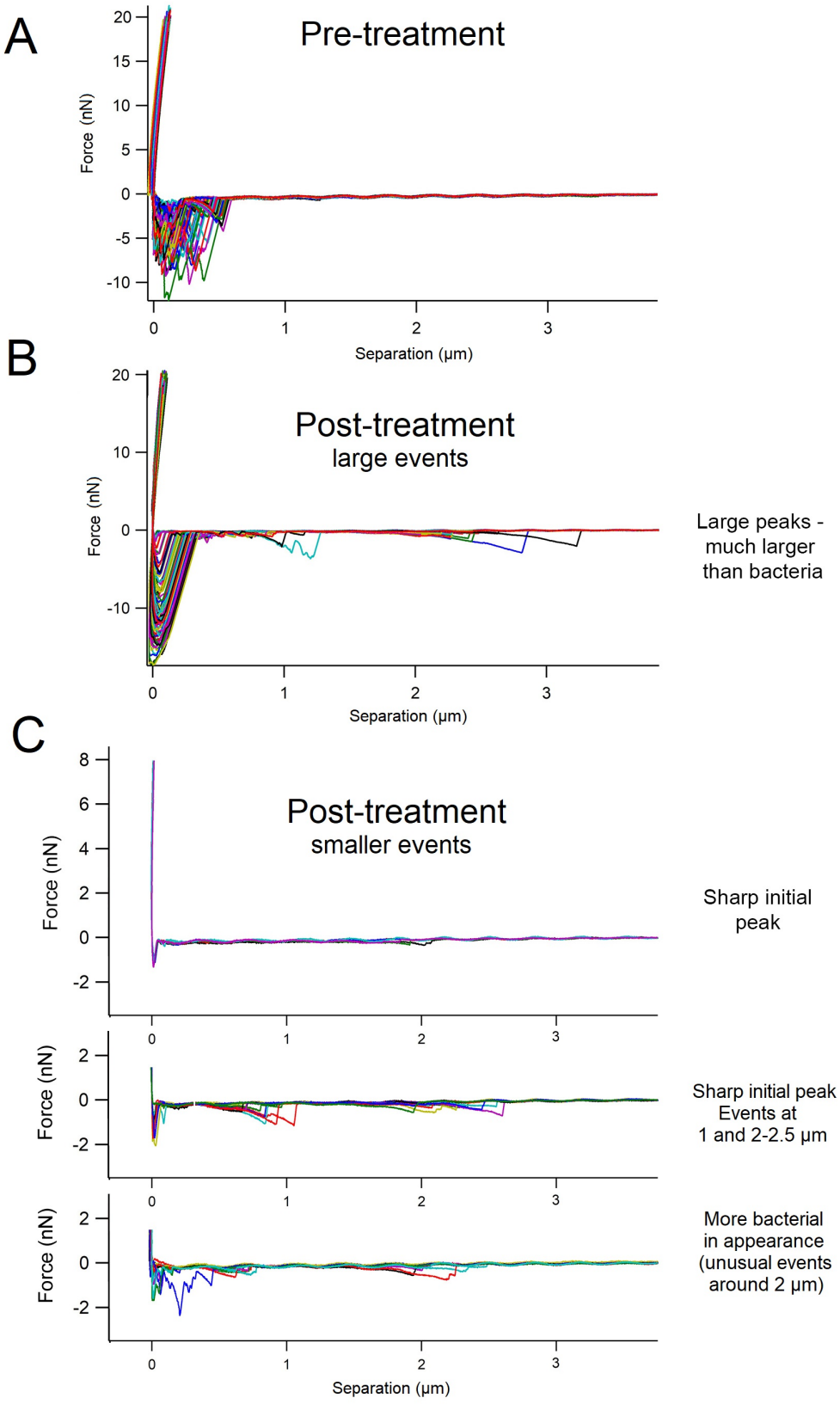

Figure 3.29: Comparison and categorisation of force-distance curves after S3 treatment.

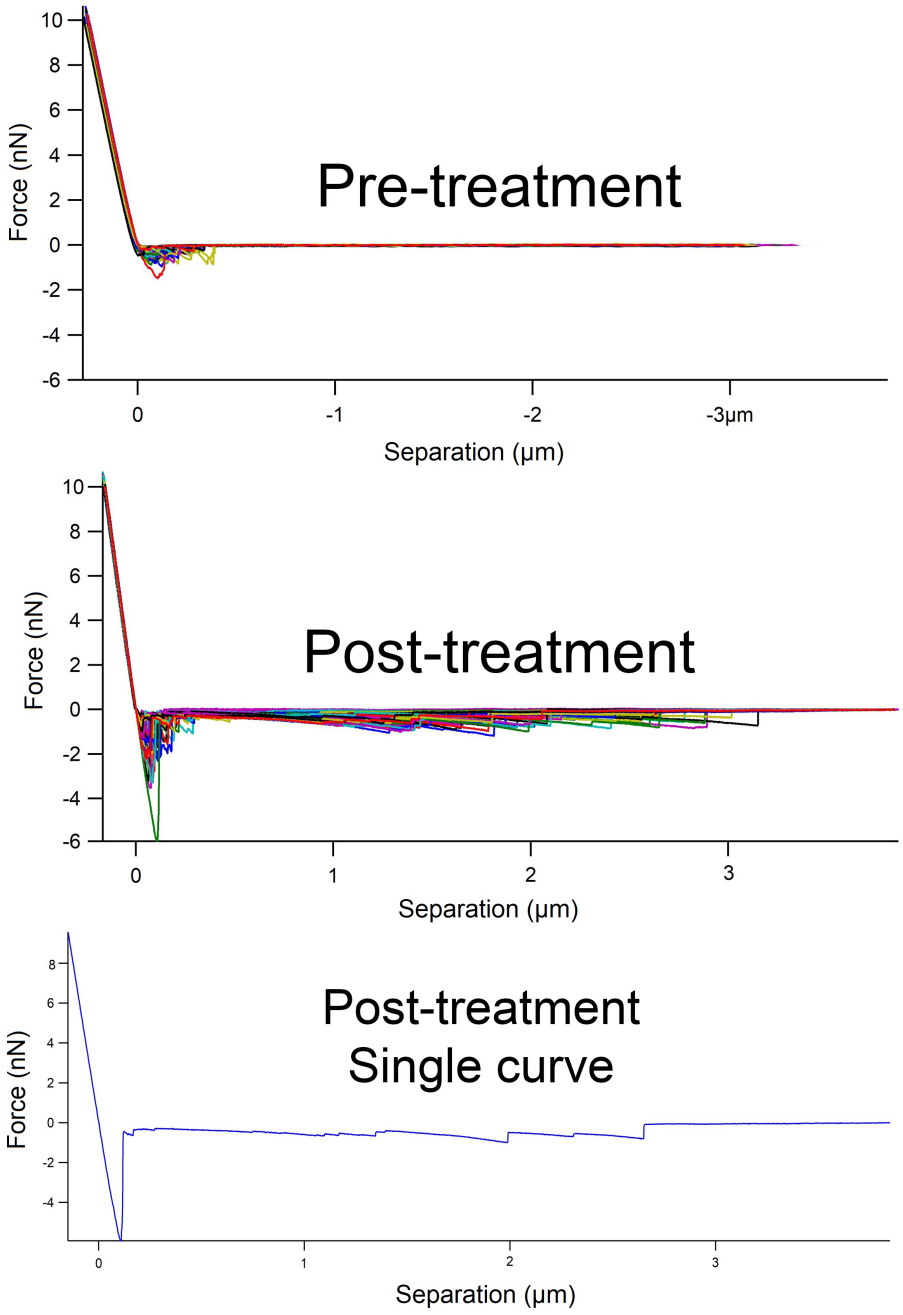

Figure 3.30: Comparison of force-distance curves after S3 treatment.

S3 Mutant

Confocal microscopy and AFM measurements suggest that there is an effect related to the S3 molecule activity on the biofilm that is responsible for the interactions observed in Fig. 3.29 and 3.30. To confirm this, a mutant variant of the molecule was provided by Novozymes. This protein has the same structure as the S3 molecule, but the active site has been disabled. Bioprobe experiments using the mutant variant mostly show a decrease in force equal to that seen in control measurements where no enzyme is used, confirming the lack of activity from the mutant. In two force maps, step wise adhesion events at multiple micron extension were observed, as shown in Fig. 3.31. The similar form of interactions are observed with the mutant as with the active S3 molecule, indicates that the mutant still has some activity against the *M. luteus* biofilm. When S3 DNase is diluted further to 10% (0.02 mg/L) of the industrial enzyme concentration (0.2 mg/L), featureless curves that resemble DNaseI results (Fig. 3.26) are observed. By analysing all of this data, an enzyme-concentration dependent effect is indicated. Further analysis of this novel S3 DNase is required to see how and why its behaviour differs from traditional industrial enzymes.

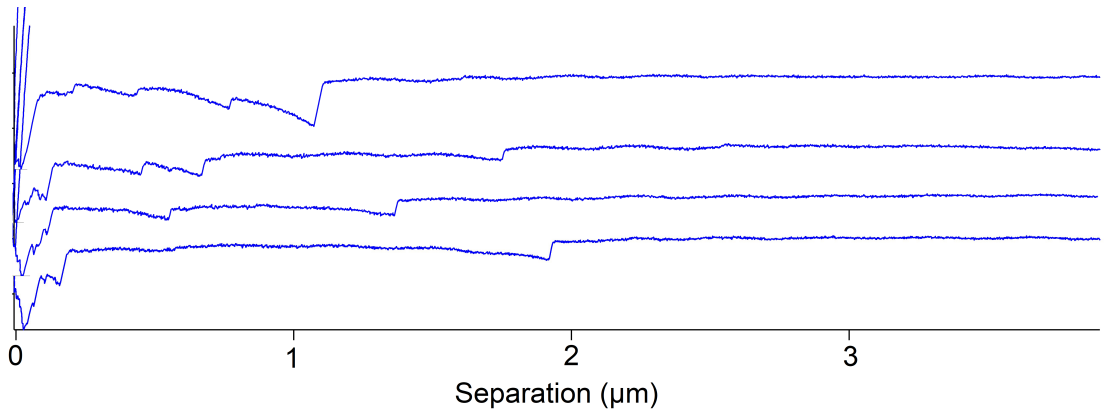

Figure 3.31: Vertically offset selection of force-distance interactions of a *M. luteus* biofilm cantilever with a PET thin film, in S3 mutant solution.

3.9 Conclusions

Force spectroscopy is able to give detailed information about how the biofilm binds to a model surface. The primary event usually has the largest adhesive force and indicates how strongly the biofilm and the substrate are attached to each other. The secondary peaks give finer details about the nature of the binding. After enzyme treatment, if the primary event decreases in magnitude, but a similar number of secondary peaks remain, some bacterial dispersion has taken place, without much change in the density of adhesive contacts. The interactions remain the same, and there is just less adhesive material present. The substance targeted by the enzyme is therefore classified as adhesive in nature. This is supported by contact angle measurements (Table 3.8), which show that the glycosyl hydrolases (cellulase and mannanase) cause minimal change to the surface energy of a biofilm on a silicon wafer.

If the secondary events do alter, a change in the structure of the biofilm can be concluded. Whole sections of the biofilm may have been cleaved and jettisoned, taking adhesive material with it. eDNA and proteins are categorised as structural components for this reason. With a change in secondary events, we can conclude there has been a change in the structure of the biofilm. When eDNA is targeted, polysaccharides and other components are lost, leading to the classification of eDNA as a structural component. Because of the large loss of material after DNaseI treatment, it is not possible to ascertain the level of contribution that eDNA has to the adhesive properties of the biofilm.

Targeting proteins also changes the distribution of secondary events, albeit to a lesser extend than the targeting of eDNA. However, the change in contact angle after protease treatment suggests there is a minor change in the biofilm structure that allows greater ingress of water. Therefore, protease is categorised as causing a minor structural change in the *M. luteus* biofilm.

The use of confocal microscopy in tandem with force spectroscopy leads to logical answers to the changes being observed in these complex arrangements of bacteria and polymeric substances. This work demonstrates the importance of perturbing the biofilm to obtain key adhesive and structural information, rather than relying simply on optical images.

By identifying efficacious enzymes and understanding their discrete effects in the behaviour of the whole assembly, new targets for biofilms can be identified and superior enzymes can be designed to disperse biofilms, with medical and industrial applications. As DNase was particularly potent against the *M. luteus* biofilm, it was subjected to further study in Chapter 4.

Chapter 4

Investigation of the mechanism of S3 DNase

4.1 Introduction

Chapter 3 illustrates the importance of extracellular-DNA (eDNA) to the structural stability of *Micrococcus luteus* biofilms, demonstrating that DNase had significantly greater effects on the biofilm than the other enzymes that were investigated. A new DNase, S3, was also explored for its effects on biofilms and was found to provide the same disruption at one tenth of the concentration of DNaseI. To gain more understanding of S3 DNase and its mechanism of action, the facilities and procedures of this project's industrial partner, Procter & Gamble (P&G), were used.

Due to the nature of their business needs, P&G's procedures and data collection are oriented towards real world wash conditions. Some of these techniques, while unfamiliar to those in traditional academic settings, provide repeatable and quantitative results. These findings drive innovation as well as being used in legal courts to defend intellectual property and commercial claims. The hydrolytic action for S3 DNase is believed to be a hopping mechanism, where the highest activity is achieved when the enzyme can easily move on and off the substrate (Fig. 4.1)**??**. The methods described in this chapter were used to investigate this possibility.

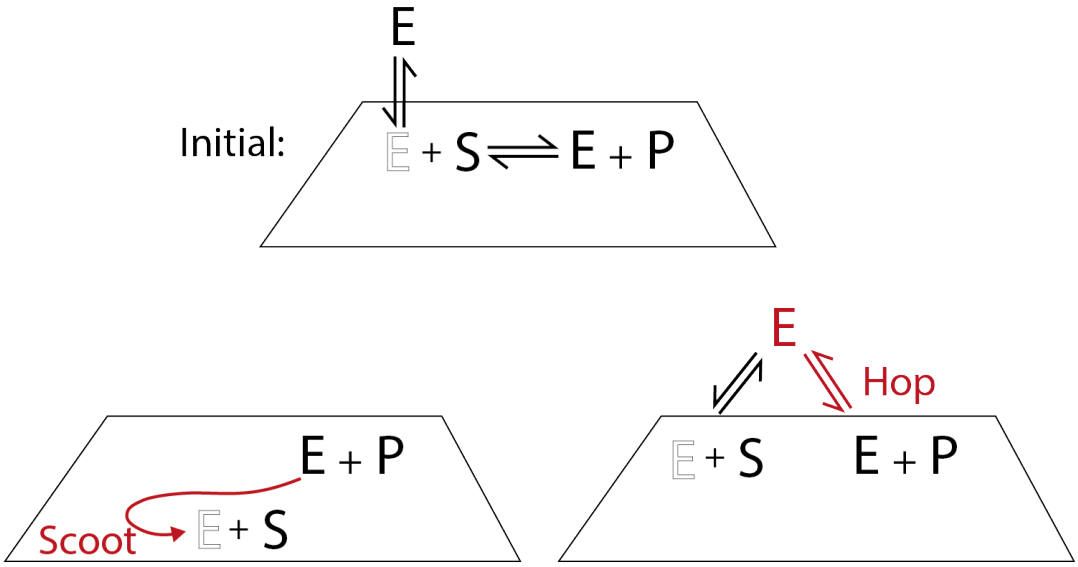

Figure 4.1: A diagrammatic representation of the differences between scooting and hopping mechanisms for interfacial catalysis.[132] After the enzyme (E) initially adsorbs to the surface, it will react with the substrate (S) and catalyse the forward reaction to create product (P). If the enzyme follows a scooting mechanism, it will remain at the interface for many catalytic cycles. If it follows a hopping mechanism, it returns to solution each cycle, before readsorbing elsewhere.

Equation 4.1 illustrates the basic reaction mechanism for an enzyme (E) and its substrate (S), catalyzing the reaction (ES^*) to produce the end product (P). For S3 DNase, the substrate is DNA and the end product comes from hydrolysing the phosphodiester bonds. If the proposed hopping mechanism is valid, k_1 and k_4 will be the major factors of reaction rate.

$$E + S \overset{k_1}{\rightleftharpoons} ES \overset{k_2}{\rightleftharpoons} ES^* \overset{k_3}{\rightleftharpoons} EP \overset{k_4}{\rightleftharpoons} E + P \tag{4.1}$$

Many factors affect enzyme activity in a wash cycle including temperature, ionic strength, wash duration and detergent composition.[88,133] A set of model DNA stains on polyester fabric swatches were subjected to a small-scale wash cycle in identical 1 L vessels, to explore these factors. The interaction between enzymes and surfactants has been a known issue since they were first introduced (See Section 1.7), which can either help or hinder activity.[134,135] The chemical contents of the wash liquid can be

varied across these vessels and the changes in DNA stain compared. This technique provides a large amount of data that can be interpreted in the statistical analysis program, JMP.

Once a broad analysis has taken place, more specific variables can be explored for their individual contributions to the action of the enzyme on the DNA stain. To achieve these results in an economically and time-favourable manner, a method known as Design of Experiments (commonly referred to as DoX) is used. A DoX method requires only certain points of the variable space to be found and relies on statistical software to interpret the unexplored space. The software produces a model of relevant variables which needs to then be verified.

To validate the model, experiments using a quartz crystal microbalance with dissipation monitoring (QCM-D) were conducted. QCM-D provides information about how the enzyme and other components of the wash solution settle on a surface and also how they are released. QCM-D enzyme studies have successfully been used to classify enzyme mechanisms,[136] as well as explore kinetics for a range of different enzymes families.[137,138] Furthermore, ionic surfactants that are included to bind to the fabric substrate and particulate soils are known to bind strongly to proteins.[134] This interaction may well play a dominant role in mediating the access of enzyme to the surface or facilitating the detachment into solution, as it does with particulate matter driven by counterion entropy.[134] By examining the variables of interest indicated by the DoX results using QCM-D, the statistical model and the hypothesis of enzyme action can be accepted or rejected based on physical data.

4.2 Experimental methods

4.2.1 DNA stain preparation

Polyester fabric was obtained from Warwick Equest (County Durham, United Kingdom) and cut into 5×5 cm squares. A 10 mg/mL solution of DNA was prepared by dissolving DNA sodium salt from herring testes (D6898, Sigma-Aldrich, now Merck) in deionised water and mixed using a stirrer bar for 2 h. The solution appeared hazy and became viscous. Each stain required 1 mL of final solution. After 2 h, $CaCl_2 \cdot 2\,H_2O$ (62 mg/mL) was added to the stirring DNA solution and stirred for a further 30 min. Methyl green zinc chloride salt (Sigma-Aldrich) was added (1 mg/mL) to the solution and stirred until homogeneous.

The stain solution (1 mL per swatch) was placed onto polyester swatches using a positive displacement pipette (Mettler Toledo MR1000) with positive displacement tips (Gilson CP1000). The swatches were left in a drying oven at 35 °C for 48 h.

After the stains had been dried, those that were not approximately circular were rejected as uneven. Accepted swatches were labelled in the corner of the fabric, away from the stain, and imaged using a DigiEye colorimeter system (VeriVide, Leicester, United Kingdom).

4.2.2 Automated washing cycle

Washing cycles were conducted in a laboratory scale, multiple washing pot machine, manufactured by Peerless Systems (Tyne and Wear, United Kingdom). This machine mimics a North American high efficiency top-loader washing machine, with ten identical 1 L wash pots, each with an agitator. The agitators are connected to the same fan belt, so all turn at the same speed. The individual pots all draw from the same water source and at the same rate. This water source can be changed between three levels of hardness, soft (1.4 mg/L $CaCO_3$), city (120 mg/L $CaCO_3$) and hard (325 mg/L $CaCO_3$).

To account for a realistic washing load, 50 g of cotton swatch ballast is added to each wash pot alongside the stained swatches. Surfactants, enzyme and fabric swatches were manually loaded using syringes when required by the washing system. Standard wash conditions were as follows:

1. Wash pots were filled with 'city' water at 25 °C
2. Surfactants and enzyme were added, stirred for 1 min
3. Half of the cotton ballast was added, sample swatches, then the remaining ballast
4. Wash cycle proceeded for 17 min, agitator speed of 208 rpm, 25 °C temperature
5. Wash pots were drained by high speed spinning
6. Wash pot were filled with chilled rinse water at 15 °C
7. The rinse cycle proceeded for 5 min, with an agitator speed of 208 rpm
8. Wash pots were drained by high speed spinning

The stained swatches are removed from the wash pot and allowed to dry in the dark for 12 h. The swatches are imaged by the DigiEye system described in Section 4.2.1 and compared against the images taken before the wash cycle.

4.2.3 Stain Removal Index (SRI)

Stain removal index (SRI) is a method for standardising the colour intensity of stains before and after they have been exposed to a cleaning treatment. It is a 0-100 scale, where 0 indicates no stain removal and 100 indicates total removal of the stain. The index uses the L*a*b* colour space (shown in Fig. 4.2), defined by the International Commission on Illumination (CIE). Colour is expressed as three separate values:

- L^*: lightness of the colour, from black (0) to white (100)
- a^*: from green (negative) to red (positive)
- b^*: from blue (negative) to yellow (positive)

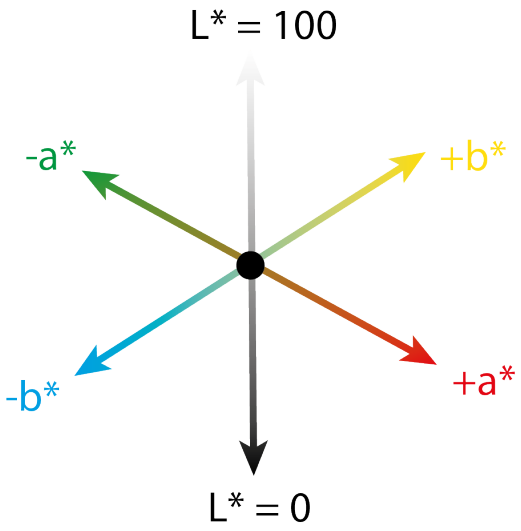

Figure 4.2: The L*a*b* colour space, represented in three dimensions.

To calculate the SRI of a formulation, two differences must be calculated, ΔE_a and ΔE_b. ΔE_a is the colour difference between the washed stain and the unwashed fabric and ΔE_b is the colour difference between the unwashed stain and unwashed fabric. These values and how they are caluclated are demonstrated in Fig. 4.3. Using these changes, the SRI is calculated by:

$$SRI = 100 \times \frac{\Delta E_b - \Delta E_a}{\Delta E_b}. \tag{4.2}$$

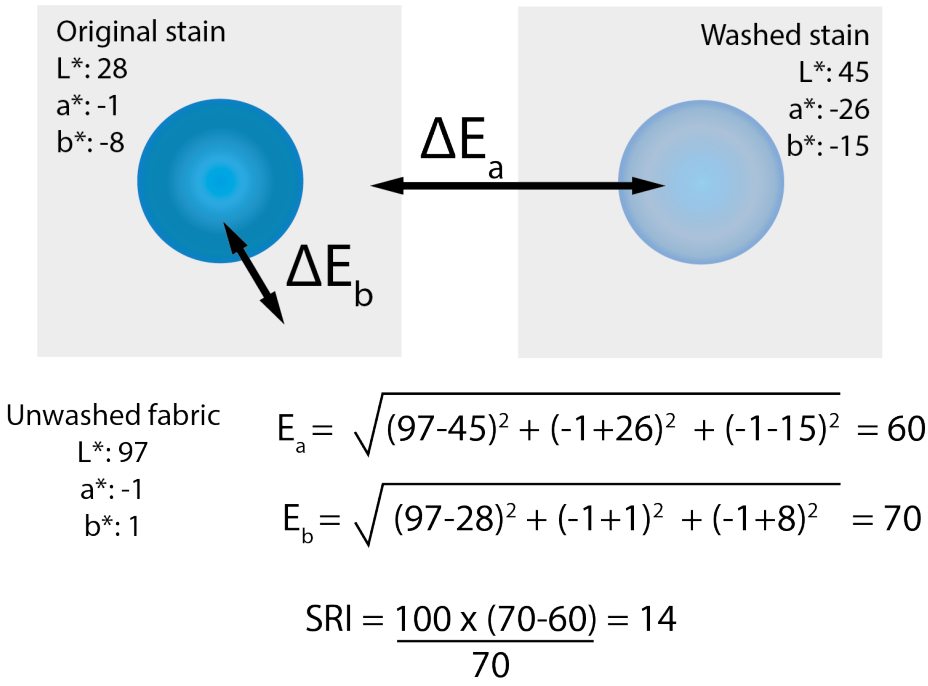

Figure 4.3: A schematic diagram of a stain on polyester fabric, with a demonstration of how the values of ΔE_a and ΔE_b are calculated with simplified L*a*b* values.

4.2.4 Enzyme-linked immunosorbent assay (ELISA)

Enzyme-linked immunosorbent assay (ELISA) was first reported as a method in 1972 to replace the more dangerous method of radioimmunoassays.[139] All preparation of the solutions used in this method are described in Section 4.2.5 and 4.2.6. Enzymes were extracted from polyester or cotton tracer swatches by placing individual samples into a 50 mL centrifuge tubes with 10 mL sample preparation buffer and rotated for 45 min at 40 rpm. The fabric samples were then left fully submerged at 4 °C overnight (this can be extended if required when working with low enzyme concentrations).

The plastic wells of a microtitre plate are able to bind proteins. Firstly, the plate was coated with 100 µL capture antibody solution for 12 hours, which is specific to the target protein to be measured (Fig. 4.4 - Step 1). The plate was washed three times with 200 µL of ELISA wash buffer to remove loosely bound protein. After each addition of wash buffer, the plate was inverted and tapped upside down on

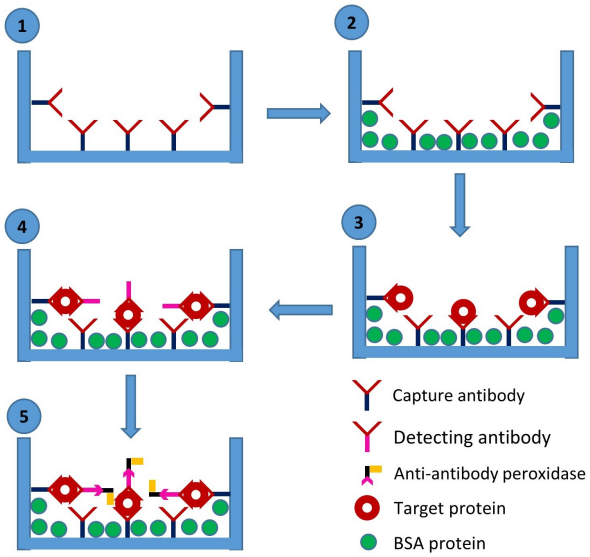

Figure 4.4: Schematic representation of the ELISA process in a single well. 1) Well coated with capture antibody, 2) free space blocked with BSA, 3) sample added and captured, 4) detecting antibody sandwiches sample, 5) anti-antibody peroxidase with signal attaches to sandwich complex

paper towel. Bovine serum albumin (BSA) protein (200 µL) was added to the well for 1 h to block nonspecific binding sites (Fig. 4.4 - Step 2) before repeating the washing step.

Known enzyme standards and the extracted enzyme samples (100 µL) were deposited into appropriate wells, in duplicate and left for 1-1.5 h to allow bindings to the capture antibody (Fig. 4.4 - Step 3). The plate was washed again and 100 µL of the detecting antibody solution was added to each well for 1 h (Fig. 4.4 - Step 4). The washing process was again repeated before 100 µL of anti-antibody peroxidase solution was added to the wells for 1 h. The plate was washed again and 200 µL of citrate buffer added to each well to adjust the pH to approximately 5. Following this, 200 µL of OPD solution was added to each well and the plate was incubated at 37 °C until a bright colour developed. Sulfuric acid (1 M, 100 µL) was added to each well to change the colour to a dark orange (Fig. 4.4 - Step 5). The plate was then read at 490 and 620 nm by an automated spectrophotometer.

4.2.5 ELISA buffers

All of the buffers listed below can be stored for 2 months at 4 °C.

Capture antibody buffer

Sodium carbonate (1.51 g) was dissolved in approximately 500 mL of deionized (DI) water. Sodium bicarbonate (2.93 g) was dissolved in approximately 500 mL of DI water and the two solutions combined in a 1000 mL beaker. The pH should be 9.6 ± 0.2. If it is outside this range, it is discarded and remade. The solution is transferred to a 1000 mL volumetric flask and made up to 1 L.

Wash buffer

Sodium chloride (29.22 g), Trizma® base (1.86 g) and bovine serum albumin (1 g) were weighed out and dissolved in 1000 mL of DI water. The pH was adjusted to 8.0 using concentrated hydrochloric acid. Tween 20 (0.5 mL) was added to this final solution.

Sample Preparation Buffer

Trizma® base (0.93 g), sodium thiosulfate pentahydrate (4.96 g), calcium chloride dihydrate (0.147 g) and sodium chloride (29.22 g) were weighed out and dissolved in 800 mL DI water with mixing. Bovine serum albumin (BSA) (1.0 g) was added slowly and allowed to dissolve. The pH was adjusted to 8.0 using concentrated hydrochloric acid. The solution was transferred to a 1000 mL volumetric flask with 1 mL of Tween 20, made up to 1000 mL with DI water and mixed.

Citrate buffer

Citric acid monohydrate (7.30 g) and $Na_2HPO_4 \cdot 12\,H_2O$ (23.87 g) were weighed out and dissolved in 1000 mL of DI water. The pH should be 5.0 +/- 0.2. This can be adjusted with 50% w/w concentrated sodium hydroxide or concentrated hydrochloric acid as required.

4.2.6 ELISA solutions

Fresh amounts of these solutions are made for each plate to be developed. All amounts given provide enough solution to fill an entire plate with some excess provided, with the exception of the BSA blocking solution which is made in small stock solutions to be replaced weekly.

Capture antibody solution

11 μL of capture antibody serum was diluted in 11 mL of capture antibody buffer.

BSA blocking solution

Bovine serum albumin (2.0 g) was dissolved in 100 mL of sample preparation buffer. The solution can be stored at 4 °C for 1 week.

Detecting antibody solution

Detecting antibody serum (11 μL) was dissolved in 11 mL of BSA blocking solution.

Anti-antibody peroxidase solution

Anti-antibody peroxidase (11 μL) was dissolved in 11 mL of BSA blocking solution.

OPD substrate solution

A single *o*-phenylenediamine (OPD) tablet (15 mg) was dissolved in 30 mL citrate buffer and allowed to dissolve without agitation. **DANGER: OPD is toxic and carcinogenic. Handle with caution and change gloves after use.** After the tablet has dissolved, 20 μL of 30 % hydrogen peroxide was added and gently mixed.

4.2.7 Hydrophilicity index (HI)

The hydrophilic index is a 0-20 scale of surfactant compositions, where a value of 20 indicates entirely hydrophilic molecules and a value of 0 indicates entirely hydrophobic molecules. The equation to calculate the HI of an individual surfactant component (HI_S) is given as:

$$HI_S = \frac{20 \times (\text{mol. weight of the hydrophilic portion of the component})}{(\text{mol. weight of the component})}, \quad (4.3)$$

and the HI of the surfactant composition as a whole (HI_C) is given as:

$$HI_C = \sum_y ((\text{weight \% of surfactant y in the system}) \times (HI_S \text{ of surfactant y})) \quad (4.4)$$

Worked example

To find the HI of a surfactant system containing 70% weight sodium dodecyl sulfate (SDS) and 30% weight alcohol ethoxylate 24-7 (AE 24-7) the individual surfactant HI values (HI_S) are first calculated.

The molecular weight of the hydrophilic portion of SDS ($SO_4{}^{2-}$) is 96.1 g/mol and the total molecular weight is 265.4 g/mol. For ionic surfactants, the counter ion is ignored. Using Eqn. 4.3, the hydrophilicity index of SDS is calculated as:

$$HI_{SDS} = \frac{20 \times 96.1}{265.4} = 7.2 \quad (4.5)$$

For alcohol ethoxylates, the commonly used naming convention indicates the unit digits of the carbon fraction, followed by the number of ethoxy units. For example, in AE 24-7, 24 indicates the number of carbons in the chain is between 12-14 and there are 7 ethoxy units. Therefore, the average number of carbons in the hydrophobic portion is 13. The average molecular formula is $CH_3-[CH_2]_{12}-[OCH_2CH_2]_7-OH$.

The molecular weight of the hydrophilic portion of AE 24-7 ($[OCH_2CH_2]_7OH$) is 325.4 g/mol and the total molecular weight is 522.8 g/mol. Using Eqn. 4.3, the hydrophilicity index of AE 24-7 is calculated as:

$$\mathrm{HI_{AE}} = \frac{20 \times 325.4}{522.8} = 12.4 \tag{4.6}$$

Using these two values and Eqn 4.4, the HI of the surfactant composition is calculated as:

$$\mathrm{HI_C} = (0.7 \times 7.2) + (0.3 \times 12.4) = 8.8 \tag{4.7}$$

4.2.8 Quartz crystal microbalance with dissipation (QCM-D)

A QSense Analyser 4-channel QCM (Biolin Scientific, Espoo, Finland) was used with QSensor QSX 303 (Biolin Scientific) SiO_2 coated sensors. Water and surfactant formulations were moved through the tubing using an Ismatec IPC-N 4 (Cole-Parmer GmbH, Wertheim, Germany) peristaltic pump, at 250 μL/min. City water (120 mg/L $CaCO_3$) was used to flush the Teflon tubing and dilute surfactant formulations.

4.3 Broad automated washing results

Multiple screening experiments were conducted to explore a range of variables to assess which, if any, modify the action of the S3 DNase enzyme's ability to remove the model DNA stain described in Section 4.2.1. For each set of wash conditions, there were two internal replicates (two DNA stains in a wash pot) and at least three external replicates (three separate wash pots with these conditions). Each experiment design features formulations with and without enzyme to act as a control.

4.3.1 Water hardness

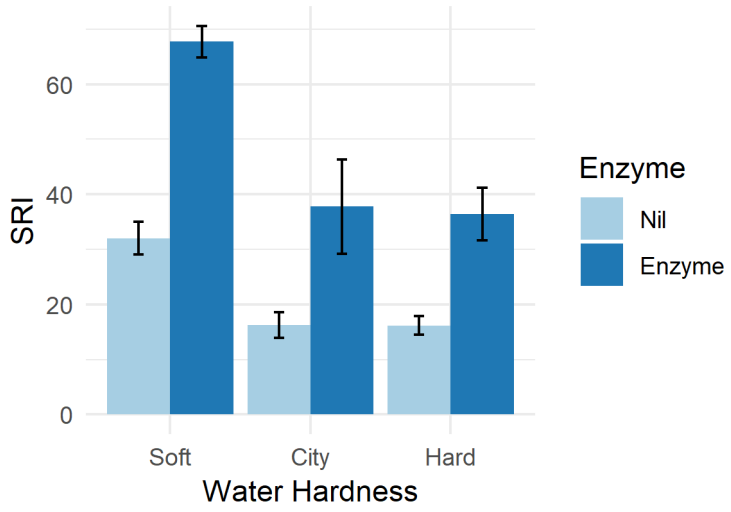

Figure 4.5: Bar chart showing the SRI values for control (nil enzyme) and enzyme containing wash cycles with varying water hardness.

As Fig. 4.5 shows, both city and hard water cycles produce similar results with large overlap of error bars for both nil and enzyme containing solutions. The soft water results show higher SRIs than the the values from solutions with greater water hardness, for both nil and enzyme containing solutions.

An increase in SRI in the nil enzyme formulations indicate that the increases in the enzyme containing formulation should be treated with caution. As seen in Section 4.2.1, calcium ions are added in the stain preparation to help bind the methyl green stain to the DNA. The lack of ions in soft water is therefore likely to cause a substantial equilibrium shift of calcium ions out of the stain and into solution. This weakens the attachment of dye to the DNA stain and gives a false-positive increase in cleaning for soft water solutions.

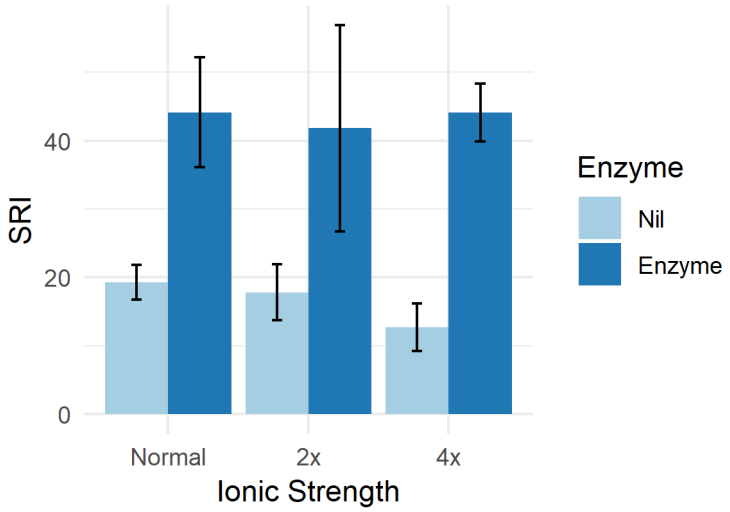

Figure 4.6: Bar chart showing the SRI values for control (nil enzyme) and enzyme containing wash cycles with varying ionic strengths of wash liquid, where the normal ionic strength of solution is 0.106 mmol/L

4.3.2 Ionic strength

As water hardness only takes into account the concentration of Ca^{2+} and Mg^{2+} ions, the ionic strength of the wash solution was investigated. Fig. 4.6 shows, there is an overlap of error bars across each of the three ionic strength levels for each of the nil and enzyme containing wash solutions. Alongside the water hardness measurements in Section 4.3.1, the concentration of ions in solution is shown to cause no change in the activity of S3 DNase.

4.3.3 Wash duration

Varying the duration of washes demonstrates that kinetics play a major role in the activity of the enzyme. Fig. 4.7 shows that a shortened 9 min wash produces no difference between a wash liquid with and without the enzyme present. In this short time period, the enzyme is unable to enhance the cleaning of the surfactants. Extending the duration to 30 min gave the highest SRI recorded across these screening experiments.

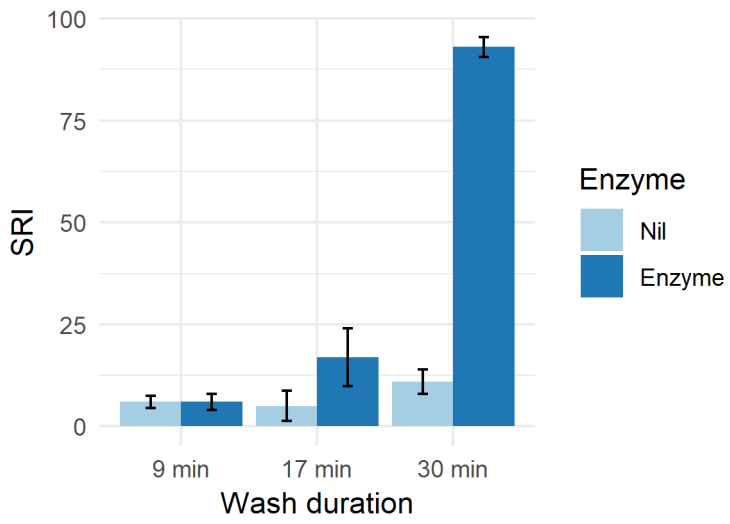

Figure 4.7: Bar chart showing the SRI values for control (nil enzyme) and enzyme containing wash cycles with varying wash durations. All wash temperatures were 25 °C.

4.3.4 Wash temperature

Varying the temperature of the wash liquid is another avenue for confirming the role of kinetics (in addition to Section 4.3.3). As seen in Fig. 4.8, the colder 15 °C conditions do not suppress the enzyme below that of the 25 °C wash. When the temperature is increased to 30 °C, a significant benefit is obtained. Referring back to Equation 4.1, all four rate constants would be increased by a rise in temperature, up until the point that the enzyme denatures.

Modifying the duration or temperature of the wash does not provide any further understanding to the mechanism of enzyme action. The increased kinetics at longer durations and higher temperatures merely increase the rate at which the enzyme acts.

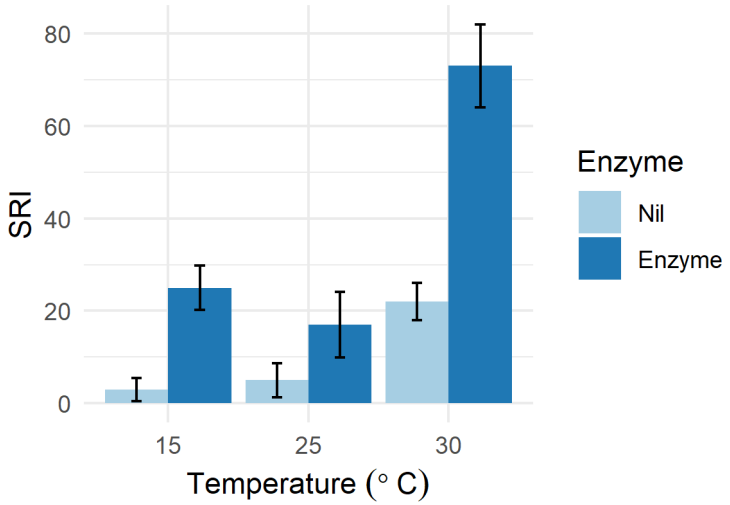

Figure 4.8: Bar chart showing the SRI values for control (nil enzyme) and enzyme containing wash cycles with varying wash temperatures. The duration of all washes was 17 min.

4.3.5 Surfactant concentration

The recommended wash concentration of P&G's Tide North American washing detergent is 1.58 mL of detergent per litre of water (57 mL detergent for a standard 36 L volume washing machine). Both the recommended concentration and a concentration of twice the intensity (3.6 mL/L) were examined. Washing at standard conditions with no S3 DNase produced an SRI of 19.4 ± 3.6. When the wash cycle is conducted with the enzyme, the SRI is raised to 40.5 ± 3.8, an addition of approximately 20 SRI units.

As seen in Fig. 4.9, when the concentration of detergent is doubled in the nil enzyme solution, the SRI increases to 42.0 ± 6.2. Experiments that contained double the recommended dose of detergent and the recommended concentration of enzyme gave an SRI of 77.9 ± 1.8. This increase of approximately 40 SRI units indicates that the surfactant level contributes to increased enzyme activity. As the surfactant concentration does not affect the rate at which an enzyme-substrate complex completes the reaction to an enzyme-product complex, this increase in activity will be seen in k_1 and k_4 in Equation 4.1.

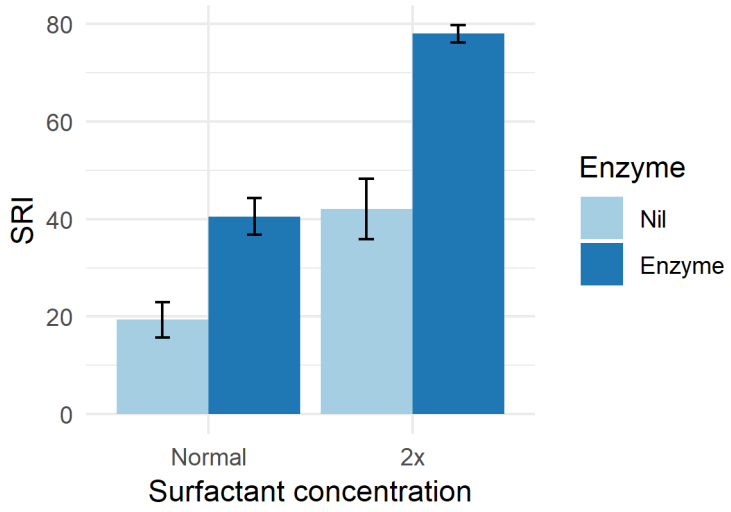

Figure 4.9: Bar chart showing the SRI values for control (nil enzyme) and enzyme containing wash cycles with varying surfactant concentrations, where the normal detergent concentration is 1.58 mL/L. Wash duration was 17 min and temperature was 25 °C.

In each wash pot, a clean polyester and cotton swatch (5cm×5cm) was labelled and recovered from the cycle. These were used to conduct enzyme-linked immunosorbent assays (ELISA) to detect the amount of enzyme protein on the surface of the fabric as described in Section 4.2.4. As the higher concentration of surfactant leads to an increase in enzyme activity (Fig. 4.9), a decrease in the amount of enzyme on the fabric at the end of the wash would be expected if the hop-on-hop-off hypothesis is valid.

As seen in Fig. 4.10, the protein more favourably attaches to the cotton fabric, rather than the polyester. This preference for cotton is seen in all ELISA experiments for S3 DNase. The wash cycle containing twice the concentration of surfactant sees decreases in protein deposition on both fabrics, but overlap of error bars makes this finding inconclusive. To eliminate experimental noise and error, the component parts of surfactant were investigated individually using a design of experiments method.

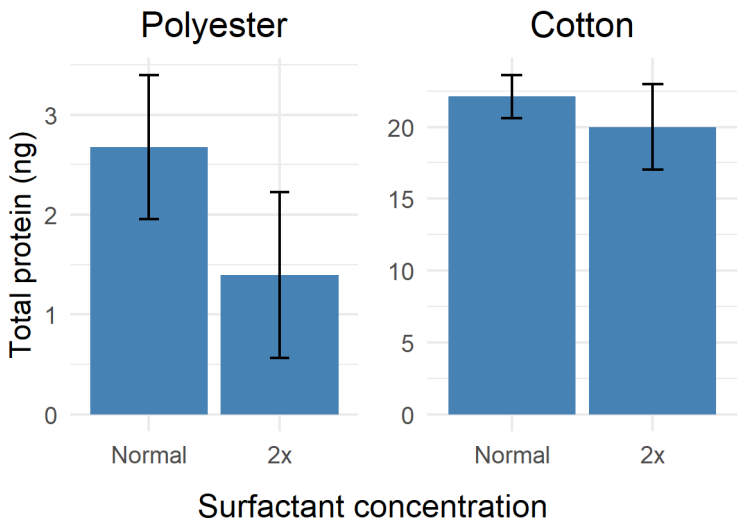

Figure 4.10: Bar chart showing the total protein values as determined by ELISA, directed against S3 DNase, on polyester and cotton tracers. Wash conditions used different concentrations of surfactant, where the normal surfactant concentration is 1.58 mL/L. Wash duration was 17 min and wash temperature was 25 °C.

4.4 Design of Experiment

From the broad variable screening experiments of Section 4.3, surfactant level was the most intriguing result. To gain a better understanding of which components of the surfactant formulation is altering enzyme activity, a design of experiment method was developed.

The surfactant formulation used in previous sections contains five major components and each of these was obtained from P&G. These constituent components were:

- LAS: linear alkylbenzene sulfonates, anionic surfactant
- AES: two different alcohol ethoxysulfates, anionic surfactant
- NI: a non-ionic surfactant
- AO: an amine oxide, non-ionic surfactant

These five surfactants and the S3 enzyme were input into the statistical analysis program, JMP. The maximum values allowed were set as the concentrations used in

Table 4.1: Maximum concentration of surfactant in wash liquid from commercial product. These values are set as the maximum allowed in the design of experiment.

Surfactant	Maximum concentration (mg/L)
LAS	442
AES (Ambrosia)	440
AES (North America)	202
Non-ionic	245
Amine oxide	47
Enzyme	0.2

the final commercial product. These values are shown in Table 4.1.

The JMP software was instructed to formulate a design with maximum, midpoint and minimum values for each component, with a maximum number of combinations of 40. It is advantageous to have as many combinations as possible, but this comes at the cost of consumables and time. The DoX provides the highest amount of understanding from the fewest combinations.

The software calculates the required combinations and randomises the order that these cycles are conducted. It is recommended practice to run the experiments in the order that the software specifies, which may not be the most straightforward for the experimenter. For example, the concentration of the surfactants will not gradually rise through the experiment run, as this may cause a residual effects in the wash pots. The random order allows non-experimental variability to be identified in the analysis stage. The first ten experimental combinations are shown in Table 4.2.

The experimental combinations required by JMP were completed, according to methods described in Section 4.2.2. The SRI values were reported back to the software so a model of the variables could be computed. Polyester and cotton swatches were also recovered from each combination that contains enzyme, to be analysed via ELISA.

Table 4.2: The first 10 experiment combinations generated by JMP software, showing the required concentration of each component in mg/L. These experiments are run and the SRI reported back into the software for it to be modelled. All wash durations were 17 min, with a temperature of 25 °C.

Exp.	LAS	NI	AO	Ambrosia AES	N. America AES	Enzyme	SRI
1	442	0	47	440	0	0	.
2	442	122.5	23.5	0	101	0	.
3	221	245	23.5	220	101	0.1	.
4	221	122.5	47	220	202	0.2	.
5	0	122.5	0	0	0	0.2	.
6	442	0	0	0	0	0	.
7	0	0	0	440	0	0.2	.
8	0	122.5	47	0	101	0.1	.
9	442	245	0	440	202	0	.
10	442	0	47	440	202	0.2	.

4.4.1 Design of Experiment model

By providing the statistical software with the SRI values that are produced by the various surfactant and enzyme combinations, it can compute a model of how these variables interact. The model suggested that the most important variable to the removal of DNA stains was the concentration of S3 DNase. Although this is not a striking finding, it provides assurance that the model is identifying variables correctly, without any prior knowledge of their chemistries.

When the model is instructed to hold the concentration of enzyme at 0.2 mg/L, two interactions become important, the relationship of LAS to NI surfactant and the relationship of Ambrosia AES to amine oxide. Both of these relationships are ratios between an anionic and non-ionic surfactant. Due to this finding, the association of the anionic:non-ionic ratio and the hydrophilicity index to the SRI of the formulations were examined.

As Fig. 4.11 shows, there is a reasonable spread of data across different anionic:non-

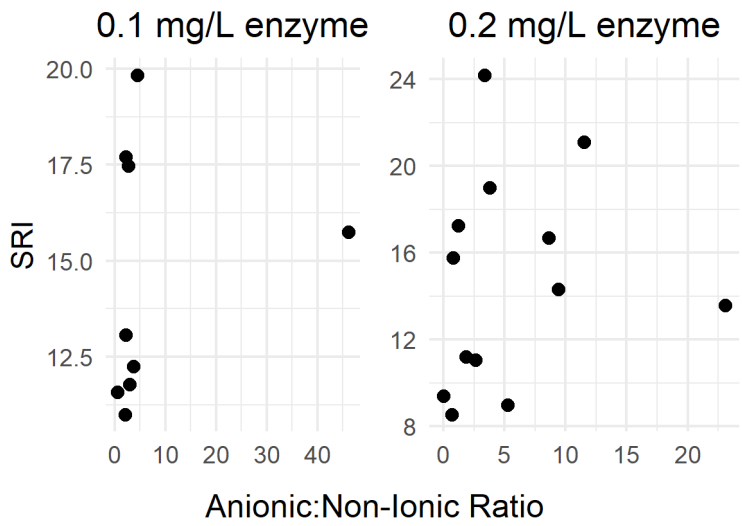

Figure 4.11: Scatter plots showing the relationship between SRI and the anionic:non-ionic ratio of the surfactant formulations for two different enzyme concentrations.

ionic ratios for the 0.2 mg/L enzyme concentration and no obvious correlation. For the lower enzyme concentration of 0.1 mg/L, eight of the nine data points are below a ratio of 5, as the ratio was not part of the original experiment design.

Fig. 4.12 shows that when the hydrophilicity index (HI) of the surfactant formulations was inspected, there was a slight trend that could be observed. These results indicate a peak value of SRI when the HI is between 8.5 and 10, with a decrease in achieved SRI either side of this range. The effects of different surfactant ratios against enzyme activity have been widely studied and shown to give both positive and negative changes depending on the specific formulation.[140–142]

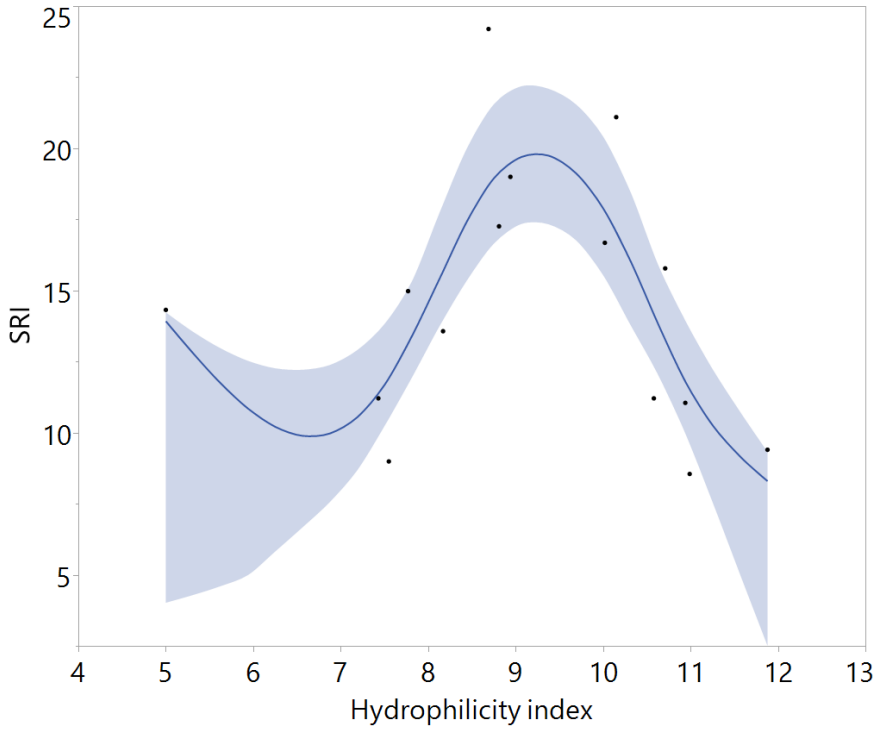

Figure 4.12: Scatter plot showing the relationship between SRI and the hydrophilicity index of the surfactant formulations. Confidence interval shown is set at 95%.

4.4.2 ELISA findings

When the amount of enzyme protein deposited on the fabric swatches at the end of the wash cycle is examined, peak values were evident as with the hydrophilicity index in the previous section. As can be seen in Fig. 4.13, the highest SRI results came with high adsorption of enzyme to the cotton fabric, but a specific value of deposition on the polyester. This is seen in greater detail in Fig. 4.14.

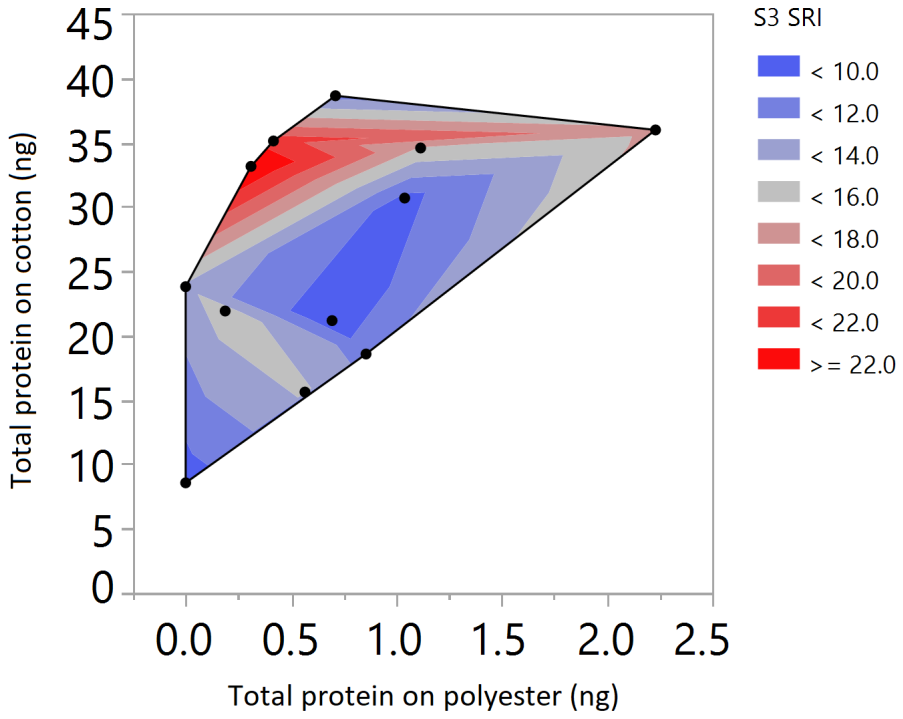

Figure 4.13: Contour plot of total protein readings on polyester and cotton swatches with the corresponding SRI values. The enzyme concentration level for these data is 0.2 mg/L.

If the proposed hopping mechanism of enzyme action is valid, it would be expected that the highest SRI is observed when the enzyme deposition is neither at an extreme minimum or maximum value, but at an intermediate level. The ELISA readings give the deposition level at the end of the cycle. A low absorbance value suggests the enzyme is unable to approach the surface easily, whereas a higher value suggests it is remaining on the substrate.

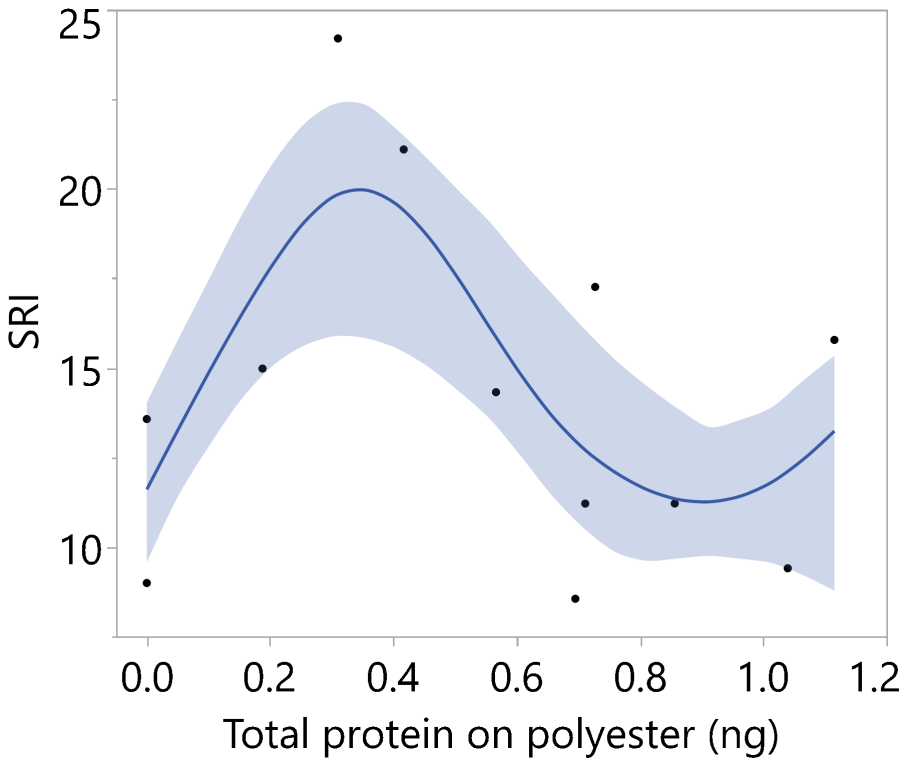

Figure 4.14: Scatter plot of SRI against total protein readings on polyester swatches for 0.2 mg/L enzyme concentration.

This behaviour is observed on polyester with a maximum SRI achieved when the total protein found on the swatch is around a value of 0.3 ng. Despite the use of the maximum concentration of enzyme (0.2 mg/L), there were two formulations that recorded no deposition at the end of the cycle. There are also numerous formulations that encouraged higher deposition to the polyester substrate. All of these resulted in lower SRI values than of those around 0.3 ng.

This intermediate deposition behaviour is not observed for cotton swatches. Here, the data suggest that to achieve the highest SRI, the deposition of enzyme on polyester should be around 0.3 ng and the deposition on cotton should be maximised. This is reasonable due to the different hydrophobicities of the two fabrics. Cotton (cellulose) is more hydrophilic than polyester (poly(ethylene terephthalate)). Cotton swatches can absorb ten times their mass in water,[143] so are a good indicator

of how much enzyme is in solution for a specific formulation. Surfactant combinations that lead to a low final adsorption on cotton may result in more favourable deposition on the walls of the wash pot and therefore inaction of the enzyme on the DNA target.

4.5 QCM-D analysis

To verify the model produced by JMP and further investigate the effect of the anionic:non-ionic ratio and hydrophilicity index (HI), experiments were conducted on a quartz crystal microbalance with dissipation monitoring (QCM-D). Three formulations were prepared that had equal amounts of surfactant, but with different HI values and predicted SRI values from the model (Table 4.5).

The QCM provides the resonant frequency of 11 overtones of a quartz crystal. As material deposits on or detaches from the surface of the quartz sensor, this frequency will be affected. Additional mass dampens the frequency, whereas material leaving the surface allows the frequency to increase back towards its natural value. By observing the deposition and release behaviour of different surfactant formulations with enzyme, the model computed by JMP can be verified or rejected. The mechanism of enzyme action being a hopping or scooting mechanism (see Fig. 4.1) can also be detected, by analysing the removal of mass between the high and low performance formulations.[132,136]

The intention was to use 0.2 mg/L of enzyme in these QCM-D experiments, but initial tests were unable to detect concentrations at this level. Various trials were conducted before deciding to increase the enzyme concentration to 200 mg/L. This much higher concentration would allow any small variation in the enzyme deposition and release to be clearly seen through noise in the data. Concentrations of 20 mg/L and 100 mg/L both resulted in frequency reductions of less than 5 Hz, which was considered to be too small a range to observe the changes.

Table 4.3: The surfactant concentrations, HI, anionic:non-ionic ratio and predicted SRI for three formulations. These values were extracted from the statistical model constructed by JMP. All formulations were tested at 25 °C.

	Performance		
	Strong	**Medium**	**Weak**
LAS (mg/L)	442	175	800
NI (mg/L)	245	779	8
AES (mg/L)	442	175	321
Total surfactant (mg/L)	1129	1129	1129
HI	8.7	10.6	6.6
Anionic:non-ionic ratio	3.6:1	0.4:1	140:1
Predicted SRI	26	15	5

Fig. 4.15 gives strong evidence to support the hopping hypothesis of the S3 DNase enzyme mechanism. All sensors were run in parallel and began with 500 s of city water passing over each sensor. At 500 s, the formulations described in Table 4.5 with 200 mg/L enzyme reach the cell containing the sensor and begin depositing. The formulation that is modelled to have the highest performance against DNA stains on polyester reaches a maximum adsorption to the surface in approximately 300 s. The weak performance formulation also achieves a frequency decrease of 20 Hz, but requires 800 s.

The deposition achieved by the medium performance formulation is lower than both the high and low performance solutions (16 Hz vs 20 Hz). However, the maximum deposition is achieved rapidly and in approximately the same time period of the high performance formulation. With reference to Equation 4.1, k_1 for the high and medium performance formulations are similar, but the reverse rate constant for the medium performance formulation is greater than that of the high performance. This leads to the observed lower initial adsorption and the loss of mass between 800 and 1700 s. k_1 for the weak performance formulation is found to be slightly lower than for medium and strong performance (with a reverse rate constant similar to that of the high performance).

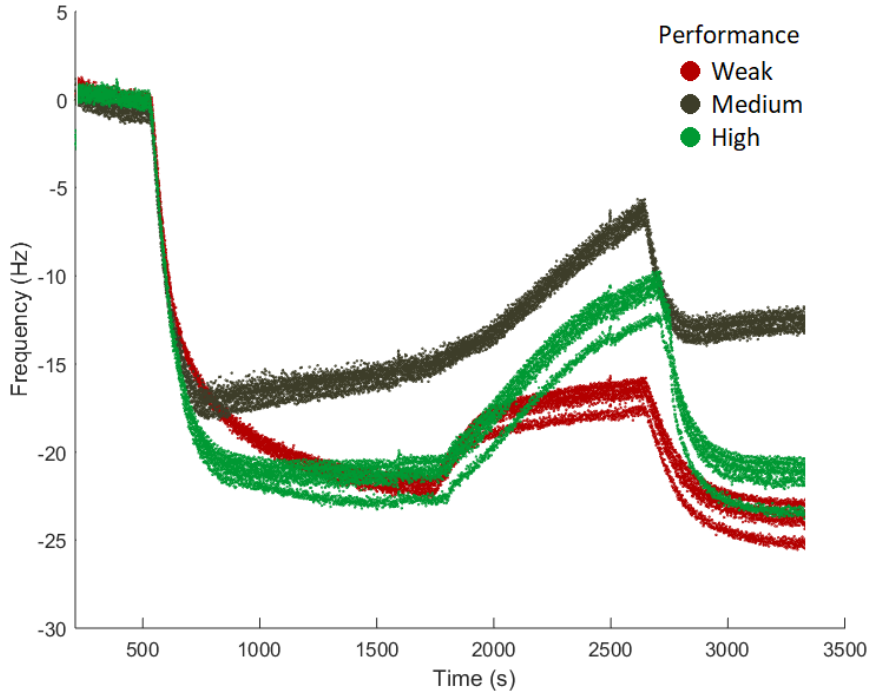

Figure 4.15: QCM-D frequency changes against time for the three formulations proposed using the statistical model. The third, fifth, seventh and ninth overtones of each sensor are displayed.

At 1700 s, fresh city water began to pass over each sensor, causing the formulations to detach from the surface. Both the high and weak performance formulations initially release at a similar rate of 1 Hz/min, but the weak performance formulation slows in rate after only 200 s. The fresh city water is only able to displace 4 Hz equivalent of material from the weak performance formulation in the time that the high performance formulation loses a 10 Hz equivalent of mass. The rate of removal in the high performance formulation eventually slows to approximately 0.7 Hz/min. Due to the lack of DNA in this QCM-D experiment, a direct measurement of k_4 (Eqn. 4.1) is not possible as there is no route to produce product (P) from the substrate. However, the predicted SRI of each formulation is directly linked to the hydrolisation of phosphodiester bonds, the generation of product. Therefore, these QCM-D data can indicate the changes in k_4 by examining the different rates

of removal of mass from the sensor.

The high performance formulation enables quick access to the surface to form a steady mass and also promotes a quick return to solution when fresh water enters the system. The weak formulation is slightly less effective at gaining the same level of deposition on the surface, but more importantly, prevents the departure of the formulation. The suppression of k_4 is responsible for the limited enzyme activity and poor SRI in the low performance formulation. This finding indicates the validity of the hopping mechanism, rather than a scooting mechanism (see Fig. 4.1), for this enzyme.[132,144]

Compared to the high performance formulation, the medium performance formulation is less able to promote access to the surface, as well as being less able to maintain a steady mass on the substrate. The introduction of fresh city water causes an increase in the removal of material to a rate of approximately 0.7 Hz/min. The removal rate becomes equal to that of the high performance formulation at 2500 s, after initially being slower. The medium performance formulation promotes less access to the surface than the weak formulation, but importantly does not keep the enzyme and its co-surfactants at the surface. It is these properties that allow the formulation to generate a reasonable SRI result.

As depicted in Fig. 4.16, these QCM-D data show that the major factors in a high SRI result is a formulation that allows easy access both towards and away from the substrate (high k_1 and k_4, Eqn. 4.1). Lower SRI values are obtained if the enzyme is restricted from getting to the surface (medium performance) or remains bound to the surface (low performance). The enzyme produces the highest SRI when it is easily able to move both onto and off of the substrate, providing a large justification for the hopping mechanism.

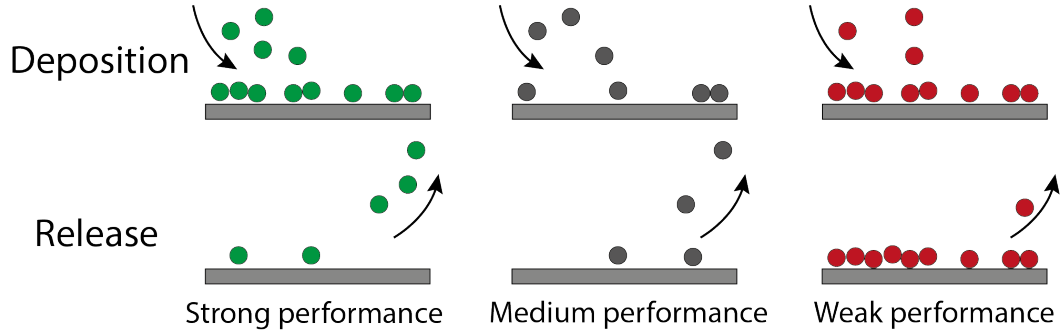

Figure 4.16: Schematic diagram of the different deposition and release behaviours of the designed formulations. Strong performance allows rapid deposition and release. Medium performance allows moderate deposition and rapid release. Weak performance allows rapid deposition, but poor release.

4.6 Conclusions

Using automated washing equipment and a model DNA stain, various conditions were screened for their effect on the activity on S3 DNase (Section 4.3). Water hardness and ionic strength were discounted as variables that have a role in the mechanism. Wash duration and temperature showed that increased kinetics aided in the enzyme's activity, but this finding does not add to the understanding of the mechanism of action. The concentration of surfactant was identified as a variable that increased enzyme activity and may lead to better understanding of the mechanism.[140]

A design of experiment procedure was developed to analyse the constituent components of the commercial surfactant mixture. These individual components were efficiently screened using the same automated washing equipment, with the results input into the statistical software, JMP. Cotton and polyester swatches were recovered from each combination of surfactants and the protein deposition at the end of the wash determined using ELISA.

ELISA results indicated that the highest enzyme activity was achieved when deposition on polyester was neither at a maximum or minimum value. The highest SRI results also coincided with maximum deposition rates on cotton, which is concluded

to be a result of a high concentration of enzyme remaining available in the solution.

The statistical software produced a model that enabled identification of hydrophilicity index (HI) as a potential driving factor in enzyme activity. The highest activity was achieved when the HI value of the formulation was approximately 9. To confirm the model and investigate the role of HI on enzyme activity, QCM-D was used. Three formulations were designed that, according to the model, produce high, medium and weak performance from the enzyme. These were observed on a QCM-D to understand the deposition and release behaviour of the surfactants and enzyme.

The QCM-D results validate the computer model and the proposed hopping mechanism. The highest enzyme activity is achieved when the formulation has rapid access to and from the substrate (high values of k_1 and k_4 in Eqn. 4.1). The formulation that produces low activity traps the components on the surface, whereas the medium performance formulation does not facilitate the initial access to the substrate as effectively as the high performance design. However, the medium formulation does enable rapid departure from the substrate back into solution, which results in reasonable enzyme activity.

Chapter 5

Scanning Force Microscopy investigation of pathogen adhesion events

As seen in Chapter 3, atomic force microscopy (AFM) can give detailed information about how the nature of adhesion to a substrate changes as the bioprobe is altered by the addition of enzymes. The World Health Organisation predicts that if effective interventions are not made against antimicrobial resistance, it will be responsible for 10 million deaths annually by 2050, higher than the current mortality rate of cancer.[145] By gaining additional understanding of the mechanisms that enable biofilms to function, the threats that they pose can be combated in new ways.

Atomic force microscopy can be used to answer other medically relevant questions about pathogenic adhesion that other techniques are unable to resolve. The investigation of a new treatment to reduce the adhesion of *Staphylococcus aureus* (*S. aureus)* to human skin cells was one of two collaborative side projects that presented themselves during the course of this thesis. This collaboration was able to take advantage of the extensive work in researching bioprobes on AFM cantilevers detailed in Chapters 2 and 3 to rapidly collect adhesion data to complement their study. The other project was the investigation of how the single cell parasite, *Leishmania*,

attaches to the midgut of the sand fly, which may lead to a method of preventing the spread of the tropical disease, leishmaniasis. This collaboration benefited from the MATLAB software (Chapter 3 and Appendix A) written to rapidly analyse AFM curves in a way that was not possible in the native software. Exposing the software to a different dataset allowed for greater refinement of the code and aided in making the future use by collaborators a more flexible and straight forward process, rather than a rigid piece of code that is only able to interact with data in a very set structure. Archived data was reanalysed using the new software, with the fresh insights detailed in this chapter.

Both leishmaniasis and infection by *S. aureus* (specifically methicillin resistant *S. aureus* (MRSA)) present serious issues due to the ineffectiveness of a wide range of drugs and treatments.[82,146] With a similar motivation to studying the adhesion of biofilms to circumvent the resistance bestowed by the extracellular matrix, AFM adhesion measurements can increase understanding of the major vectors of transmission and infection of MRSA and leishmaniasis. With the target of new treatments being external to the cells in question, the ability of the cell to gain resistance is greatly decreased, making the treatment more valuable to the fight against these pathogens.

5.1 Molecular mapping of sand fly gut adhesins on the surface of the human protozoan pathogen *Leishmania mexicana* through scanning force microscopy

Leishmaniasis is a tropical disease that affects the skin, liver or spleen. It is caused by protozoan *Leishmania* parasites and are transmitted from the bites of female sand flies.[147] With approximately 40,000 deaths annually, leishmaniasis has the second largest death toll of parasitic diseases, second only to malaria.[84,148]

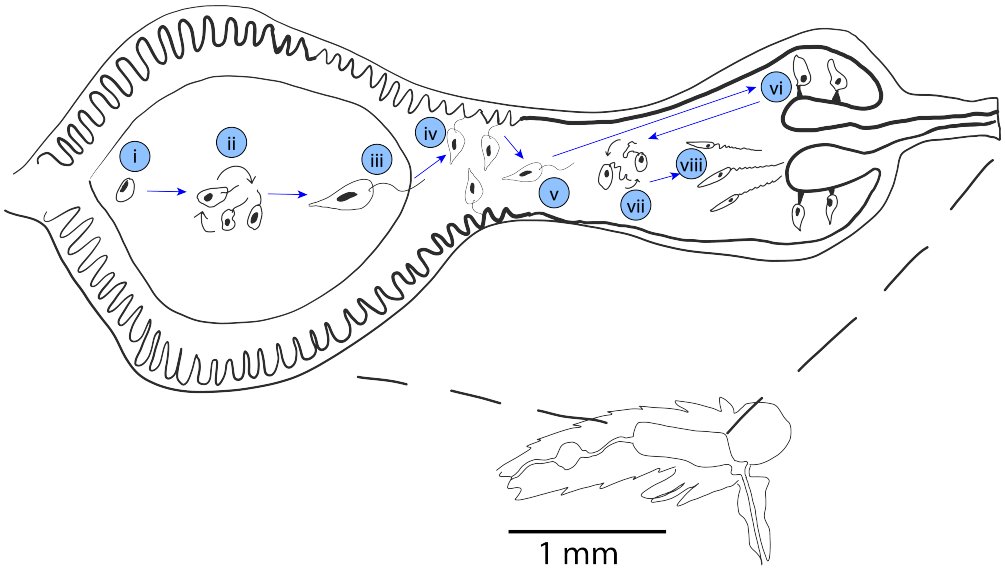

Figure 5.1: Schematic diagram of a sand fly midgut. (i) amastigotes from blood of infected host; (ii) procyclic promastigotes multiply in the digested bloodmeal; (iii) nectomonad promastigotes migrate through the peritophic matrix before the bloodmeal is defecated; (iv) nectomonads attach to the microvilli of the midgut to resist expulsion by defecation, then detach and resume their forward migration (v); (vi) Haptomonad promastigotes attach to the stomodeal valve by modifying their flagellum; (vii) leptomonads multiply, secrete phosphoglycans and differentiate into the mammal-infective metacylic promastigotes (viii), which are transmitted into skin when the sand fly takes another bloodmeal. Not to scale. Inset is a cross-section through a female sand fly showing the midgut which is expanded. The scale bar is 1 mm.

There are few effective drugs against leishmaniasis and many are toxic. The over reliance on those that do exist has lead to a global increase in drug resistance.[146] Therefore, there is a need for a greater understanding of the mechanism of these parasites to identify targets for new treatments and drugs.[149]

Here, a molecule of interest is the use of surface glycoconjugates by *Leishmania* to anchor themselves to the midgut of the sand fly.[85] This attachment allows *Leishmania* to develop by resisting expulsion from the sand fly when it defecates, allowing it to persist beyond the initial bloodmeal phase of infection (Fig. 5.1). If this phase of development can be disrupted by modification of adhesion factors, it may lead to a new method of blocking transmission.

When colonizing the sand fly, *Leishmania* undergo morphological changes between life stages. Nectomonad promastigotes can adhere to the sand fly midgut to mature, whereas metacyclic promastigotes that are infective to mammals populate in the anterior midgut of the sand fly, ready to be transmitted.

Leishmania use lipophosphoglycan (LPG) on their surface to attach to the sand fly midgut. LPG is an oligosaccharide containing a glycophosphatidylinositol (GPI) anchor, a conserved backbone of phosphorylated galactose-mannose disaccharide repeat units and an oligosaccharide cap. Modification of the LPG occurs during the life cycle of *Leishmania*, resulting in elongation and for some species, substitution of side chains.[150] These changes to the side chains mask groups involved in attachment, allowing the metacyclic promastigotes to be free within the lumen of the sand fly gut and ready for transmission when the sand fly bites.

A galectin (a β-galactoside binding lectin, see Fig. 5.2) has been identified in the midgut of *Phlebotomus papatasi* as mediating the attachment of galactose residues found in the LPG of *L. major*.[151] By coating an AFM tip with galactose, the surface of various *L. mexicana* promastigotes were mapped for adhesive interactions to understand the molecular interactions used by *Leishmania* parasites to colonize their sand fly vector.

Galactose-coated tips had been produced and used to map adhesive events across various *L. mexicana* promastigotes in previous work by a collaborator.[81] The contributions listed in this thesis are additional data processing of force-distance curves using a custom MATLAB script, as well as control measurements involving an AFM tip modified by an anti-LPG antibody against the same *L. mexicana* promastigotes.

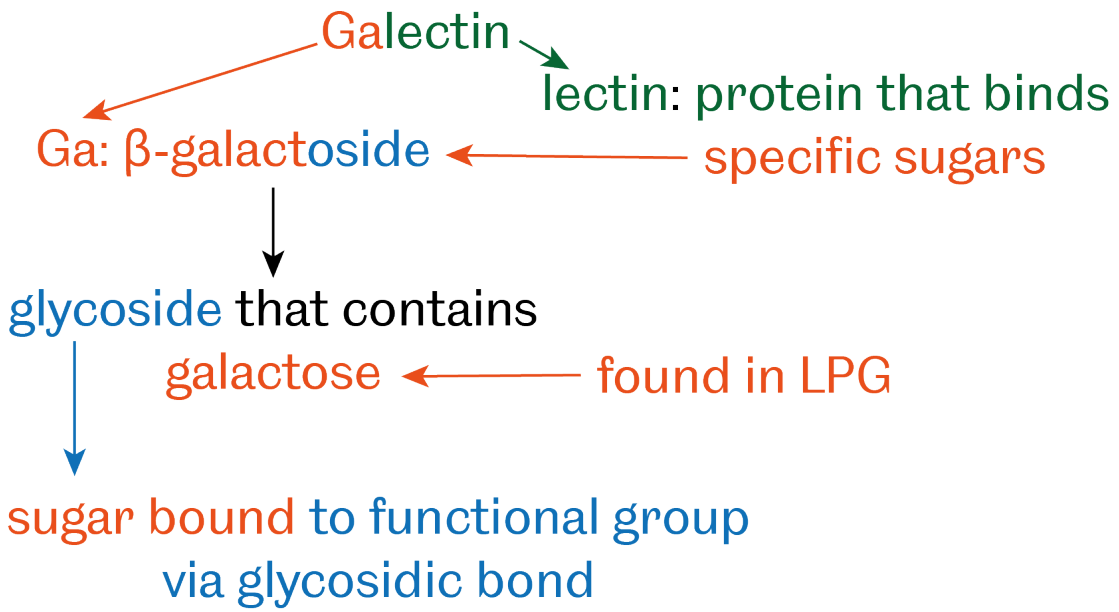

Figure 5.2: Biological nomenclature of galectin, a protein that specifically binds to structures containing galactose, which is found in LPG.

5.1.1 Experimental methods

Galactose tips

Although force measurements with galactose modified tips were not conducted in this thesis, the method for production is included for reference.

Polymethacrylic acid (PMMA) brushes were synthsized on AFM cantilevers (MLCT, Bruker AFM Probes, USA) as previously described.[152] After 20 min of polymerization (producing brushes between 8–15 nm thick as measured by ellipsometry in ambient conditions), the PMAA-coated cantilevers were stored in foil-wrapped glass Petri dishes for up to one month before use. PMAA brushes were converted to poly(*N*-2-(β-D-galactosyloxy(ehtyl acrylamide))) (p(NβGalEAM)) glycopolymers by immersing the coated cantilevers in a solution of equal parts 0.1 M *N*-(3-dimethylaminopropyl)-*N*-ethylcarbodiimide hydrochloride (EDC) and 0.2 M *N*-hydroxysuccinimide (NHS) in deionized (DI) water. After 2 h, the cantilevers were rinsed with DI water and dried under a gentle nitrogen gas flow. 150 µL of a 10 mg/mL solution of 2-aminoethyl-β-D-galactopyranoside[153] was carefully added to each cantilever and left overnight before rinsing with DI water and drying under a

gentle nitrogen gas flow. Both of these steps were undertaken at room temperature in 5 cm polystyrene Petri dishes.

Anti-LPG tips

Leishmania LPG antibody (CA7AE) was obtained from Bio-Rad (Watford, United Kingdom). The received antibody was stored in multiple aliquots of 2.5 mg/mL in 0.5 mL of DI water and frozen until use. MLCT (Bruker, USA) cantilevers were cleaned in Piranha solution (H_2SO_4:H_2O_2, 1:1, 97%:30%) [DANGER: Piranha solution is strongly oxidising, hydrogen peroxide should be added dropwise to hydrochloric acid, never in reverse, slowly] for 20 min before being rinsed in DI water. The cantilevers were then immersed in 10 mL of 1% (3-aminopropyl)triethoxysilane (APTES) in toluene for 2 h. This was followed by immersing the cantilevers in 2.5% glutaraldehyde in phosphate-buffered saline (PBS) for 1 h, washing in PBS and storing in PBS overnight at 4 °C. On the day of the experiments, a frozen aliquot of antibody was thawed and 500 µL of PBS was added to adjust the concentration to 1.25 mg/mL. The cantilevers were incubated in this solution for 2 h and rinsed gently in PBS before use in force measurements.

Glass slides for parasites

Glass slides were cleaned by sonication in acetone, ethanol and DI water sequentially, dried under nitrogen and stored in covered polystyrene Petri dishes. On the day of experiments, a fresh solution of poly(ethylenimine) (PEI) (0.2 w/v) in DI water was added dropwise to the centre of the cleaned glass slides and left for 1.5 h. Parasites were thawed and extensively washed in PBS via centrifugation and 100 µL of this solution was added to the PEI coated slides and left for 1.5 h.

5.1.2 MATLAB data analysis

The original work exploring the adhesive properties of *L. mexicana* parasites analysed the peak adhesive interaction between the cells and a galactose-coated AFM tip.[81] The custom MATLAB script presented in this thesis was able to quickly and

accurately extract the secondary peaks of each force-distance curve from this original data. This data analysis would not be possible without the MATLAB script as the AFM software requires time consuming manual inspection of each force-distance curve to identify and extract the coordinates of secondary peaks. With the thousands of force-distance curves collected in the original work, this manual task was prohibitively time intensive to consider.

The aims of data analysis made possible by processing in MATLAB were:

1. Compare the number of force events per force-distance curve for different life stages of the parasite
2. Allow a calculation of an average number of events per force-distance curve
3. Examine the relationship between extension and adhesion values

The threshold for what would be indexed as a valid force event had to be defined and inserted into the MATLAB script. It was decided that events should be preceded by a reasonably clear, continuous extension and that the size of the event should be greater than 30 pN (as the noise in the curves is generally 15–20 pN).

To achieve these conditions, the script was designed to identify all peaks and troughs in the retraction curve. The script then moves through the curve with increasing values of extension, comparing the difference between a peak and a trough. Various checks are undertaken to examine if a peak or trough should be retained or removed based on the proximity to others in the x axis and the size of the event across the y axis. Once the entire curve has been examined, the only identified troughs remaining should be at valid events that agree with those that would be picked out manually, as shown in an example curve in Fig 5.3.

5.1.3 Antibody experiments

A monoclonal antibody (CA7AE), which recognizes the phosphorylated galactose-mannose (Gal-Man) repeat units of the LPG backbone, was attached to an AFM tip,

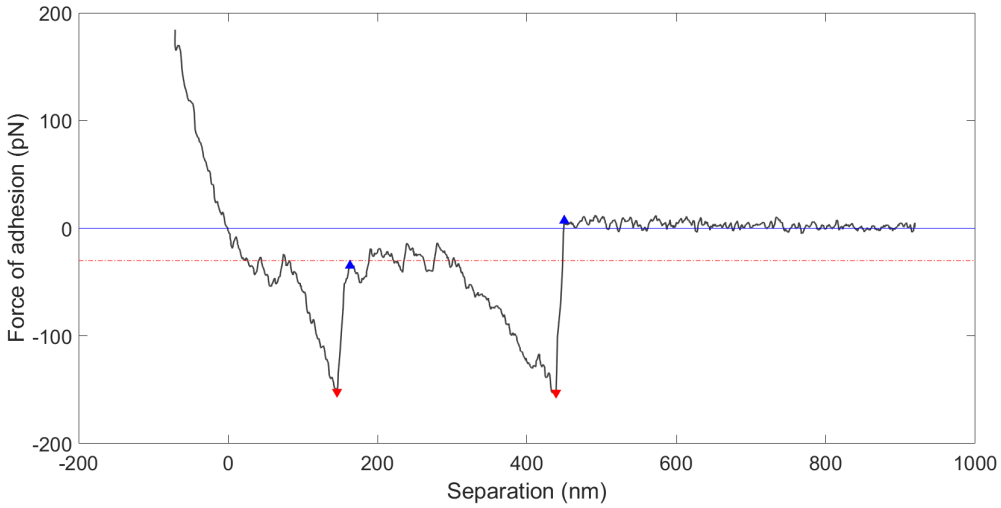

Figure 5.3: A single retraction curve of the interaction between a galactose coated AFM tip and a *L. mexicana* parasite that has been examined using the MATLAB script. The identified troughs are marked with a red downwards arrow and their corresponding peaks with a blue upwards arrow. The blue horizontal line is at a value of 0 pN and the red dashed line is 30 pN below for reference of what size of peak is admissible.

as described in Section 5.1.1. These modified tips were used to investigate the binding to nectomonad and metacyclic promastigotes in experiments that mimic those in Section 5.1.4. In addition to these experiments, mutant parasites which were deficient in LPG ($lpg^{-/-}$) (lacking the *LPG1* gene) and those with LPG production added back ($lpg^{-/-} + lpg1$) were examined. The addback line is generated by stable transfection of an episomal copy of the *LPG1* gene into a mutant parasite, to restore its LPG synthesis capability. The purpose of these experiments was to confirm that AFM is able to detect the binding events of LPG on *Leishmania* promastigotes and compare these to the galactose measurements conducted and analysed in the previous section.

Fig. 5.4 shows that the anti-LPG coated tip can detect the LPG on the surface of the promastigotes and that there is a clear difference between wild types with normal LPG production and the mutant forms ($lpg^{-/-}$) that are deficient in LPG. Interactions with the mutants are restricted to less than 200 nm extension and are

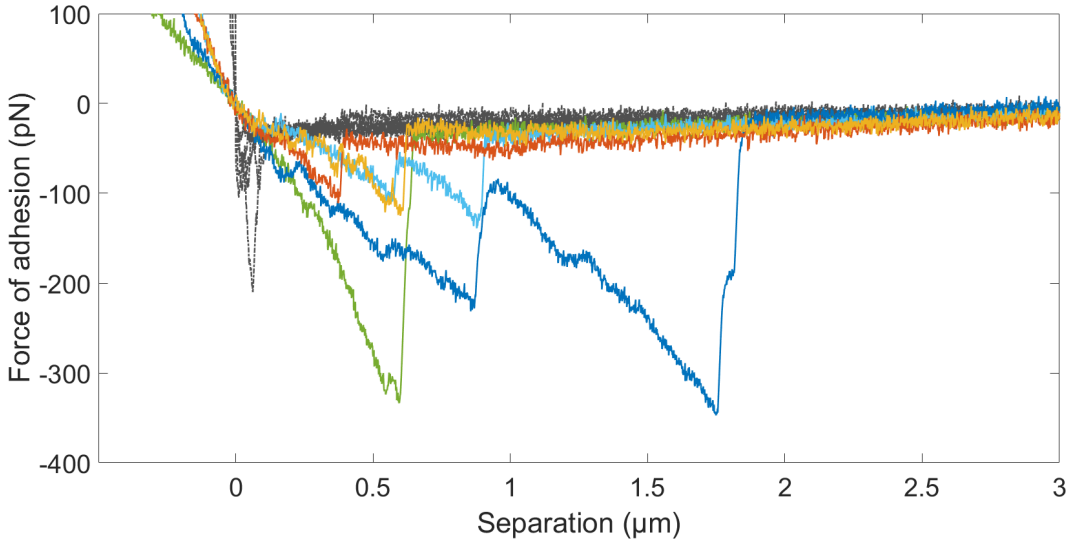

Figure 5.4: Five random force-distance curves each of mutant nectomonad promastigotes lacking LPG (grey dotted lines) and wild type nectomonad promastigotes (solid coloured lines) interacting with an anti-LPG coated AFM tip.

likely to be entirely non-specific interactions. The interactions with wild-type promastigotes also contain non-specific events due to some denaturing of the antibody on the AFM tip. However, the specific interactions between LPG and its antibody are clearly observed over a range of greater extensions, with clear force events being recorded.

Both nectomonad and metacyclic promastigotes showed interactions with the anti-LPG coated tip, with many events occurring over a long range of extensions, as seen in Fig. 5.5. Both life stages record a large number of interactions below 1.2 μm (58% for metacyclic and 83% for nectomonad promastigotes). There is a second peak in the distribution of metacyclic interactions between 1.4–2.2 μm that is also accompanied by a small number of interactions with nectomonad promastigotes. This is likely to be evidence of the extension of LPG in the metacylic life stage.[150]

As seen in Fig. 5.6, in terms of the forces of adhesion measured between the anti-LPG antibody and the surfaces of the promastigotes, metacyclics featured fewer force-distance curves with no interaction (44% for metacylics vs 66% for nectomon-

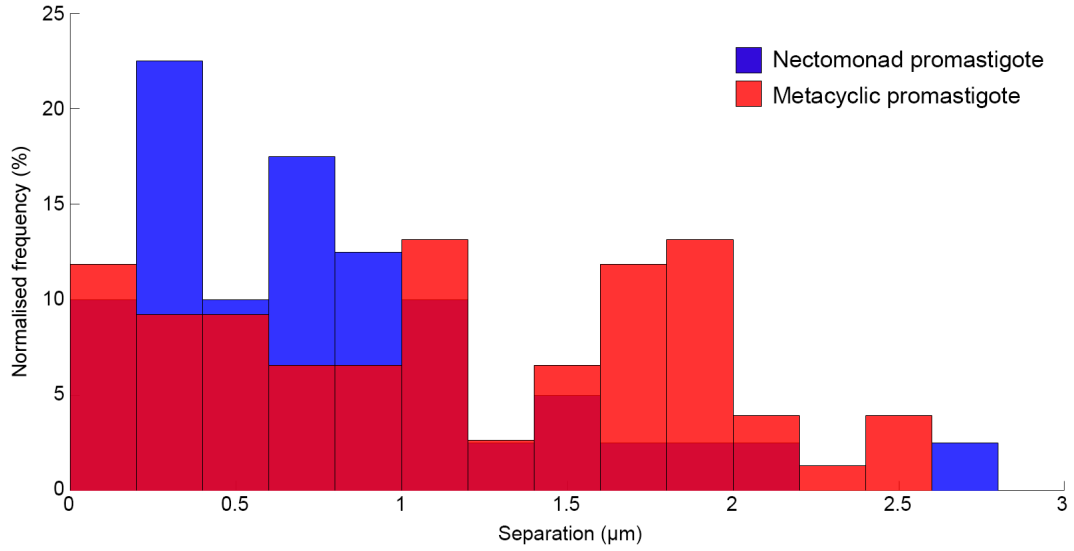

Figure 5.5: Normalized frequency histogram of extensions at which all force events are measured for nectomonad (blue) and metacyclic (red) promastigotes with an anti-LPG coated AFM cantilever tip.

ads). Interactions with metacylics also registered higher binding values compared to nectomonad promastigotes (177 ± 14 pN for metacyclics, 73 ± 12 pN for nectomonads).

5.1.4 Data analysis results

Using this MATLAB script, interactions between galactose coated AFM tips and promastigotes in different stages of the life cycle of *L. mexicana* were examined and the number of events, extension at which the events occur and force value of all events were catalogued.

Fig. 5.7 shows that there is a large range in the scale of adhesive events of galactose coated tips with nectomonad and metacylic promastigotes. There is a clear difference in the percentage of interactions that fall below the 30 pN threshold set between the two stages of the *L. mexicana*. For the later stage metacyclic promastigote, 70% of force curves have no events above the threshold value of 30 pN,

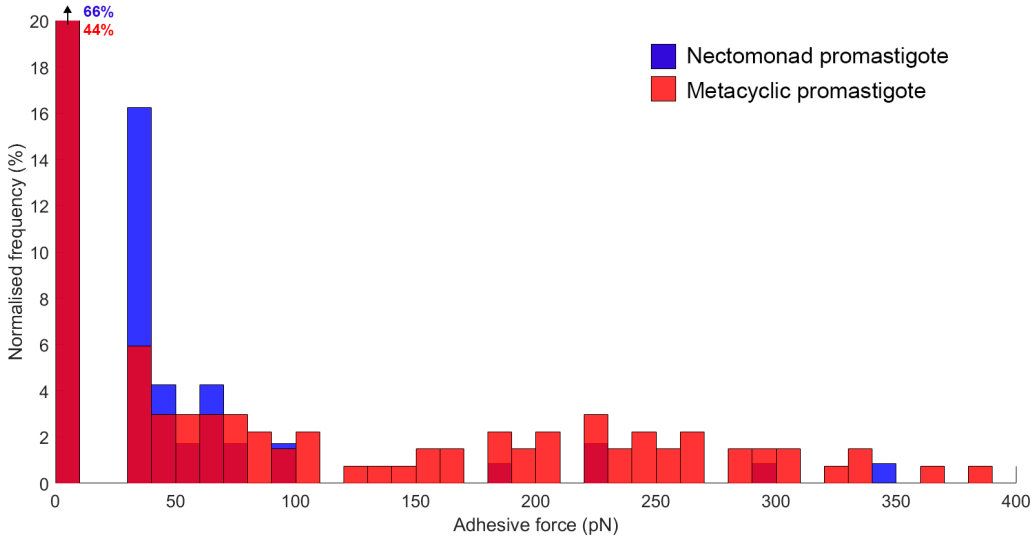

Figure 5.6: Normalized frequency histogram of force values measured for nectomonad (blue) and metacyclic (red) promastigotes with an anti-LPG coated AFM cantilever tip.

compared to 35% of the earlier stage nectomonad. For events that are greater than the threshold value, the early stage nectomonad promastigotes also achieve higher force bindings than the later stage metacyclic. In the metacyclic stage, *Leishmania* have detached from the sand fly vector and are ready to be transmitted when the sand fly bites a mammal. The high proportion of interactions with no events above the threshold value, and the weaker interactions that are above the threshold, corresponds to this observation in nature. The average force across all nectomonad promastigote parasites was 64 ± 5 pN and was 42 ± 3 pN for metacyclic promastigotes.

This clear difference in the average adhesion of the two stages is also seen in the number of binding events that are made when the galactose coated tip contacts a nectomonad or metacylic promastigote, as seen in Fig. 5.8. Metacyclic promastigotes have, on average, almost twice the number of force curves with no adhesive events passing the threshold value compared to nectomonad promastigotes (39 ± 5% and 75 ± 5% respectively). In addition to this, as seen in Fig. 5.8, multiple binding events were more frequent between a galactose tip and a nectomonad promastigote compared to a metacyclic promastigote (over four times more frequent

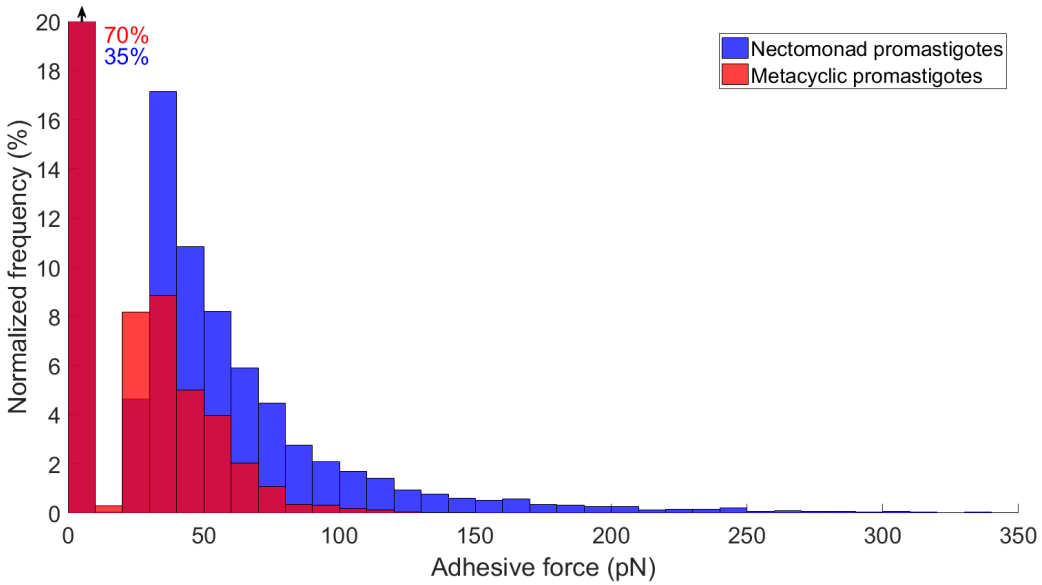

Figure 5.7: Normalized frequency histogram of all force events measured for nectomonad (blue) and metacyclic (red) promastigotes with a galactose coated AFM cantilever tip.

for two or more events and over ten times more frequent for three or more events per curve). The average number of events in a nectomonad force-distance curve is 0.8 ± 0.1 compared to 0.3 ± 0.1 per curve belonging to a metacylic.

When exploring the extension at which these different binding events take place, there is little difference between the two stages of *Leishmania*, as seen in Fig. 5.9. Metacyclics show a peak extension value between 25–50 nm, with nectomonads recording its second largest frequency of values in this range, with the most populated range immediately adjacent, between 50–75 nm. Both stages of the parasite feature maximum extension events beyond 800 nm, with nectomonads again having slightly higher extension than the metacyclic stage.

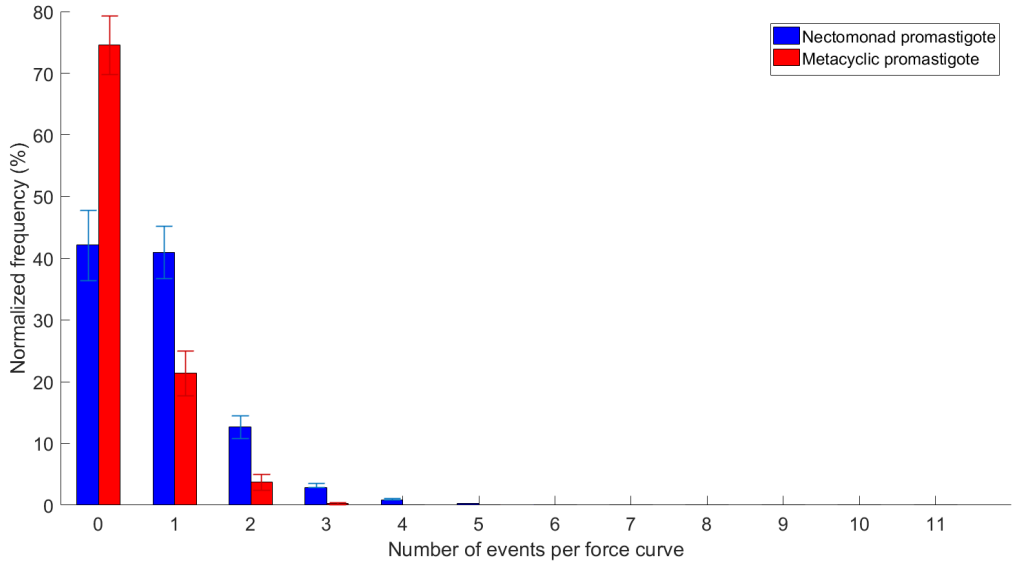

Figure 5.8: Normalized frequency bar chart showing the number of force events per interaction for nectomonad (blue) and metacyclic (red) promastigotes with a galactose coated AFM cantilever tip. The error bars show standard error.

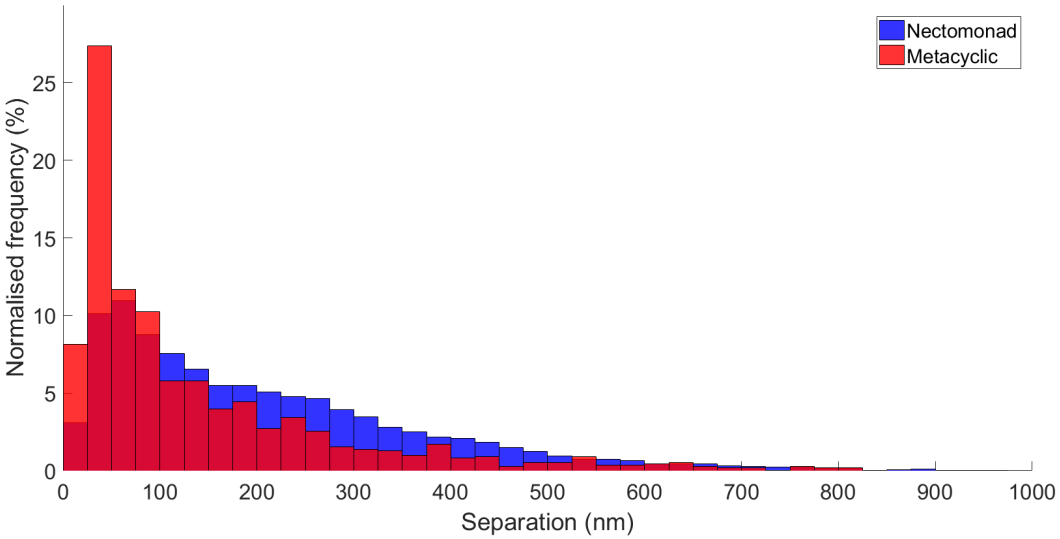

Figure 5.9: Normalized frequency histogram of extensions at which all force events are measured for nectomonad (blue) and metacyclic (red) promastigotes with a galactose coated AFM cantilever tip.

5.1.5 Conclusions

Anti-LPG coated tips demonstrated that scanning force microscopy can detect molecules on the surface of *Leishmania mexicana* parasites. The known extension of LPG in the metacyclic life stage can be detected as seen in Fig. 5.5 and confirms the backbone of LPG can be adhered to by the coating on the tip.

To interrogate the stage specific adhesion of specific molecules, the well defined sugar coated galactose tip provided a greater resolution than the anti-LPG antibody. Clear differences in the nature of binding (Fig. 5.8) and the magnitude of the binding between the two life stages (Fig. 5.7) was revealed using the custom MATLAB script to analyse the interactions using these tips.

This shows that modification of a cantilever with appropriate moieties can be used to study adhesion behaviour of parasites is a viable strategy for understanding specific interactions. Regarding the adhesion of *Leishmania mexicana* to sand fly guts, it shows that galactose-bearing proteins play a role alongside lipophosphoglycan.

5.2 Tetraspanin-enriched microdomains as a strategy to prevent bacterial infection of human epithelial cells

The methods for the construction of *M. luteus* biofilms on AFM cantilevers and their adhesion to poly(ethylene terephthalate) substrates are thoroughly documented in Chapters 2 and 3. Advancing from this initial study of a model bacterium and a model surface, these methods were adjusted to explore a more complex relationship by growing *Staphylococcus aureus* (*S. aureus*) biofilms on cantilevers to examine how their adhesion to epithelial cells can be modified.

5.2.1 Introduction

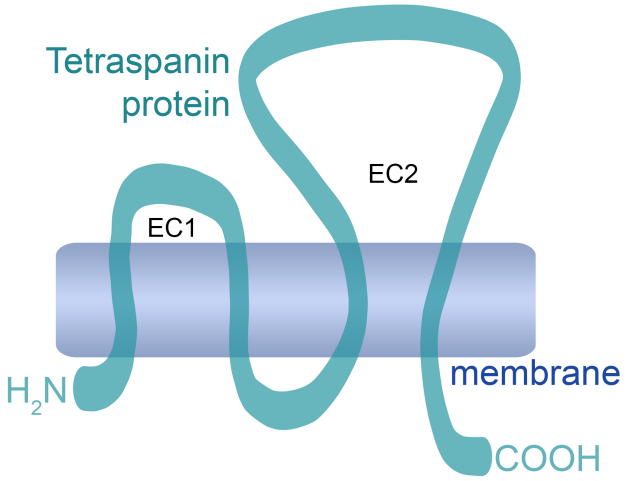

Figure 5.10: Tetraspanins feature four transmembrane domains, one intracellular loop, two intracellular termini and two extracellular loops (EC1 and EC2).

Tetraspanins are proteins that cross the membrane (transmembrane) of cells in a wide range of organisms, from sponges to humans.[86] The proteins span the membrane four times, contain charged residues, a single intracellular loop, two intracellular termini and feature a small and a large extracellular loop (Fig. 5.10). The large loop (EC2) forms specific protein-protein interactions.[87,154]

Using the EC2 loop, tetraspanins associate with each other and other proteins to form regions on the cell surface referred to as tetraspanin-enriched microdomains (TEMs).[87] By aggregating these components, tetraspanins are suited for organising cellular events such as fusion, adhesion, vesicle trafficking and exsome release.[86,155] It is well established that viruses use TEMs as a means of entering, traversing and exiting cells through the stages of viral infection and there is increasing evidence that bacteria are able to use TEMs to aid in colonisation and infection as well.[86]

Bacteria have a range of molecules that allow tight adhesion to molecules associated with the host cell surface, including fibronectin, CD36 and Hsc70. All of these molecules are known to interact with tetraspanins. It is in this way that bacteria are believed to exploit TEMs on cell surfaces. The tetraspanins do not interact directly with bacteria, but organise receptors in a manner that facilitates bacterial adhesion.[154] Through targeting this mechanism, short peptides derived from the sequence of the EC2 loop of the tetraspanin CD9 have been shown to cause a reduction in the colonisation of epithelial cells and 3D tissue-engineered models of human skin by *S. aureus*, without causing any adverse effects on the skin cells.[87]

The transmission of methicillin-resistant *Staphylococcus aureus* in clinical settings is responsible for a range of infections, with high mortality rates, such as sepsis and bacterimia. In the United Kingdom, 12,500 annual cases of *Staphylococcus aureus* bacterimia (SAB) had an approximate mortality rate of 30%.[156] In the United States of America, there are over 120,000 annual MRSA infections in general, which result in 20,000 deaths. If CD9 protein can be shown to decrease the adhesion of *S. aureus* to human epithelial cells, it would present a novel method for reducing the transmission of MRSA in hospital and other clinical environments. To investigate this possibility, the adhesion of *S. aureus* to HeLa cells (commonly used cancer epithelial cells) that had been treated with CD9 protein were examined using atomic force microscopy (AFM).

5.2.2 Previous work

Direct stochastic optical resolution microscopy (STORM) was used to visualise the distribution of CD9 on epithelia cell membranes. The CD9 molecules were always found in clusters, with a geometric mean radius of approximately 30 nm. Following treatment with CD9 peptide (but not with scrambled sequence controls), the geometric mean radius and surface area of the clusters was significantly increased. The peptide treatment did not affect the surface expression of CD9, so the change is likely to be the result of increased spacing of the CD9 molecules in the TEM clusters.

The increased spacing of CD9 molecules might lead to a similar increase in the spacing of molecules co-clustered with CD9 in adhesion platforms, potentially decreasing the binding force. Scanning force microscopy was employed to study this claim and establish if there is a change in adhesion of *S. aureus* with these epithelial cells once treated with CD9 peptide.

5.2.3 Methods

Biofilms were established on tipless NP-O10 cantilevers as described in Section 2.1.2. The method varied through the use of *Staphylococcus aureus* (*S. aureus*) rather than *M. luteus*.

The *S. aureus* used was SH1000, a widely used laboratory strain. It was grown in Luria-Bertani (LB) broth for approximately 10 h to stationary phase.

The EC2 region of CD9 tetraspanin was divided into 14-15 amino acid segments and synthesized using solid phase fluorenylmethyloxycarbonyl protecting group (referred to as Fmoc) chemistry (Genscript, New Jersey, USA). Scrambled peptide sequences were randomly generated from the CD9 sequence.

The scan size of the scanning force microscope was limited to 1×1 μm^2 to main-

tain the bioprobe on the surface of the HeLa cell. The force distance was set to 4 µm due to the long range of interactions observed between the cell and the bioprobe. The z velocity was 2 µm/s, with a trigger point of 5 nN and a 5 s dwell at contact.

As seen in Fig. 5.11, the interaction between a HeLa cell and a *S. aureus* bioprobe lacks the detailed force interactions observed in earlier chapters of this thesis. This is partly due to the softer trigger point and shorter dwell used (10 nN and 5 s here compared to 20 nN and 10 s for *M. luteus* biofilms against PET substrates in Chapter 3) to avoid damaging the delicate HeLa cell. Force analysis is therefore restricted to the traditional method of the peak interaction, rather than a more detailed investigation of the number of binding events per interaction.

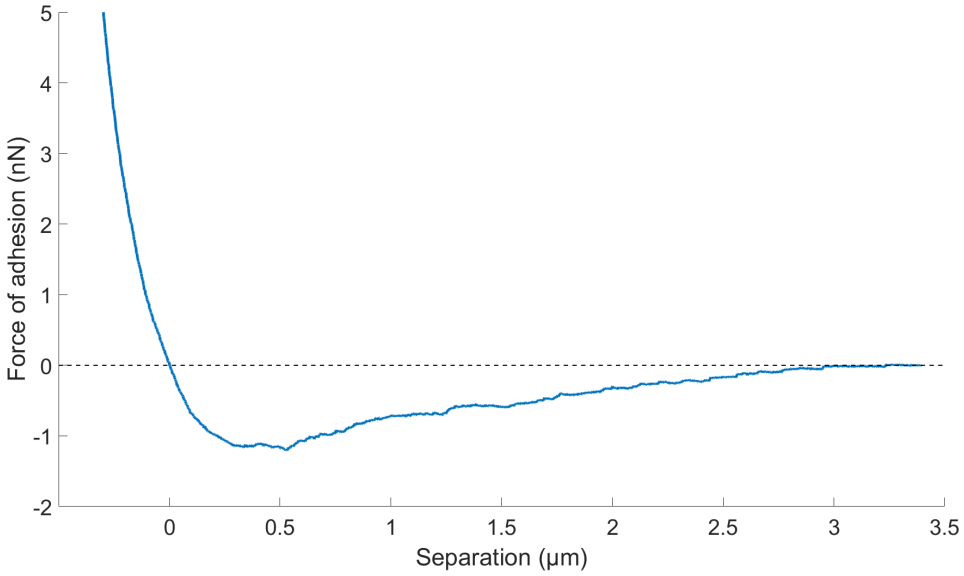

Figure 5.11: Typical retraction curve of the interaction between a *S. aureus* bioprobe and a HeLa cell.

5.2.4 Control measurements

Measurements against glass

As an initial control measurement, the interaction between a *S. aureus* biofilm and glass slides with and without peptide treatment were examined, as shown in Fig.

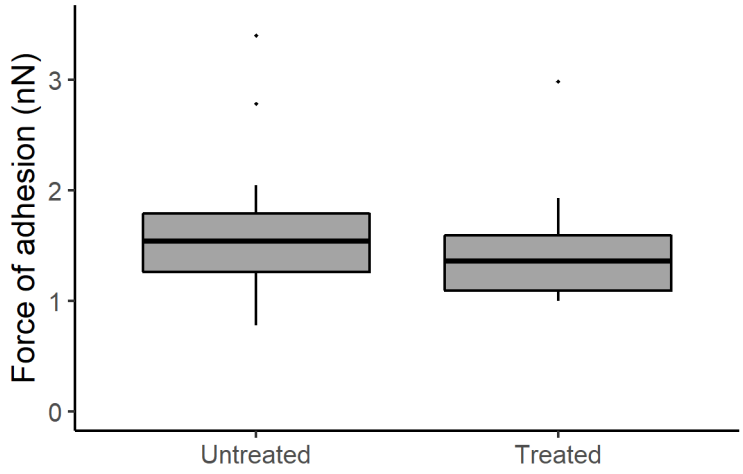

Figure 5.12: Box plots showing interaction of *S. aureus* bioprobe with glass that has and has not been treated with CD9 peptide.

5.12. The two sets of data are not significantly different (p = 0.29) and show that the presence of the CD9 peptide alone does not alter the adhesion of the biofilm to substrates.

Scrambled peptide sequences

A second control measurement was that of the scrambled peptide sequences, to confirm they were not having an active effect on the adhesion of the biofilm. These peptides contained the same amino acids as the active sample, but were in a random order, which should produce no effect in the adhesion between the biofilm and HeLa cell.

As seen in Fig. 5.13, despite some variation in the force values recorded against non-treated HeLa cells, the cells treated with scrambled peptide align with these control values. Fig. 5.14 shows that when the measurements are grouped together, there is no significant difference between the control and scramble treated HeLa cells (p value = 0.6). The mean force value for interactions between control HeLa cells and this *S. aureus* bioprobe was 1.10 ± 0.03 nN and the mean interaction between

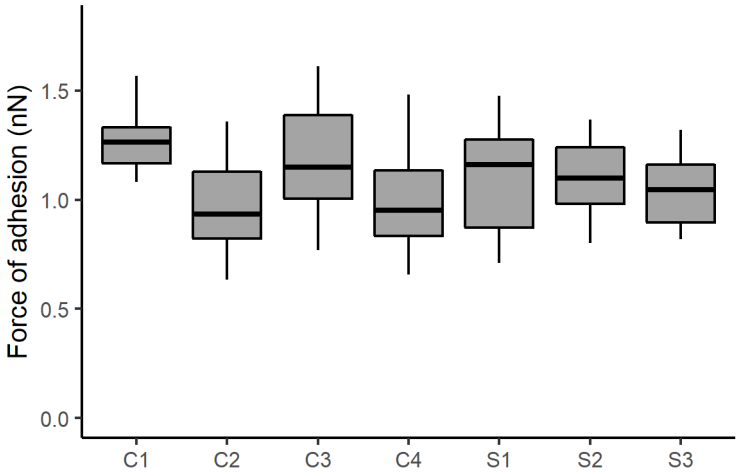

Figure 5.13: Box plots showing interaction of *S. aureus* bioprobe with control HeLa cells that have not been treated (C1-4) and HeLa cells that have been treated with a scrambled CD9 protein (S1-3).

HeLa cells treated with scrambled peptide was 1.08 ± 0.03 nN. This confirms that the scrambled peptide does not affect the adhesion of *S. aureus* bioprobes to the HeLa cells and that any change seen from treatment with active peptide will be due to the specificity of the sequence.

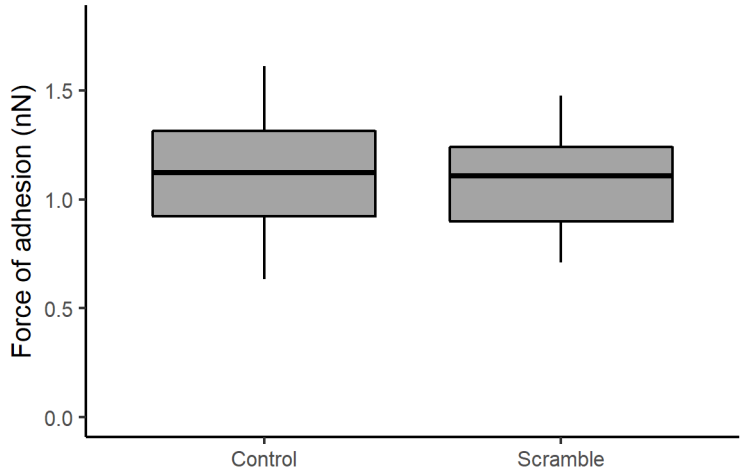

Figure 5.14: Box plots showing combined interaction of *S. aureus* bioprobe with control HeLa cells that have not been treated and HeLa cells that have been treated with a scrambled CD9 protein. The difference is non-significant ($p = 0.6$).

5.2.5 CD9 treated HeLa cells

With control measurements confirmed, HeLa cells that had been treated with CD9 were investigated in the same manner. As Fig. 5.15 shows, readings for both untreated control cells and CD9 treated HeLa cells were readily repeated, with little variation between cells. There is a clear decrease in adhesion of the bioprobe to cells that have been treated with the CD9 protein. When these readings are grouped, as shown in Fig. 5.16, the effect of the treatment is clear, with a decrease in adhesion of 51% (mean force values decreased from 5.38 ± 0.08 nN to 2.62 ± 0.06 nN, p value $\ll 0.05$).

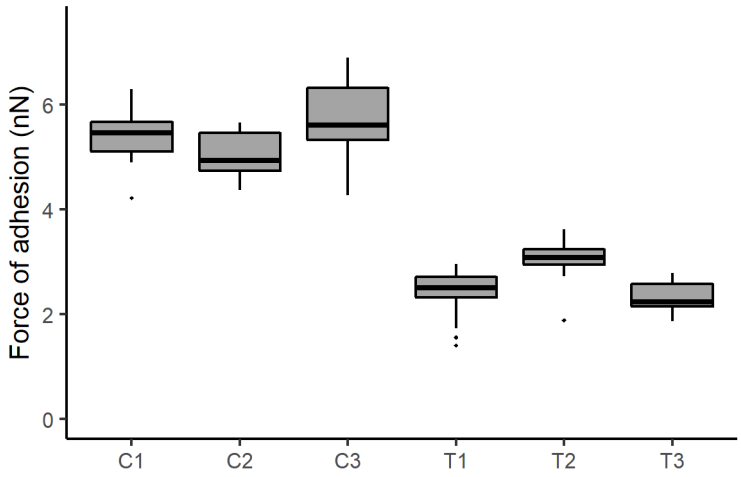

Figure 5.15: Box plots showing interactions of *S. aureus* bioprobe with control (C1-3) HeLa cells that have not been treated and HeLa cells that have been treated (T1-3) with active CD9 protein.

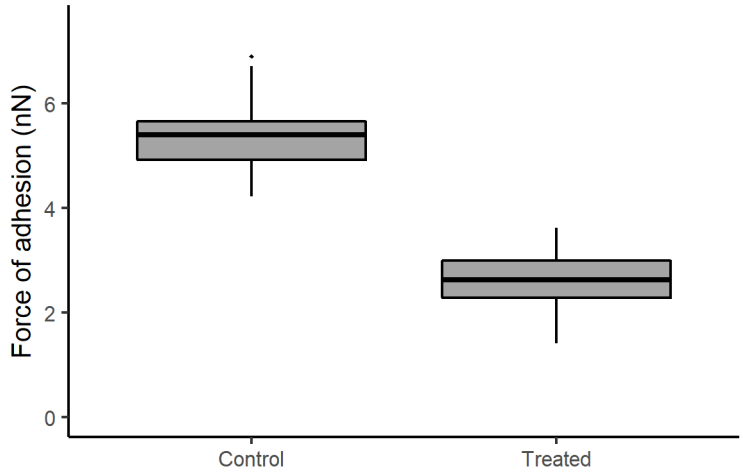

Figure 5.16: Box plots showing combined interaction of *S. aureus* bioprobe with control HeLa cells that have not been treated and HeLa cells that have been treated with active CD9 protein. The difference is significant ($p <<< 0.05$).

The effect of CD9 can be clearly observed in Fig. 5.15 and Fig. 5.16. STORM experiments described in Section 5.2.2 had observed some treated cells that did not display a disrupted TEM. A single instance of this was observed in AFM experiments, where a treated cell adhered to the *S. aureus* bioprobe in a manner similar to the untreated controls (T1 of Fig. 5.17).

Fig. 5.18 shows that when the responses from multiple controls and treated cells are grouped together, it is confirmed there is no significant difference between the single failed treatment observation and control measurements (p value = 0.29). HeLa cells are from a cancer line and therefore divide rapidly. It is believed this observation of a failed treatment is due to a HeLa cell that has divided during the peptide treatment period and features freshly formed TEM that have not been disrupted by the peptide.

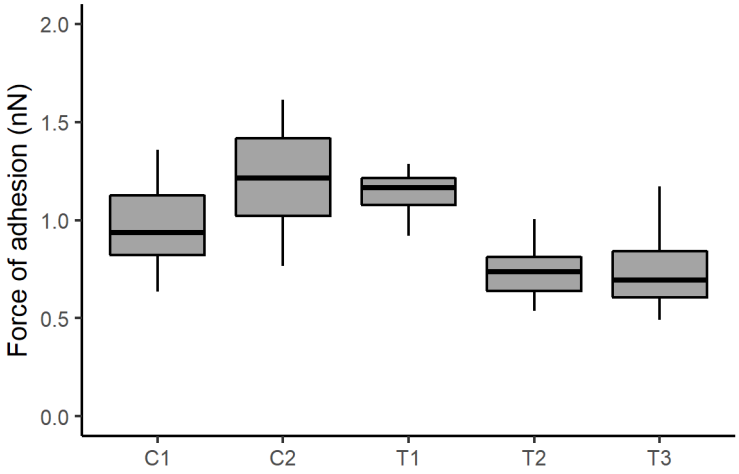

Figure 5.17: Selected box plots showing interactions of *S. aureus* bioprobe with control (C1-2) HeLa cells that have not been treated and HeLa cells that have been treated (T1-3) with active CD9 protein.

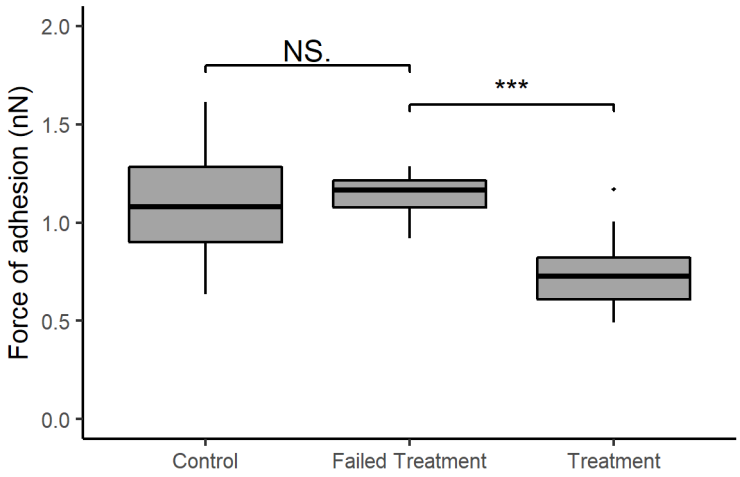

Figure 5.18: Box plots showing combined interactions of *S. aureus* bioprobe with control HeLa cells that have not been treated, a treated cell that has not changed in force response and HeLa cells that have been successfully treated with active CD9 protein. NS indicates non-significant comparison. *** indicates highly significant difference, $p \ll 0.05$.

5.2.6 Conclusions

Atomic force microscopy (AFM) was successfully used to probe the interaction of an SH1000 *S. aureus* biofilm with HeLa cells that had been treated with CD9 peptide. This treatment caused a decrease of 51% in average adhesion between biofilm and cell surface. This evidence supports the hypothesis that the additional spacing observed between CD9 may also disrupt the co-clustered adhesive molecules in the TEM.

The decrease is confirmed as an active effect of the peptide due to control measurements that show no change in adhesion between the bioprobe and glass that has and has not been exposed to the peptide. Additionally, HeLa cells treated with scrambled peptide sequences were tested and showed no significant difference to control values.

AFM confirmed observations seen in STORM data that some treated cells do not register a decrease in bacterial adhesion, most likely caused by a fresh division of the cell, exposing non-disrupted TEM regions.

5.3 Summary

Using different modifications of scanning force microscopy cantilever tips, two different pathogens were investigated for their adhesion to their relevant substrates. A *Staphylococcus aureus* (*S. aureus*) biofilm was grown on a tipless cantilever and probed against HeLa epithelial cells to investigate the effect of a peptide treatment that was hypothesised to decrease bacterial adhesion. The force measurements indicated that the treatment with this specific peptide sequence reduced adhesion of *S. aureus* by 51%. It is thought this reduction in adhesion occurs by disrupting the adhesive platforms found to co-cluster in tetraspanin-enriched microdomains (TEMs).

In a different study, a lipophosphglycan (LPG) antibody was bound to a tipped cantilever via glutaraldhehyde to confirm that AFM can measure specific molecular interactions on the surface of *Leishmania mexicana* parasites. The anti-LPG tip was able to distinguish between wild type and mutant parasites that had had their LPG production gene suppressed. The extension of LPG in a different life stage of the parasite was also observed. Data analysis of previous work using a custom MATLAB script gave new insight into the changing mechanisms used by the parasites as they mature and become infective.

These two studies provided answers and additional understanding to medically relevant projects that are seeking to fight parasitic infections that are especially difficult to combat due to different forms of drug resistance.

Chapter 6

Conclusions

This work used force spectroscopy with biofilm coated cantilevers to investigate the effect of hydrolytic enzymes on various extracellular polymeric substances. Elsewhere, biofilms have been grown on cantilevers to examine their adhesive nature towards a range of substrates. This method has not previously been used to modify the biofilm while on the tip in order to observe the change of adhesion.

Using custom MATLAB scripts allowed for a more thorough investigation of each force-distance curve produced by biofilms interacting with PET substrates. The ability to index the number of events per interaction enabled analysis of the way in which the biofilm was binding to the substrate before and after being exposed to enzyme. This analysis highlighted subtle changes in the adhesion of the biofilms, indicating a structural nature to the target of the enzyme where the number of attachment points decreased. Traditional techniques for quantifying enzyme activity on biofilms relies on optical measurements and adhesion binding assays. By physically interacting with the biofilm, these structural changes can be detected and differentiated from enzymes that cause only a reduction in adhesion. Proteins ($54 \pm 12\%$ reduction in adhesion, number of events per measurement reduced by one when targeted) and DNA ($92 \pm 3\%$ reduction in adhesion, number of events per measurement reduced by three) were established as structural components of the *M. luteus* biofilm, while polysaccharides were concluded to play adhesive roles (no

reduction in number of events per measurement by cellulase or mannanase. Cellulase treatment reduced adhesion by $53 \pm 7\%$ and mannanase treatment reduced adhesion by $40 \pm 5\%$). It is through these observations that force spectroscopy can be used to properly identify the key molecules in a biofilm and guide more effective degradation methods.

The results of Chapter 3 identified extracellular DNA as a major structural component of the *Micrococcus luteus* (*M. luteus*) biofilm. A novel engineered DNase, called S3, was found to be just as effective as DNaseI, at 10% of the concentration. To understand the mechanism action the enzyme was studied using real world conditions, with the aid of computer modelling. A range of potential variables were screened and surfactant concentration was found to be relevant. A design of experiment method was used to investigate the individual components of the surfactant formulation for their effect on the enzyme activity. The hydrophillic index of the formulation was found to influence the activity of the enzyme against DNA stains, with maximum enzyme efficiency occuring at hydrophillic index values between 8.5 and 10. QCM-D was used to further examine tailored surfactant formulations. Hydrophillic index values were found to be of interest and revealed changing adsorption and release rates. The enzyme's activity was highest when it could rapidly gain access to, and leave, the surface. This confirmed a hopping mechanism that had previously been proposed.

The methods developed in Chapter 3 used a model bacterium and a model surface. Once the method is mature, the most advantageous step forward would be to identify the structural components of pathogenic or drug resistant biofilms. Degradation of the protective biofilm may allow current or new drugs and chemicals a foothold into the community, presenting a way of dispersing the bacteria. This type of characterisation of multiple pathogens would be a project in itself, so intermediate steps were taken in this thesis. In Chapter 5.3, the tools and techniques developed through the project were used to complement work already conducted against two

pathogens, *Staphylococcus aureus* and *Leishmania mexicana*.

The method of growing *M. luteus* biofilms on the cantilever was modified to grow *Staphylococcus aureus* (*S. aureus*). Epithelial HeLa cells were treated with a protein that was designed to disrupt their tetraspanin-enriched microdomains (TEMs). It is thought that these TEMs allow adhesive platforms, used by bacteria in colonising skin, to co-cluster. Disruption of the TEMs had been confirmed through increased spacing of the clusters via stochastic optical reconstruction microscopy (STORM). Force spectroscopy was used to identify if bacteria adhesion had been decreased. Biofilms cantilevers measured the adhesion values between *S. aureus* and these epithelial cells and confirmed a 52% decrease in adhesion for those cells that had been treated with the disrupting protein. A range of control measurements ensured the reduction in adhesion was an active result of the specific protein binding. These findings can lead to a treatment that would disrupt the adhesion of *S. aureus* to human skin, providing great use in limiting the transmission of methicillin-resistant *S. aureus* (MRSA) in clinical settings.

The computer scripts designed during this project were used to further analyse previous force spectroscopy data between *Leishmania mexicana* (*L. mexicana*) parasites and galactose-coated cantilevers. The binding of *L. mexicana* to galactose residues was under investigation, as it was thought to be life stage specific. The additional data extracted using the custom MATLAB scripts developed in this project allowed the subtle changes in the number of force-events per interaction to be examined. A stage specific change in binding nature was observed which helped further the understanding of the binding mechanisms of these parasites (average number of events in a nectomonad force-distance curve 0.8 ± 0.1 compared to 0.3 ± 0.1 per curve belonging to a metacyclic). In a similar manner to the experiments with *S. aureus* and *M. luteus*, this helps guide further work by identifying targets of chemical importance.

In summary, force spectroscopy was used successfully to study the adhesive properties of bacteria and parasites. By establishing a biofilm on the cantilever and modifying it through hydrolytic enzymes, structural components of the biofilm can be identified in a way that traditional methods cannot. The methods refined against thin film substrates in this project were also used against the more challenging substrate of cells and parasites. Biofilm adhesion to epithelial cells was studied, as well as data analysis of parasite interactions with chemically defined cantilevers. Computer software was used and developed alongside experiments to give further insight to the data collected. This was shown in Chapter 4 with statistical modelling of rapid data collection and in Chapters 3 and 5.3 to extract additional information from force spectroscopy results. This information combines to direct further research towards measures that can combat the problems and risks associated with undesirable adhesion of bacteria and parasites.

Appendix A

Custom MATLAB script

A.1 Need for external scripting

Early on in the project, it became apparent from visually inspecting the force-distance curves that there was a lot of information that could be analysed in the individual peaks the AFM captured. The native software of the AFM is lacking when it comes to extracting this information and was prone to crashing. For this reason, the control software is used to automatically offset the AFM curves to account for drift and the x-y coordinates are exported as comma separated value (.csv) files to be imported into MATLAB, which can quickly process the data according to custom build scripts.

The first generation of custom MATLAB script presented the user with each force-distance curve and a cross hair cursor. The user was asked to click on each force peak that was deemed to be of interest and the coordinates would be logged by the script. The end product of this task was possible in the control software, but would take approximately an hour for a 10×10 force map as it involved hovering the mouse over the point, writing down the coordinates from the tool-tip and digitising the data into Microsoft Excel. The process in MATLAB reduced this time to approximately 30 seconds and eliminated chances for human error to introduce mistakes in the writing down and digitisation of the data. Although a large im-

provement, there was still more that MATLAB could do.

The main aim was to create a script that would interpret the data as a human would, knowing which peaks were valid force events and knowing when to discount events, such as small blips on a larger peak, or peaks that stood out from the noise, but did not pass a threshold value. If the code was capable of this recognising peaks, without requiring a human to interpret and click, a 10×10 force map could be processed in a matter of seconds with an additional few minutes of manually reviewing the selected points as a quality control step.

Having the MATLAB script being able to identify peaks and troughs in the data is reasonably straight forward and is detailed in Section A.2. The more difficult part of the development was writing code that mimics the decision making a human makes on borderline events and ignoring events that are flagged up mathematically, but are just a continuation of another event. This appendix section will detail the different sections of code and its purpose to the script as a whole. MATLAB functions and operators will be written in *italics* and variables in **bold**.

A.2 Identifying peaks in the data

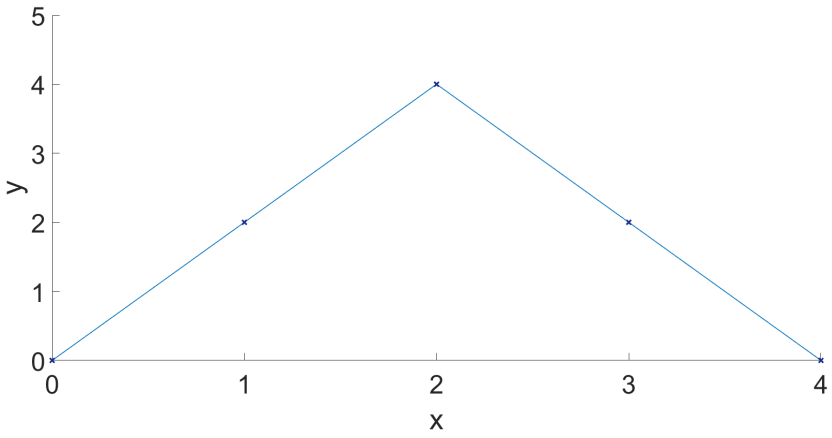

Figure A.1: Plot of points corresponding to those in A.1.

Listing A.1: Example code for peak identification

```
1  x = [0,1,2,3,4]
2  y = [0,2,4,2,0]
3
4  FirstDerivative = diff(y);
5  %output:  2, 2, -2, -2
6
7  FirstDerivativeLogical = diff(y) > 0;
8  %output: 1, 1, 0, 0
9
10 LogicalDiff = diff(diff(y) > 0);
11 %output: 0, -1, 0
```

Peaks and troughs are identified by examining the difference in adjacent points using the *diff* operator, finding the first derivative of the line. Using a simple plot containing the following 5 points: (0,0), (1,2), (2,4), (3,2), (4,0), the *diff* operator will be demonstrated to find the peak.

The first derivative values show that the y value increases by 2 per point across the the first half of the plot and then decreases by 2 for each point in the second half. Line 7 creates a logical set to simplify the movements. Here a 1 represents a TRUE value and 0 a FALSE value. The logical output does not take in to account the magnitude of increase or decrease, just the direction of the gradient. The two TRUE values signify the gradient of the line is positive between the first and second point and the second and third point, but negative between the third and fourth point and the fourth and fifth point.

Although obvious to a human viewer where the inflection point is, the code needs to capture the location. This is done on line 10 by examining the differences in the logical values. A negative value is recorded as the second value, which corresponds to the third point of the original data. This is because each derivative is offset by half the interval spacing and produces a set of data one fewer than the original. To realign the final output with the original data, **alltroughs** and **allpeaks** are

flanked by FALSE (0) values either side of the *diff* code block. A peak in the data will output -1 and a trough will output +1, which is used in assigning **allpeaks** and **alltroughs** by changing the direction of the second inequality symbol.

A.3 Variable identification and cleaning

Lines 5 and above feature in the developmental code and extract x and y coordinates from the imported force map. The y coordinates are smoothed using a simple moving average filter to avoid noise in the force-distance data being analysed by the code, rather than the obviously prominent force events.

As described in Section A.2, **alltroughs** and **allpeaks** are logicals, cataloguing the **yy** variable for the locations of peaks or troughs with TRUE (1) values. Theses are sequentally processed by the code and classified as valid force events or discarded.

Lines 8 and 9 set thresholds to be obeyed, which will vary depending on what kind of force data is being analysed and **dataCutoff** is a simple limit on how far along the curve the script should identify. The cutoff can be placed at the very end of the data, or be used to trim the data to a region of interest. **i** begins with a value of 1 and is increased by the code each time it iterates to move the focus of the code to the next pair of troughs and peaks. The **skip** variable defaults to zero and can be changed to 1 by certain parts of the code if it wishes to exclude the point in question from other tests. The value is always reset to zero after the skip has taken place.

The code enters the overarching *while* loop in section A.3. While the value of **i** is less than **dataCutoff** the loop will continue, with the code jumping the value of **i** along the x axis to move past force events that have been catalogued.

The variable **j** is created and set to always lag behind **i** by a value of 1. This aids in keeping the code clear when referencing the slices of data back to the whole data set and can be seen regularly in the various **if** statements.

Listing A.2: Initialisation of variables

```
%initialise variables
loc = 1;
x = values(:,loc);
y = values(:,loc+1);
yy = smooth(y);
alltroughs = [FALSE; diff(diff(yy) > 0) > 0; FALSE];
allpeaks = [FALSE; diff(diff(yy) > 0) < 0; FALSE];
ythreshold = 2.75e-10;
xthreshold = 8e-9;
dataCutoff = 700;

i = 1;
skip = 0; %default 0, code can change to 1 to move through
   section without running

%end initialisation of variables
```

Listing A.3: Determination of peaks and troughs

```
while i < dataCutoff
    j = i-1;
    troughs = alltroughs(i:end);
    peaks = allpeaks(i:end);

    findtrough = find(troughs,1);
    findpeak = find(peaks,1);

    nexttroughinterval = find(troughs(findtrough+1:end),1);
    nexttrough = nexttroughinterval + findtrough;
    nextpeakinterval = find(peaks(findpeak+1:end),1);
    nextpeak = nextpeakinterval + findpeak;
```

The variables **troughs** and **peaks** take slices of **alltroughs** and **allpeaks**, so that the data that has already been analysed is not included in the next iteration of the *while* loop. When the loop runs for the first time and **i** is equal to 1, the slices are identical to the entire data set.

The trough and peak of interest to this iteration of the loop are found using the MATLAB logical operator, *find*. Line 22 and 23 involve searching the relevant variable for the first instance of a non-zero value in **troughs** and stores this location in the variable **findtrough**. On following loops through this section of code, the value of **i** will have increased to exclude points already examined. This allows the code to simply rely on looking for the first instance of a non-zero value in the slice.

The final four lines of this section give the code an awareness of the trough and peak pair that follow it, slicing the data past what has already been identified. These next locations are used by some code arguments to properly identify the type of event that is being dealt with.

Code section A.4 is the first of many *if* statements that aims to clean up the data, reclassifying or removing some trough-peak pairings. It makes a decision on an identified trough if there is an already accepted peak closely preceding it. Line 31 features a *try* statement as an error will be produced on the first iteration of the while loop as the **findtrough+j-10** can become negative. The *if* statement makes a slice of the 10 points before the identified trough and looks for the presence of a peak. If none is found, the argument is equal to zero and the *if* statement ends. If there is a peak, it is further inspected in the *else* statement starting on line 33.

The previous peak is translated back to its global position and its y values is compared to that of the trough in question. If the trough is at least a quarter of the **ythreshold** below the peak, it is left to be analysed by the rest of the code. If the trough is too small, it and the corresponding peak are determined to be a section of noise. The pair is removed and the **skip** variable increased to a value of 1 so rest of

Listing A.4: Check for previous peaks being close to current trough

```
30 %This is inside the while loop
31 try if sum(allpeaks(findtrough+j-10:findtrough+j)) == 0
32         %no peaks close, carry on
33     else
34         previouspeak = find(allpeaks(findtrough+j-10:
               findtrough+j),1) + findtrough+j-10 -1;
35         if yy(previouspeak) - yy(findtrough+j) > ythreshold
               /4
36             %do nothing
37         else
38             allpeaks(findpeak+j) = 0;
39             alltroughs(findtrough+j) = 0;
40             skip = 1;
41             disp('Pair removed as previous peak too close to
                   trough in question')
42         end
43
44     end
45 end
```

the code is not run.

Code section A.5 runs checks on the x and y positions of the current peak and the next trough. The first part of the *if* statement on line 49 checks the x separation between the current peak and the next potential trough. The second part of the *if* statement compares the y separation of the same two points, to check for a plateau force event (an extension in the x direction with minimal variation in y). Without this section of the code, plateaus are regularly misclassified as non-events. The absolute value (*abs*) is used as the y variation may be slightly positive or negative. If the points are close in either x or y space, the peak and the next trough are removed. The next peak is redefined as the current peak. This allows the trough to be compared against a new higher peak.

Listing A.5: Check for next trough being close to current peak

```
47 %This is inside the while loop
48 if skip == 0
49         if x(nexttrough+j) - x(findpeak+j) < xthreshold ||
              abs(yy(nexttrough+j) - yy(findpeak+j)) < (yy(
              findpeak+j) - yy(findtrough+j))/12
50             %delete findpeak and nexttrough, analyse on
                  findtrough and nextpeak
51             allpeaks(findpeak+j) = 0;
52             alltroughs(nexttrough+j) = 0;
53             findpeak = nextpeak;
54             disp('expanded check to next peak due to
                  proximity')
55         end
```

A.4 Validation of force event

In code section A.6, the trough and peak are now evaluated against the selected y-threshold. If the force event is large enough, the *if* statement on line 58 is true. The trough and peak pair are confirmed and no further reaction is required, as their value in the logical matrices is already = 1. If the force event is smaller than the threshold, the *elseif* statement on line 62 becomes active and true. This rejects the trough and peak pairing, making their logical value = 0. After the *if* statement ends, the value of i is increased to the location of the current peak and then advanced by a single point. The code will assess the next pair of trough and peak on the next iteration.

Eventually the value of **i** becomes greater than **dataCutoff**, which causes the code to break out of the *while* loop that started in section A.3. In section A.7, line 69 and 70, the remaining part of the force-distance curve is declare empty of valid points. There are now two logical matrices, **allpeaks** and alltroughs which identify the accepted points.

The force-distance curve is presented to the user with valid troughs overlaid with red (ro) circles and the peaks with blue arrows (b∧). Depending on the mode of operation, the user can select to visually confirm each of these curves, with the overlaid points, or simply let the code identify without intervention. Either mode of operation produces results in seconds or minutes that would take hours or days if manually extracting the data from the AFM software.

Listing A.6: Compare trough and peak

```
57 %This is inside the while loop
58  if yy(findpeak+j) - yy(findtrough+j) > ythreshold
59              %point is fine, move on to next one
60              disp('Point accepted')
61          elseif yy(findpeak+j) - yy(findtrough+j) <
               ythreshold
62                  %need to delete this point
63                  allpeaks(findpeak+j) = 0;
64                  alltroughs(findtrough+j) = 0;
65                  disp('Point rejected')
66          end
67          i = findpeak+j+1; %moves index to current peak, + 1
```

Listing A.7: Plot final results of the curve

```
69          allpeaks(dataCutoff+1:end) = 0;
70          alltroughs(dataCutoff+1:end) = 0;
71
72          plot(x,yy)
73          hold
74
75          plot(x(alltroughs),yy(alltroughs), 'ro' )
76          plot(x(allpeaks),yy(allpeaks), 'b^' )
```

Bibliography

[1] M. Young, V. Artsatbanov, H. R. Beller, G. Chandra, K. F. Chater, L. G. Dover, E. B. Goh, T. Kahan, A. S. Kaprelyants, N. Kyrpides, A. Lapidus, S. R. Lowry, A. Lykidis, J. Mahillon, V. Markowitz, K. Mavromatis, G. V. Mukamolova, A. Oren, J. S. Rokem, M. C. Smith, D. I. Young and C. L. Greenblatt, *Journal of Bacteriology*, 2010, **192**, 841–860.

[2] A. Fleming and V. D. Allison, *British Journal of Experimental Pathology*, 1922, **3**, 252–260.

[3] M. S. Conover, M. Mishra and R. Deora, *PLOS ONE*, 2011, **6**, e16861.

[4] C. L. Greenblatt, J. Baum, B. Y. Klein, S. Nachshon, V. Koltunov and R. J. Cano, *Microbial Ecology*, 2004, **48**, 120–127.

[5] T. R. Sandrin and R. M. Maier, *Environmental Health Perspectives*, 2003, **111**, 1093–1101.

[6] C. Callewaert, E. De Maeseneire, F.-M. Kerckhof, A. Verliefde, T. Van de Wiele and N. Boon, *Applied and Environmental Microbiology*, 2014, **80**, 6611–6619.

[7] C. B. Klee and M. F. Singer, *The Journal of Biological Chemistry*, 1968, **243**, 5094–5100.

[8] F. Erbasan, *Rheumatology International*, 2018, **38**, 2323–2328.

[9] A. Pekala, E. Paździor, J. Antychowicz, A. Bernad, H. Głowacka, B. Wiecek and W. Niemczuk, *Aquaculture*, 2018, **486**, 285–289.

[10] J. J. Leyden, K. J. McGinley, E. Hölzle, J. N. Labows and A. M. Kligman, *Journal of Investigative Dermatology*, 1981, **77**, 413–416.

[11] A. James, J. Casey, D. Hyliands and G. Mycock, *World Journal of Microbiology and Biotechnology*, 2004, **20**, 787–793.

[12] L. S. Cairns, L. Hobley and N. R. Stanley-Wall, *Molecular Microbiology*, 2014, **93**, 587–598.

[13] H. H. Tuson and D. B. Weibel, *Soft Matter*, 2013, **9**, 4368–4380.

[14] L. Hall-Stoodley, J. Costerton and P. Stoodley, *Nature Reviews. Microbiology*, 2004, **2**, 95–108.

[15] L. Hobley, C. Harkins, C. E. MacPhee and N. R. Stanley-Wall, *FEMS Microbiology Reviews*, 2015, **39**, 649–669.

[16] R. Nijland, M. J. Hall and J. G. Burgess, *PLOS ONE*, 2010, **5**, e15668.

[17] M. Sadekuzzaman, S. Yang, M. F. R. Mizan and S. D. Ha, *Comprehensive Reviews in Food Science and Food Safety*, 2015, **14**, 491–509.

[18] D. Dufour, V. Leung and C. M. Lévesque, *Endodontic Topics*, 2012, **22**, 2–16.

[19] M. Habash and G. Reid, *The Journal of Clinical Pharmacology*, 1999, **39**, 887–898.

[20] R. Bos, H. C. van der Mei and H. J. Busscher, *FEMS Microbiology Reviews*, 1999, **23**, 179–230.

[21] R. M. Donlan and J. W. Costerton, *Clinical Microbiology Reviews*, 2002, **15**, 167–193.

[22] P. Stoodley, K. Sauer, D. G. Davies and J. W. Costerton, *Annual Review of Microbiology*, 2002, **56**, 187–209.

[23] H. Xu, A. E. Murdaugh, W. Chen, K. E. Aidala, M. A. Ferguson, E. M. Spain and M. E. Núñez, *Langmuir*, 2013, **29**, 3000–3011.

[24] S. Srey, I. K. Jahid and S.-D. Ha, *Food Control*, 2013, **31**, 572–585.

[25] H.-C. Flemming, T. R. Neu and D. J. Wozniak, *Journal of Bacteriology*, 2007, **189**, 7945–7947.

[26] S. Voběrková, S. Hermanová, K. Hrubanová and V. Krzyžánek, *Folia Microbiol*, 2016, **61**, 91–100.

[27] S. Schlafer and R. L. Meyer, *Journal of Microbiological Methods*, 2017, **138**, 50–59.

[28] H. Flemming and J. Wingender, *Relevance of Microbial Extracellular Polymeric Substances (EPSs)–Part I: Structural and Ecological Aspects.*, 2001, vol. 43.

[29] D. G. Allison, *Biofouling*, 2003, **19**, 139–150.

[30] K. Schwartz, M. Ganesan, D. E. Payne, M. J. Solomon and B. R. Boles, *Molecular Microbiology*, 2016, **99**, 123–134.

[31] I. W. Sutherland, *Trends in Microbiology*, 2001, **9**, 222–227.

[32] I. W. Sutherland, in *Microbial Extracellular Polymeric Substances*, ed. J. Wingender, T. R. Neu and H.-C. Flemming, Springer Berlin Heidelberg, Berlin, Heidelberg, 1999, pp. 201–216.

[33] J. Wingender, K. E. Jaeger and H.-C. Flemming, in *Microbial Extracellular Polymeric Substances*, ed. J. Wingender, T. R. Neu and H.-C. Flemming, Springer Berlin Heidelberg, Berlin, Heidelberg, 1999, pp. 231–251.

[34] B. Frølund, T. Griebe and P. H. Nielsen, *Applied Microbiology and Biotechnology*, 1995, **43**, 755–761.

[35] J. H. Paul and W. H. Jeffrey, *Applied Enviromental Microbiology*, 1985, **50**, 431–437.

[36] C. Mayer, R. Moritz, C. Kirschner, W. Borchard, R. Maibaum, J. Wingender and H.-C. Flemming, *International Journal of Biological Macromolecules*, 1999, **26**, 3–16.

[37] H.-C. Flemming, J. Wingender, C. Mayer, V. Körstgens and W. Borchard, *Cohesiveness in Biofilm Matrix Polymers*, 2000.

[38] A. Faghihnejad and H. Zeng, *Langmuir*, 2013, **29**, 12443–12451.

[39] N. P. Boks, W. Norde, H. C. van der Mei and H. J. Busscher, *Microbiology*, 2008, **154**, 3122–3133.

[40] N. I. Abu-Lail and T. A. Camesano, *Environmental Science & Technology*, 2003, **37**, 2173–2183.

[41] S. Levine, *Proceedings of the Royal Society of London. Series A. Mathematical and Physical Sciences*, 1939, **170**, 165–182.

[42] S. Levine and G. P. Dube, *Trans. Faraday Soc.*, 1939, **35**, 1125–1140.

[43] B. Derjaguin and L. Landau, *Progress in Surface Science*, 1993, **43**, 30–59.

[44] E. J. W. Verwey and J. T. G. Overbeek, *Journal of Colloid Science*, 1955, **10**, 224–225.

[45] C. Demetzos, *Pharmaceutical Nanotechnology*, Springer Singapore, Singapore, 2016.

[46] J. Lyklema, W. Norde, M. C. M. van Loosdrecht and A. J. B. Zehnder, *Colloids and Surfaces*, 1989, **39**, 175–187.

[47] J. N. Israelachvili, in *Intermolecular and Surface Forces*, Elsevier, 3rd edn., 2011, pp. 253–289.

[48] J. N. Israelachvili, in *Intermolecular and Surface Forces*, Elsevier, 3rd edn., 2011, pp. 291–340.

[49] J. Polte, *CrystEngComm*, 2015, **17**, 6809–6830.

[50] C. J. van Oss, *Interfacial Forces in Aqueous Media.*, Marcel Dekker Inc., New York, USA, 1994.

[51] Y.-L. Ong, A. Razatos, G. Georgiou and M. M. Sharma, *Langmuir*, 1999, **15**, 2719–2725.

[52] M. C. M. van Loosdrecht, W. Norde, J. Lyklema and A. J. B. Zehnder, *Aquatic Sciences*, 1990, **52**, 103–114.

[53] R. Coico, in *Current Protocols in Microbiology*, ed. R. Coico, T. Kowalik, J. Quarles, B. Stevenson and R. Taylor, John Wiley & Sons, Inc., Hoboken, NJ, USA, 2005, pp. A.3C.1–A.3C.2.

[54] Q. Ding and K. S. Tan, *Frontiers in Cellular and Infection Microbiology*, 2016, **6**, 115.

[55] A. E. Zeraik and M. Nitschke, *Brazilian Archives of Biology and Technology*, 2012, **55**, 569–576.

[56] I. P. Molobela, T. E. Cloete and M. Beukes, *African Journal of Microbiology Research*, 2010, **4**, 1515–1524.

[57] C. Leroy, C. Delbarre, F. Ghillebaert, C. Compere and D. Combes, *Biofouling*, 2008, **24**, 11–22.

[58] S. Wang, X. Liu, H. Liu, L. Zhang, Y. Guo, S. Yu, D. J. Wozniak and L. Z. Ma, *Environ Microbiol Rep*, 2015, **7**, 330–340.

[59] J. T. Blakeman, A. L. Morales-García, J. Mukherjee, K. Gori, A. S. Hayward, N. J. Lant and M. Geoghegan, *Langmuir*, 2019, **35**, 6468–6475.

[60] J. S. Andrews, S. A. Rolfe, W. E. Huang, J. D. Scholes and S. A. Banwart, *Environmental Microbiology*, 2010, **9**, 2496.

[61] J. Das, E. Mokrzan, V. Lakhani, L. Rosas, J. A. Jurcisek, W. C. Ray and L. O. Bakaletz, *MBio*, 2017, **8**, e01466–17.

[62] J. B. Kaplan, K. Lovetri, S. T. Cardona, S. Madhyastha, I. Sadovskaya, S. Jabbouri and E. A. Izano, *Journal of Antibiotics*, 2012, **65**, 73–77.

[63] G. Binnig and C. F. Quate, *Physical Review Letters*, 1986, **56**, 930–933.

[64] *Atomic Force Microscopy in Liquid: Biological Applications*, ed. A. M. Baró and R. G. Reifenberger, Wiley, Weinheim, Germany, 2012.

[65] W. N. Sharpe, *Springer Handbook of Experimental Solid Mechanics*, Springer Science & Business Media, 2008.

[66] J. L. Hutter and J. Bechhoefer, *Review of Scientific Instruments*, 1993, **64**, 1868–1873.

[67] G. Lee, L. Chrisey and R. Colton, *Science*, 1994, **266**, 771–773.

[68] O. H. Willemsen, M. M. Snel, A. Cambi, J. Greve, B. G. De Grooth and C. G. Figdor, *Biophysical Journal*, 2000, **79**, 3267–3281.

[69] M. Ludwig, V. T. Moy, M. Rief, E.-L. Florin and H. E. Gaub, *Microscopy Microanalysis Microstructures*, 1994, **5**, 321–328.

[70] V. Moy, E. Florin and H. Gaub, *Science*, 1994, **266**, 257–259.

[71] E. Florin, V. Moy and H. Gaub, *Science*, 1994, **264**, 415–417.

[72] V. T. Moy, E.-L. Florin and H. E. Gaub, *Colloids and Surfaces A: Physicochemical and Engineering Aspects*, 1994, **93**, 343–348.

[73] P. Hinterdorfer, W. Baumgartner, H. J. Gruber, K. Schilcher and H. Schindler, *Proc. Natl. Acad. Sci. USA*, 1996, **93**, 3477–3481.

[74] W. R. Bowen, N. Hilal, R. W. Lovitt and C. J. Wright, *Colloids and Surfaces A: Physicochemical and Engineering Aspects*, 1998, **136**, 231–234.

[75] A. Razatos, Y. L. Ong, M. M. Sharma and G. Georgiou, *Proc. Natl. Acad. Sci. USA*, 1998, **95**, 11059–11064.

[76] M. Thie, R. Rospel, W. Dettmann, M. Benoit, M. Ludwig, H. E. Gaub and H. W. Denker, *Human Reproduction*, 1998, **13**, 3211–3219.

[77] S. K. Lower, M. F. Hochella Jr. and T. J. Beveridge, *Science*, 2001, **292**, 1360–1363.

[78] A. Beaussart, S. El-Kirat-Chatel, P. Herman, D. Alsteens, J. Mahillon, P. Hols and Y. F. Dufrêne, *Biophysical Journal*, 2013, **104**, 1886–1892.

[79] R. Yongsunthon and S. K. Lower, in *Advances in Applied Microbiology*, Elsevier, 2005, vol. 58, pp. 97–124.

[80] K. K. Jefferson, *FEMS Microbiology Letters*, 2004, **236**, 163–173.

[81] A. R. Hall, *Ph.D. thesis*, 2015.

[82] A. Hassoun, P. K. Linden and B. Friedman, *Critical Care*, 2017, **21**, 211.

[83] D. Fleming and K. Rumbaugh, *Microorganisms*, 2017, **5**, 15.

[84] S. DebRoy, O. Prosper, A. Mishoe and A. Mubayi, *Emerging Themes in Epidemiology*, 2017, **14**, 10.

[85] D. Sacks and S. Kamhawi, *Annual Review of Microbiology*, 2001, **55**, 453–483.

[86] P. N. Monk and L. J. Partridge, *Infectious Disorders - Drug Targets*, 2012, **12**, 4–17.

[87] J. K. Ventress, L. J. Partridge, R. C. Read, D. Cozens, S. MacNeil and P. N. Monk, *PLOS ONE*, 2016, **11**, e0160387.

[88] I. Herbots, B. Kottwitz, P. J. Reilly, R. L. Antrim, H. Burrows, H. B. M. Lenting, L. Viikari, A. Suurnäkki, M.-L. Niku-Paavola, J. Pere and J. Buchert, in *Ullmann's Encyclopedia of Industrial Chemistry*, American Cancer Society, 2008.

[89] W. B. Shelley, H. J. Hurley and A. C. Nichols, *AMA Archives of Dermatology and Syphilology*, 1953, **68**, 430–446.

[90] P. M. J. Terpstra, *International Biodeterioration & Biodegradation*, 1998, **41**, 169–175.

[91] N. L. Belkin, *American Journal of Infection Control*, 1998, **26**, 149–151.

[92] S. Munk, C. Johansen, L. H. Stahnke and J. Adler-Nissen, *Journal of Surfactants and Detergents*, 2001, **4**, 385–394.

[93] C. Callewaert, S. Van Nevel, F.-M. Kerckhof, M. S. Granitsiotis, N. Boon, S. V. Nevel, F.-m. Kerckhof, S. Michael, N. Boon, M. Technology and H. Zentrum, *Frontiers in Microbiology*, 2015, **6**, 1381.

[94] S. Fijan, S. Koren, A. Cencič and S. Šostar-Turk, *Diagnostic Microbiology and Infectious Disease*, 2007, **57**, 251–257.

[95] M. J. Blaser, P. F. Smith, H. J. Cody, W.-L. Wang and F. M. LaForce, *The Journal of Infectious Diseases*, 1984, **149**, 48–57.

[96] Y. K. Demirel, M. Khorasanchi, O. Turan and A. Incecik, Low Carbon Shipping Conference, London, 2013, p. 13.

[97] B. Craigen, A. Dashiff and D. E. Kadouri, *The Open Microbiology Journal*, 2011, **5**, 21–31.

[98] Y. Lequette, G. Boels, M. Clarisse and C. Faille, *Biofouling*, 2010, **26**, 421–431.

[99] N. Oulahal-Lagsir, A. Martial-Gros, M. Bonneau and L. J. Blum, *Biofouling*, 2003, **19**, 159–168.

[100] I. Aldridge, B. Chmurny Alan, R. Durham Donald, L. Roberts Rowena and G. Fan Lai-Duien, 1993.

[101] V. Prabhawathi, T. Boobalan, P. M. Sivakumar and M. Doble, *PLOS ONE*, 2014, **9**, e96152.

[102] M. Loiselle and K. W. Anderson, *Biofouling*, 2003, **19**, 77–85.

[103] D. Fleming, L. Chahin and K. Rumbaugh, *Antimicrobial Agents and Chemotherapy*, 2016, **61**, e01998–16.

[104] J. M. Dow, L. Crossman, K. Findlay, Y. Q. He, J. X. Feng and J. L. Tang, *Proc Natl Acad Sci USA*, 2003, **100**, 10995–11000.

[105] C. B. Whitchurch, T. Tolker-Nielsen, P. C. Ragas and J. S. Mattick, *Science*, 2002, **295**, 1487.

[106] J. Song, J. Liang, X. Liu, W. E. Krause, J. P. Hinestroza and O. J. Rojas, *Thin Solid Films*, 2009, **517**, 4348–4354.

[107] J. Amim, P. M. Kosaka and D. F. S. Petri, *Cellulose*, 2008, **15**, 527–535.

[108] D. B. Hall, P. Underhill and J. M. Torkelson, *Polymer Engineering & Science*, 1998, **38**, 2039–2045.

[109] C. B. Walsh and E. I. Franses, *Thin Solid Films*, 2003, **429**, 71–76.

[110] M. Ibaragi, *Ph.D. thesis*, University of Sheffield, 2015.

[111] S. Gunnars, L. Wågberg and M. Cohen Stuart, *Cellulose*, 2002, **9**, 239–249.

[112] S. Fält, L. Wågberg, E. L. Vesterlind and P. T. Larsson, *Cellulose*, 2004, **11**, 151–162.

[113] F. A. Jenkins and H. E. White, *Fundametals of Optics*, McGraw-Hill Book Company, New York, USA, 3rd edn., 1976.

[114] P. C. Jukes, A. Das, M. Durell, D. Trolley, A. M. Higgins, M. Geoghegan, J. E. Macdonald, R. a. L. Jones, S. Brown and P. Thompson, *Macromolecules*, 2005, **38**, 2315–2320.

[115] M. Geoghegan, J. S. Andrews, C. A. Biggs, K. E. Eboigbodin, D. R. Elliott, S. Rolfe, J. Scholes, R. G. J. Edyvean, L. Swanson, R. Rutkaite, R. Fernando, Y. Pen and S. A. Banwart, *Faraday Discuss.*, 2008, **139**, 85–103.

[116] A. L. Morales-García, *Ph.D. thesis*, 2014.

[117] W. Zheng, H. Fan, L. Wang and Z. Jin, *Langmuir*, 2015, **31**, 11671–11677.

[118] A. Beaussart, A. E. Baker, S. L. Kuchma, S. El-Kirat-Chatel, G. A. O'Toole and Y. F. Dufrêne, *ACS Nano*, 2014, **8**, 10723–10733.

[119] L. Vidakovic, P. K. Singh, R. Hartmann, C. D. Nadell and K. Drescher, *Nature Microbiology*, 2017, **3**, 26–31.

[120] P. C. Y. Lau, J. R. Dutcher, T. J. Beveridge and J. S. Lam, *Biophysical Journal*, 2009, **96**, 2935–2948.

[121] R. Morgan, S. Kohn, S. H. Hwang, D. J. Hassett and K. Sauer, *Journal of Bacteriology*, 2006, **188**, 7335–7343.

[122] A. Heydorn, A. T. Nielsen, M. Hentzer, C. Sternberg, M. Givskov, B. K. Ersbøll and S. Molin, *Microbiology*, 2000, **146**, 2395–2407.

[123] J. B. Kaplan, *Journal of Dental Research*, 2010, **89**, 205–218.

[124] M. Okshevsky, V. R. Regina and R. L. Meyer, *Current Opinion in Biotechnology*, 2015, **33**, 73–80.

[125] S. D. Goodman, K. P. Obergfell, J. A. Jurcisek, L. A. Novotny, J. S. Downey, E. A. Ayala, N. Tjokro, B. Li, S. S. Justice and L. O. Bakaletz, *Mucosal Immunology*, 2011, **4**, 625–637.

[126] M. J. Huseby, A. C. Kruse, J. Digre, P. L. Kohler, J. A. Vocke, E. E. Mann, K. W. Bayles, G. A. Bohach, P. M. Schlievert, D. H. Ohlendorf and C. A. Earhart, *Proceedings of the National Academy of Sciences*, 2010, **107**, 14407–14412.

[127] J. N. C. Fong and F. H. Yildiz, *Microbiology Spectrum*, 2015, **3**, 4–2014.

[128] L. S. Pakkiri, B. A. Wolucka, E. J. Lubert and C. J. Waechter, *Glycobiology*, 2004, **14**, 73–81.

[129] M. Banar, M. Emaneini, M. Satarzadeh, N. Abdellahi, R. Beigverdi, W. B. Leeuwen and F. Jabalameli, *PLOS ONE*, 2016, **11**, e0164622.

[130] K. Gori, L. E. T. Baltsen and M. Allesen-Holm, 2013.

[131] W.-s. Chen, W.-H. Chen, Z. Chen, A. A. Gooding, K.-J. Lin and C.-H. Kiang, *Physical Review Letters*, 2010, **105**, 218104.

[132] M. K. Jain and O. G. Berg, *Biochimica et Biophysica Acta (BBA) - Lipids and Lipid Metabolism*, 1989, **1002**, 127–156.

[133] W. Aehle and S. Amin Neelam, 2008.

[134] K. Holmberg, *Colloids and Surfaces B: Biointerfaces*, 2018, **168**, 169–177.

[135] J. Zhang, Y. Zhang, W. Li, X. Li and X. Lian, *Journal of Surfactants and Detergents*, 2014, **17**, 1059–1067.

[136] A. Bouchet-Spinelli, L. Coche-Guérente, S. Armand, F. Lenouvel, P. Labbé and S. Fort, *Sensors and Actuators B: Chemical*, 2013, **176**, 1038–1043.

[137] X. Turon, O. J. Rojas and R. S. Deinhammer, *Langmuir*, 2008, **24**, 3880–3887.

[138] M. Stoytcheva, R. Zlatev, Z. Velkova and G. Montero, *Analytical Methods*, 2013, **5**, 3811–3815.

[139] E. Engvall and P. Perlmann, *The Journal of Immunology*, 1972, **109**, 129–135.

[140] D. N. Rubingh, *Current Opinion in Colloid & Interface Science*, 1996, **1**, 598–603.

[141] Y. Sangtian, L. An, Z. Hao, L. Mingfang and X. Xinhui, *Chin. J. Chem. Eng.*, 2009, **17**, 829–834.

[142] G. H. Peters, *Colloids and Surfaces B: Biointerfaces*, 2002, **26**, 84–101.

[143] J. F. Ang, *Journal of Food Science*, 1991, **56**, 1682–1684.

[144] I. Panaiotov, M. Ivanova and R. Verger, *Current Opinion in Colloid & Interface Science*, 1997, **2**, 517–525.

[145] V. Tangcharoensathien, W. Sattayawutthipong, S. Kanjanapimai, W. Kanpravidth, R. Brown and A. Sommanustweechai, *Bulletin of the World Health Organization*, 2017, **95**, 599–603.

[146] A. S. Nagle, S. Khare, A. B. Kumar, F. Supek, A. Buchynskyy, C. J. N. Mathison, N. K. Chennamaneni, N. Pendem, F. S. Buckner, M. H. Gelb and V. Molteni, *Chemical Reviews*, 2014, **114**, 11305–11347.

[147] P. A. Bates, *International Journal for Parasitology*, 2007, **37**, 1097–1106.

[148] J. Alvar, I. D. Vélez, C. Bern, M. Herrero, P. Desjeux, J. Cano, J. Jannin, M. den Boer and t. W. L. C. Team, *PLOS ONE*, 2012, **7**, e35671.

[149] S. L. Croft and P. Olliaro, *Clinical Microbiology and Infection: The Official Publication of the European Society of Clinical Microbiology and Infectious Diseases*, 2011, **17**, 1478–1483.

[150] C.-L. Forestier, Q. Gao and G.-J. Boons, *Frontiers in Cellular and Infection Microbiology*, 2015, **4**, 193.

[151] S. Kamhawi, M. Ramalho-Ortigao, V. M. Pham, S. Kumar, P. G. Lawyer, S. J. Turco, C. Barillas-Mury, D. L. Sacks and J. G. Valenzuela, *Cell*, 2004, **119**, 329–341.

[152] P. Chapman, R. E. Ducker, C. R. Hurley, J. K. Hobbs and G. J. Leggett, *Langmuir*, 2015, **31**, 5935–5944.

[153] A. Y. Chernyak, G. V. M. Sharma, L. O. Kononov, P. R. Krishna, A. B. Levinsky, N. K. Kochetkov and A. V. Rama Rao, *Carbohydrate Research*, 1992, **223**, 303–309.

[154] N. A. Hassuna, P. N. Monk, F. Ali, R. C. Read and L. J. Partridge, *Journal of Infection*, 2017, **75**, 115–124.

[155] M. Yáñez-Mó, O. Barreiro, M. Gordon-Alonso, M. Sala-Valdés and F. Sánchez-Madrid, *Trends in Cell Biology*, 2009, **19**, 434–446.

[156] G. E. Thwaites, J. D. Edgeworth, E. Gkrania-Klotsas, A. Kirby, R. Tilley, M. E. Török, S. Walker, H. F. Wertheim, P. Wilson and M. J. Llewelyn, *The Lancet Infectious Diseases*, 2011, **11**, 208–222.